

Electron probing of oxygen-evolving oxide catalysts

Présentée le 13 avril 2022

Faculté des sciences et techniques de l'ingénieur
Laboratoire pour la caractérisation in situ des nanomatériaux par des électrons
Programme doctoral en science et génie des matériaux

pour l'obtention du grade de Docteur ès Sciences

par

Tzu-Hsien SHEN

Acceptée sur proposition du jury

Prof. P. Bowen, président du jury
Prof. V. Tileli, directrice de thèse
Prof. F. Ross, rapporteuse
Prof. J. Suntivich, rapporteur
Prof. J. Luterbacher, rapporteur

Acknowledgements

PhD is a journey I would never forget. I am grateful for people who have helped make my PhD possible.

First of the all, I would like to express my deepest gratitude to my advisor, Prof. Vaso Tileli for everything she has helped me in my PhD. I feel so lucky and thankful to have her as my PhD advisor. I have learnt a lot from her during these years such as experiments, scientific viewpoint, attitude, critical thinking, and many other aspects. For me, she is an advisor that you can seek for the help. When I felt depressed, she was always there to cheer me up. When I lost my direction or motivation, she was there to guide me and push me to be better. When I struggled on my work, I could simply go to her office and discussed with her. I really appreciate that she always makes time for helping me so much in these years despite her busy agenda. Without her, I could say I could barely finish my PhD.

I would like to thank Prof. Jeremy Luterbacher, Prof. Frances Ross, Prof. Jin Suntivich, and Prof. Paul Bowen for agreeing to be on my PhD defense committee.

I would like to thank my collaborators for experimental helps and feedback of manuscripts. I am very grateful to collaborate with Prof. Yang Shao-Horn from MIT and her student Jiayu Peng. I really appreciate for providing the materials for my thesis work and commenting on our manuscripts. I would also like to thank Dr. Liam Spillane from Gatan for all the help on EELS.

A big part of my PhD life involves my dearest labmates at INE: Jing, Reinis, Jan, Robin, Michele, My, Morgan, Martina, Salta, and Pierpaolo. They have always been around and made my PhD life so enjoyable. I am glad I can have such nice, smart, and supportive labmates to work with during my PhD. Working together with them make me feel I am not alone. I really appreciate their help and have learnt a lot from them.

I would like to say thank you to all my friends outside the lab. I really enjoy hanging out with them like going out for meals, skiing, climbing, bbq, and many other activities.

I would like to take chance to thank CMi and CIME for providing the instruments I need for my thesis. I have learnt a lot from the staffs during the training and they have been always

helpful when I encountered problems during the experiments. Without their supports, many experiments and fabrications could not be successfully performed.

Last, a big thanks to my mom, dad, and my young brother. Thank you for always being there for me and supporting all the decision I have made.

Lausanne, 2021

Tzu-Hsien Shen

Résumé

Le craquage de l'eau est l'une des manières les plus propres pour stocker de l'énergie. La production d'hydrogène et d'oxygène sous forme gazeuse peut être utilisée dans les piles à combustible pour générer de l'électricité, de la puissance et de la chaleur. Dans le cas du processus de craquage de l'eau, la réaction d'évolution de l'oxygène (REO) se produisant à l'anode est la plus lente, limitant son efficacité. Des électrocatalyseurs sont utilisés pour réduire la barrière cinétique de la REO. Le développement de catalyseurs qui soient stables et avec des hautes performances, dédiés à la REO, requière une compréhension fondamentale de leurs propriétés électrocatalytiques, d'où le fait que leur caractérisation holistique soit indispensable.

L'objectif de cette thèse est d'examiner des catalyseurs à base de Co pour la REO dans un milieu alcalin en utilisant des techniques avancées de microscopie électronique en transmission (à balayage) (MET(B)). En débutant par la caractérisation de la surface d'un catalyseur oxyde hautement actif pour la REO, le $\text{Ba}_{0.5}\text{Sr}_{0.5}\text{Co}_{0.8}\text{Fe}_{0.2}\text{O}_{3-\delta}$ (BSCF), il est montré que les surfaces de particules de BSCF, telles que synthétisées, sont riches en Co/Fe et adoptent une structure en spinelle avec une valence réduite des ions de Co. La structure Co/Fe en spinelle est, de plus, liée à la formation de Co(Fe)OOH hautement actif à la surface du BSCF. Un examen approfondi et en temps réel des catalyseurs oxydes BSCF en utilisant la MET électrochimique en phase liquide montre un comportement de mouillage changeant des catalyseurs oxydes à base de Co par l'analyse de mouvements du liquide autour des particules d'oxydes. Les interactions interfaciales à la surface de l'électrolyte sous voltamétrie cyclique sont corrélées à l'électromouillage et aux transformations hydrophiles de surface. L'évolution de l'oxygène moléculaire est détectée qualitativement sous des conditions de REO en identifiant des pics d' O_2 dans des spectres de perte d'énergie des électrons. La quantification de l' O_2 en utilisant la spectroscopie de perte d'énergie des électrons est également démontrée, en attendant des améliorations futures.

Le travail ci-inclus offre de nouvelles perspectives au cadre de caractérisation des catalyseurs oxydes pour la REO en utilisant la MET(B). Les structures volumiques à surfaciques des catalyseurs peuvent être analysées et les interactions interfaciales des catalyseurs en particule simple peuvent être examinées en temps réel. Les conclusions aident dans la compréhension des performances et de la stabilité des catalyseurs oxydes évoluant l'oxygène, avec de futures

perspectives envisageant un examen quantitatif complet et en temps réel des réactions électrocatalytiques. A terme, une caractérisation quantitative par la MET(B) électrochimique en phase liquide pourrait fournir une compréhension des sites de surface actifs et des cinétiques de réaction des catalyseurs d'évolution d'oxygène.

Mots-clés : réaction d'évolution de l'oxygène, électrocatalyseurs, oxydes à base de Co, microscopie électronique en transmission (à balayage), spectroscopie de perte d'énergie des électrons, microscopie électronique en transmission électrochimique en phase liquide.

Abstract

Water splitting is one of the cleanest ways to store energy. The production of hydrogen and oxygen gases can be utilized in fuel cells to generate electricity, power, and heat. In the water splitting process, the oxygen evolution reaction (OER), taking place at the anode, is the sluggish reaction limiting the efficiency. Electrocatalysts are used to reduce the kinetic barrier of OER. Development of high-performance and stable OER catalysts requires fundamental understanding of their electrocatalytic properties and, hence, their holistic characterization is indispensable.

The objective of this thesis is to probe Co-based oxide catalysts for OER in an alkaline medium using advanced (scanning) transmission electron microscopy ((S)TEM) techniques. Starting with the surface characterization of a highly active OER oxide catalyst, $\text{Ba}_{0.5}\text{Sr}_{0.5}\text{Co}_{0.8}\text{Fe}_{0.2}\text{O}_{3-\delta}$ (BSCF), it is shown that the surfaces of the as-synthesized BSCF particles are Co/Fe rich and adopt a spinel-like structure with a reduced valence of Co ions. The Co/Fe spinel structure is further linked to the formation of the highly active Co(Fe)OOH at the BSCF surface. Further real-time probing of BSCF oxide catalysts using electrochemical liquid-cell TEM shows a switchable wetting behavior of Co-based oxide catalysts by analyzing the liquid movement around oxide particles. The interfacial interactions at the surface-electrolyte under potential cycling are correlated to electrowetting and hydrophilic surface transformation. Molecular oxygen evolution is detected qualitatively under OER conditions by identifying the O_2 feature in electron energy-loss spectra. Quantification of the O_2 using electron energy-loss spectroscopy is also demonstrated, pending further improvements.

The work herein offers new insights into the characterization framework of oxide catalysts for OER using (S)TEM. The bulk to surface structure of the catalysts can be analyzed, and the interfacial interactions of single-particle catalysts can be probed in real-time. The findings aid in understanding the performance and stability of oxygen-evolving oxide catalysts with further prospects envisioned towards a complete quantitative probing of electrocatalytic reactions in real-time. Ultimately, quantitative characterization in electrochemical liquid-phase (S)TEM can provide understanding of surface-active sites and reaction kinetics of oxygen evolution catalysts.

Keywords: oxygen evolution reaction, electrocatalysts, Co-based oxides, (scanning) transmission electron microscopy, electron energy-loss spectroscopy, electrochemical liquid-phase transmission electron microscopy.

Table of contents

Acknowledgements	i
Résumé	iii
Abstract	v
Table of contents.....	vii
Chapter 1 Introduction	11
Chapter 2 Literature review.....	15
2.1 Mechanism of oxygen evolution reaction (OER)	15
2.2 Perovskite OER catalysts and $\text{Ba}_{0.5}\text{Sr}_{0.5}\text{Co}_{0.8}\text{Fe}_{0.2}\text{O}_{3-\delta}$	17
2.2.1 e_g occupancy as a descriptor	17
2.2.2 Bulk O 2p band center and metal-oxygen covalency	18
2.2.3 Surface stability of BSCF	20
2.3 Solid-liquid interfacial interactions	23
2.3.1 Charge transfer and surface restructuring.....	23
2.3.2 Surface wettability	24
2.4 Operando/ <i>in situ</i> techniques for oxygen electrocatalysis.....	27
2.4.1 X-ray based techniques.....	28
2.4.2 <i>In situ</i> (scanning) transmission electron microscopy	32
Chapter 3 Methodology and Instrumentation.....	35
3.1 Principles of (S)TEM.....	35
3.1.1 Overview of (S)TEM.....	35
3.1.2 Principles of TEM operation in transmission mode	37
3.1.3 Electron diffraction in TEM	40
3.1.4 Principles of TEM operation in scanning transmission mode	41

3.1.5	EDS.....	44
3.2	Electron energy-loss spectroscopy (EELS).....	45
3.2.1	Physics of EELS	45
3.2.2	EELS acquisition	49
3.3	Electrochemical liquid-phase (S)TEM.....	51
3.3.1	Background and principles of electrochemical liquid-phase (S)TEM.....	51
3.3.2	Spatial resolution in LP-(S)TEM.....	52
3.3.3	Energy-filtered TEM for LP-TEM	54
3.3.4	Electron-beam induced effects in LP-(S)TEM	55
3.3.5	Microfabrication and configuration of electrochemical chips for LP-TEM.....	56
3.3.6	Electrochemical measurements	58
3.3.7	Potential calibration of Pt quasi-reference electrode for electrochemical LP-TEM.....	60
Chapter 4	Oxygen Evolution Reaction in $\text{Ba}_{0.5}\text{Sr}_{0.5}\text{Co}_{0.8}\text{Fe}_{0.2}\text{O}_{3-\delta}$ Aided by Intrinsic Co/Fe Spinel-Like Surface	63
4.1	Introduction.....	64
4.2	Experimental Section.....	65
4.2.1	Materials	65
4.2.2	Lab-on-chip setup	66
4.2.3	(S)TEM, EDS, and EELS characterizations	67
4.2.4	<i>In situ</i> electrochemical cell	68
4.2.5	Electrochemical measurements in conventional bulk cell	68
4.3	Results and Discussion	69
4.3.1	Structural and chemical analysis of BSCF surfaces	69
4.3.2	Electrochemical evaluation of Co/Fe spinel surface.....	73

4.3.3	<i>In situ</i> electrochemical behavior of BSCF	76
4.4	Mechanism	77
4.5	Conclusions	78
Chapter 5	Switchable Wetting of Oxygen-Evolving Oxide Catalysts	81
5.1	Introduction	82
5.2	Experimental section	83
5.2.1	Materials	83
5.2.2	Working electrode preparation	84
5.2.3	Electrochemical measurements	84
5.2.4	Liquid-phase TEM setup	84
5.2.5	Operando TEM and selected-area electron diffraction analyses	85
5.2.6	Image segmentation	85
5.2.7	EELS characterization	86
5.2.8	EELS quantification	86
5.3	Results and discussion	87
5.3.1	Operando TEM observation of BSCF under potential cycling	87
5.3.2	Operando EELS analysis of molecular oxygen evolution	89
5.3.3	Switchable wetting behavior of cobalt-based oxides	91
5.3.4	Proposed mechanism of wetting behavior	93
5.4	Conclusions	96
Chapter 6	Towards EELS Quantification of O₂ in LP-TEM	99
6.1	Oxygen evolution of an IrO ₂ particle	99
6.2	EELS quantification process for the molecular oxygen	101
6.2.1	Fundamentals of EELS quantification	102
6.2.2	Quantification of gas composition by EELS in environmental TEM....	104

6.2.3	Standard-based EELS quantification.....	105
6.3	EELS quantification in cell enclosure.....	105
6.3.1	Air-cell enclosure	106
6.3.2	Liquid-cell enclosure with O ₂ gas.....	109
6.3.3	Discussion on areal density of O ₂	111
6.4	Conclusions.....	111
Chapter 7	Conclusions and Perspectives	113
Appendix A	117
	Runcard of the fabrication of the electrochemical chips.....	118
Appendix B	119
	Synchronization of TEM image sequence and CV curves.....	120
Appendix C	127
	Supporting Information of Chapter 4.....	128
Appendix D	137
	Supporting Information of Chapter 5.....	138
Bibliography	147
CURRICULUM VITAE	170

Chapter 1 Introduction

Compared to traditional fossil fuel technologies, water splitting, production of hydrogen and oxygen gases [1], is a cleaner way to store energy. The operation of low temperature water electrolysis is classified into alkaline [2] and polymer–electrolyte membrane (PEM) electrolyzers [3], depending on the kind of electrolyte and the type of ions (OH^- and H^+). Conventional alkaline electrolysis is performed in the alkaline liquid electrolyte using a diaphragm to separate gases while PEM provides a solid electrolyte medium with high proton conductivity. Alkaline electrolysis is well established and it is the most applied commercial technology. Its main advantages are the long-term stability and relatively low cost. Considering electrolyzing water with alkaline electrolytes, the cathode involves the hydrogen evolution reaction (HER, $\text{H}_2\text{O} + 4\text{e}^- \rightarrow 2\text{H}_2 + 4\text{OH}^-$) while the anode proceeds with oxygen evolution reaction (OER, $4\text{OH}^- \rightarrow \text{O}_2 + 2\text{H}_2\text{O} + 4\text{e}^-$). A schematic illustration of an electrolyzer, alkaline cell is shown in Figure 1.1.

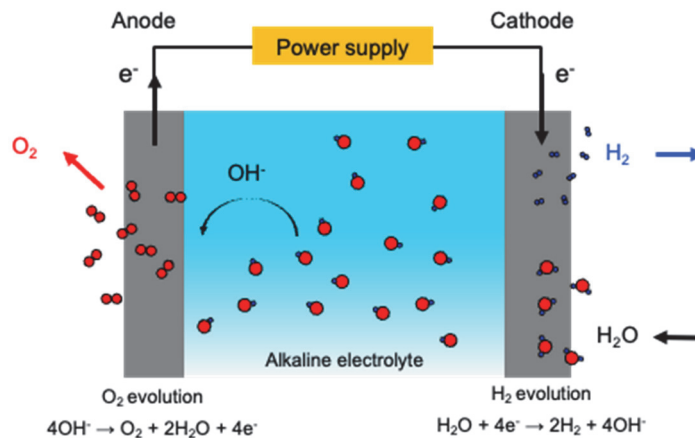


Figure 1.1. Schematic illustration of alkaline electrolysis. OER occurs at anode while HER happens at cathode.

Compared to HER, OER is more sluggish due to its four-electron transfer reaction. According to thermodynamics, the minimum potential between two electrodes to trigger water splitting ($\text{H}_2\text{O} \rightarrow 2\text{H}_2 + \text{O}_2$) is $E_{\text{eq}}=1.23 \text{ V}$ [4]. However, in the real case, the potential to have water splitting is higher. The additional applied potential is called overpotential (η) and it represents the potential difference between the applied and equilibrium potentials of the reaction ($E-E_{\text{eq}}$). The slow kinetic nature of OER due to its four electron-transfer nature requires much higher overpotential than HER ($\eta_{\text{OER}} > \eta_{\text{HER}}$), meaning that OER leads to high energy losses during water splitting. Thus, it is widely accepted that OER is the kinetical bottleneck limiting the efficiency of water electrolysis. To lower this kinetic barrier in OER, catalysts to reduce the overpotential are used. In practice, the overpotential for OER is commonly referred to a value that has to be applied to achieve a specified current density, for example, 10 mA/cm^2 [5]. When compared to the value of the overpotential, the performance OER electrocatalysts can be evaluated. Thus, low overpotential values of electrocatalysts indicate better electrocatalytic ability.

To lower the OER overpotential, highly active electrocatalysts with long-term stability have been developed. In the past decades, precious metal oxides such as RuO_2 and IrO_2 had been the benchmarks of OER catalysts due to their high activity at a wide range of pH values [6–8]. However, the scarcity of iridium and ruthenium leads to their high cost, which limits their large-scale industrial utilization. Therefore, design and synthesis of low-cost and highly active catalysts for OER is central to boosting the efficiency of water electrolysis. Transition metal oxides have been considered as a strong candidate to replace precious oxide catalysts for OER owing to their low-cost and stability in alkaline medium [9]. Researchers have explored transition metal oxides with different structures such as perovskite, spinel, and layered double hydroxides showing outstanding OER activity and stability [4,9–11]. One of them, the highly active Co-based perovskite oxide OER catalyst $\text{Ba}_{0.5}\text{Sr}_{0.5}\text{Co}_{0.8}\text{Fe}_{0.2}\text{O}_{3-\delta}$ (BSCF) [12] is the main focus of my thesis.

Designing catalysts with better performance and stability requires a fundamental understanding of how the electrocatalysts work during the reaction. A critical aspect towards this understanding is to obtain detailed information of the surfaces that are responsible for the reactions. Scanning transmission electron microscopy ((S)TEM) based techniques are

particularly useful to diagnose the catalytic functionalities due to their high spatial resolution down to the nanometer scale and, more importantly, due to their combination of a great variety of analytical methods to inspect the crystal structure, elemental composition, and/or valence site-specifically. A step forward includes performing (S)TEM in real-time during operation which can further provide valuable information of the evolution of the catalysts, solid-liquid interactions, and detection of the catalytic products during relevant conditions. The objective of this thesis is to probe the OER oxide catalysts using (S)TEM techniques and ultimately provide insights of the dynamic behavior during OER catalytic processes.

An overview of the fundamentals of OER such as mechanisms and descriptors for oxide catalysts is given in Chapter 2. It also discusses solid-liquid interfacial interactions that are related to OER. In situ/operando characterizations of electrocatalysts during operation conditions are also reviewed.

Chapter 3 includes an overview of the methodology and instrumentation. The first part includes the operating principles of (S)TEM techniques. The second part covers electron energy-loss spectroscopy (EELS) which is used to probe the surface of BSCF and the catalytic products during the reaction. The third part reviews electrochemical liquid-phase (S)TEM that is implemented to perform operando characterizations.

In Chapter 4, the detailed investigation of electron probing of the surface structure of BSCF is given. Postmortem and identical location (S)TEM analyses reveal that the Co/Fe spinel-like surface retains a stable chemical environment of the Co/Fe ions. The spinel surface is found to be related to the surface transformation of BSCF's surface to the oxyhydroxide active OER phase.

Chapter 5 details the operando TEM and EELS studies of Co-based OER catalysts. Switchable wetting of the Co-based oxide catalysts is probed using electrochemical liquid-phase TEM by analyzing the liquid movement surrounding the single oxide particles. Further, the molecular oxygen is detected using EELS under operation conditions. The mechanism of switchable wetting is proposed to be related to electrowetting, surface reconstruction of hydrophilic oxyhydroxide phase, and evolution of molecular oxygen.

Chapter 6 presents the quantification of molecular oxygen using EELS. The evolution of the fingerprint of molecular oxygen in O K EEL spectra is shown to correspond to OER potentials during cycling. Mapping of O₂ in the vicinity of an IrO₂ particle under chronoamperometry is demonstrated. Standard-based quantification workflow is presented to quantify the molecular oxygen fine structure. To validate the quantification, air cell conditions, in which the N₂/O₂ ratio is known, are used. The quantification process is further applied to liquid-cell enclosure with O₂ gas. The discrepancies between the quantification results and nominal values are discussed.

Chapter 7 summarizes the electron probing of oxygen-evolving Co-based oxide catalysts and provides future directions of the work.

Chapter 2 Literature review

This chapter covers the background and literature review. I start by introducing the mechanisms that are used to describe electrocatalytic oxygen evolution reaction (OER) (2.1). Then the focus is placed on $\text{Ba}_{0.5}\text{Sr}_{0.5}\text{Co}_{0.8}\text{Fe}_{0.2}\text{O}_{3-\delta}$ (BSCF), a highly active perovskite OER catalyst (2.2). Descriptors and surface stability aspects are also discussed. The next section (2.3) generalizes solid-liquid interfacial interactions, which are prominent during the heterogenous OER electrocatalysis. Charge-transfer processes, surface restructuring, and surface wetting are also discussed. As a mean to experimentally verify what contributes to the OER catalysts performance and stability, the final section presents the work that has been reported using operando and *in situ* methodologies (2.4).

2.1 Mechanism of oxygen evolution reaction (OER)

The performance of OER catalysts can be improved by tuning the intrinsic activity of the structure or/and by increasing the number of the active sites at the catalytic surfaces. To get insights into intrinsic activity of the active sites and reaction mechanisms, researchers have utilized and developed computational tools based on density functional theory or molecular dynamic simulations where different OER reaction mechanisms have been proposed [13]. Schematic illustrations of the conventional adsorbate evolution mechanism (AEM) and lattice-oxygen-mediated mechanism (LOM) are shown in Figure 2.1a,b. AEM is assumed to involve four concerted proton–electron transfer (CPET) reactions centered on the metal ion. That is, at each step, a proton is injected into the electrolyte and is coupled with a transferred electron [14]. First, hydroxyl ions (OH^-) adsorb on the surface metallic site (M). The M-OH then deprotonate to form metal-oxygen bonds (M-O). Then, M-O reacts with another OH^- to form the MOOH intermediate. In the final step, O_2 is evolved through the deprotonation of HOO

with the regeneration of the active site. LOM, on the contrary, describes nonconcerted proton-electron transfer reactions. LOM also involves oxidation of lattice oxygen at the surface of the electrocatalysts [15]. Compared to conventional AEM, LOM proceeds on two neighboring metal sites rather than a single metal site. First, two OH^- on the dual metal sites deprotonate at the same step, resulting in oxidation of lattice oxygen and formation of two metal–oxo species. Then, instead of forming the OOH intermediate state, these two neighboring oxo species directly couple to form O_2^{2-} .

Another way to understand OER electrocatalysis is via trends that describe the activity among different catalysts. Early works from Rossmeisl *et al.* proposed the standard Gibbs free energy difference of two intermediate states ($\Delta G_{\text{O}^*}^0 - \Delta G_{\text{HO}^*}^0$) as a universal descriptor to predict the OER activity of electrocatalysts [14]. The descriptor ($\Delta G_{\text{O}^*}^0 - \Delta G_{\text{HO}^*}^0$) indicates that the optimized adsorption strength of the intermediates should be neither too weak nor too strong, resulting in a volcano plot of OER overpotential as a function of ($\Delta G_{\text{O}^*}^0 - \Delta G_{\text{HO}^*}^0$), Figure 2.1c. Many descriptors on the basis of oxygen binding energy have been proposed to describe the relationship between electronic structure and activity. The descriptors, specifically for oxide OER electrocatalysts, can be separated into two main categories: molecular orbital (MO) and bulk band theory. For example, e_g filling [12,16,17] relies on the basis of MO principles while metal-oxygen covalency [18,19], O 2p band center [20], and charge transfer energy [21] are related with the bulk band theory. The following section covers several popular descriptors that describe perovskite oxides as OER catalysts.

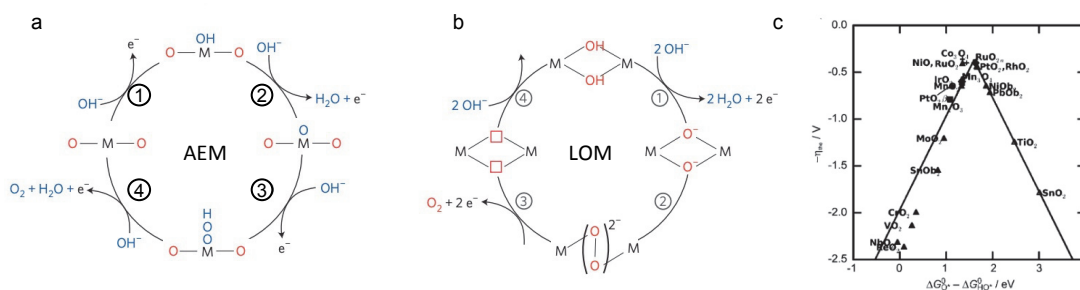


Figure 2.1. Schematic illustration of the OER mechanisms.. (a) Conventional adsorbate evolution mechanism (AEM). (b) More recent lattice oxygen mediated mechanism (LOM). a and b reproduced from ref. [22] with permission. © 2016 Springer Nature. (c) OER overpotential values of metal oxide catalysts with different structures as a function of ($\Delta G_{\text{O}^*}^0 - \Delta G_{\text{HO}^*}^0$). Reproduced from ref. [14] with permission. © 2011 Wiley-VCH.

2.2 Perovskite OER catalysts and $\text{Ba}_{0.5}\text{Sr}_{0.5}\text{Co}_{0.8}\text{Fe}_{0.2}\text{O}_{3-\delta}$

Perovskites of the general formula ABO_3 have transition metals that occupy B-sites with corner-sharing octahedra of oxygen, while alkaline and/or rare-earth ions are located on the A-sites with 12-fold coordination with oxygen [23]. A schematic illustration of the perovskite structure is shown in Figure 2.2a. Owing to their tunable electronic structure via substitution of a variety of elements in the structure, they have been shown to exhibit diverse physical and chemical properties such as ferroelectricity [24], piezoelectricity [25], pseudocapacitance [26], etc. The behavior of electrocatalytic oxygen evolution on perovskite oxides was first reported in 1980s [27–29], when Bockris *et al.* systematically studied OER electrocatalytic properties of lanthanum-based perovskites with different B-site first-row transition metals [27]. The authors proposed that, on the basis of MO, the electrocatalytic activity of lanthanum-based perovskites increased with increasing occupancy of antibonding orbitals of the intermediate state B-OH.

2.2.1 e_g occupancy as a descriptor

In 2011, Suntivich *et al.* presented a complete study with several perovskites were evaluated for the oxygen evolution reaction. Within this study, an exceptional OER electrocatalyst, the complex perovskite $\text{Ba}_{0.5}\text{Sr}_{0.5}\text{Co}_{0.8}\text{Fe}_{0.2}\text{O}_{3-\delta}$ (BSCF), in alkaline solution [12] was presented revealing that the intrinsic OER activity of BSCF is even better than the benchmarked IrO_2 nanoparticles [12]. Typically, BSCF has been shown to exhibit exceptional oxygen ion conductivity [30] for applications such as gas sensors, oxygen transport membranes, and solid oxide fuel cell (SOFC) electrodes [31–33]. The breakthrough from Suntivich *et al.* opened a new application regime for BSCF, specifically for OER electrocatalysis. After Suntivich and co-workers reported the outstanding OER performance of BSCF, many studies on BSCF as OER catalysts followed [12,34–39]. Conventional MO principles were proposed in Suntivich's article to explain the activity of perovskite oxides as OER catalysts. A step forward from the occupancy of antibonding orbitals proposed by Bockris *et al.* back in 1980s, Suntivich and co-workers included covalent mixing and crystal field of metal d and O 2p orbitals. The B-site transition metal site is normally considered as active during electrocatalysis. Their anti-

bonding states split into e_g and t_{2g} as shown in Figure 2.2b. The e_g orbitals on the surface of the transition metal ions participate in the bonding of surface adsorbates. The binding of oxygen is stronger when the e_g filling is lower, and *vice versa*. Thus, in principle, neither too high nor too low occupancy can lead to optimized binding strength of intermediate adsorbates. In this way, the electron filling in e_g orbitals of transition metals acts as a descriptor for elucidating the OER catalytic activity of perovskite oxides. It was proposed that the optimized e_g occupancy is close to 1.2 for OER electrocatalysts by reporting a volcano plot of e_g electron versus OER applied potential at $i = 50 \mu\text{A}/\text{cm}_{\text{ox}}^2$ (Figure 2.2c). As shown on the plot, with the filling close to 1.2, BSCF exhibits the best OER activity among the perovskites compared. After successfully explaining the trend of OER activity among perovskite oxides, the e_g filling, which is regulated via oxidation [17] and spin states [40,41], has been widely used to elucidate the performance of OER oxide electrocatalysts [16,17,42].

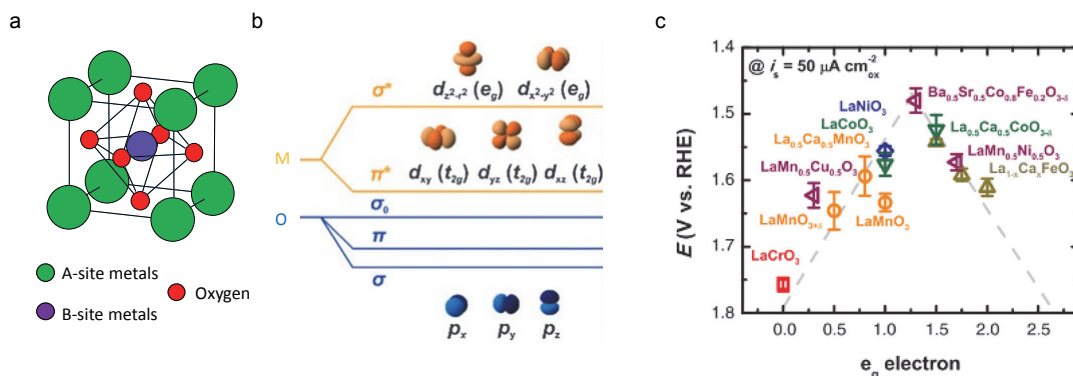


Figure 2.2. e_g occupancy as a descriptor for perovskites. (a) A unit cell of perovskite structure shows that the B-site metals are with octahedral coordination. (b) M 3d and O 2p orbitals form bonding (σ and π) and anti-bonding orbitals (σ^* and π^*). For octahedral coordination around the transition metal, the M 3d orbitals are split into e_g and t_{2g} states. Reproduced from ref. [11] with permission. © 2015 Royal Society of Chemistry. (c) The volcano plot of e_g electron versus potential (RHE) for different perovskite oxides. Adapted from ref. [12] with permission. © 2011 AAAS.

2.2.2 Bulk O 2p band center and metal-oxygen covalency

Even though the electron filling in e_g orbitals has been demonstrated as a useful activity descriptor in perovskite oxides for OER, the molecular orbital approximations can only be applied when the metal-oxygen bonds are nearly ionic. It cannot explain the different activity

of LaNiO_3 , LaCoO_3 , and LaMnO_3 where three perovskites possess the same e_g occupancy ~ 1 . The hybridization of the M 3d and O 2p bands should also be considered since the M-O bonds possess covalent nature [11,13,43]. Bulk band theory provides deeper and more complete insights into the OER catalytic activity of perovskite oxides and their mechanistic details. A schematic illustration of a bulk band diagram of metal and oxygen band hybridization is shown in Figure 2.3a. Suntivich and co-workers further proposed metal-oxygen covalency to describe OER activity [43]. By estimating the hybridization of metal and oxygen bands from O K edge in X-ray absorption spectroscopy, they defined the covalency parameter as $(hole_{e_g} + 1/4 hole_{t_{2g}})$. Greater covalency reflects that the active B-site cation has a larger O 2p character, enhancing the charge transfer between the active sites and adsorbates [12,43]. Figure 2.3b shows the influence of covalency on OER activity when the e_g occupancy of the reported oxides is ~ 1 . Grimaud *et al.* also reported that the computed O 2p band center relative to the Fermi level can be used as a descriptor for OER activity by correlating the experimental OER activities of cobalt-based perovskites as shown in Figure 2.3c [19]. Lee *et al.* demonstrated that the gap between O 2p-band center and Fermi level significantly correlates with surface oxygen exchange kinetics and oxygen absorption strength on the metal oxide surface [44]. Recently, Jacobs *et al.* reported on a strong linear correlation between the measured OER activity of perovskite oxides and the oxygen p-band bulk descriptor [20].

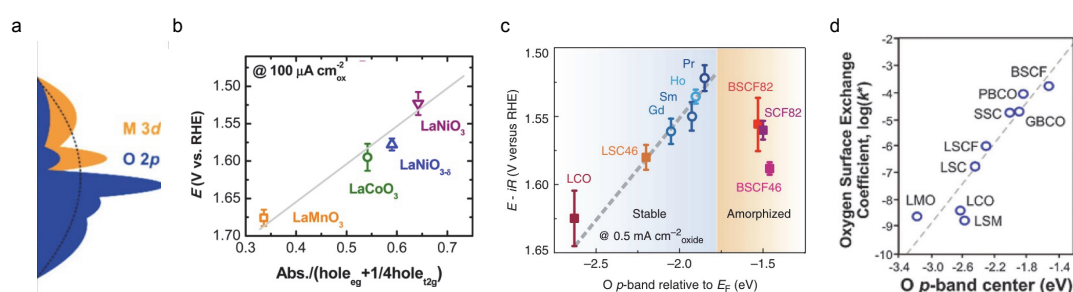


Figure 2.3. Bulk O 2p band center and metal-oxygen covalency. (a) Schematic illustration of perovskite density of state (DOS), orange = transition metal 3d and blue = O 2p on the basis of bulk band theory. Reproduced from ref. [11] with permission. © 2015 Royal Society of Chemistry. (b) OER activity plots against M-O covalency. Reproduced from [43] with permission. © 2014 American Chemical Society. (c) OER activity (potential at 0.5 mA cm^{-2}) versus the calculated O p-band center relative to the Fermi level for different perovskite oxides. Reproduced from ref. [19] with permission. © 2013 Springer Nature. (d) Correlation between the measured oxygen surface exchange coefficient and calculated O p-band center for different perovskites. Adapted from ref. [44] with permission. © 2011 Royal Society of Chemistry.

2.2.3 Surface stability of BSCF

The O 2p band center indeed provides a powerful perspective to describe perovskite oxide OER electrocatalysts. However, the OER activity cannot be fully explained by the bulk O 2p descriptor which is based on the assumption that the surface electronic structure is the same as in the bulk. If the surface that is responsible for OER activity is not what is claimed or surface reconstruction occurs, the bulk descriptors may not be applicable. For example, as shown in Figure 2.3c, the OER activity of BSCF does not scale with the O 2p band center. The reason for the deviation was studied by May *et al.* [38]. They reported surface amorphization and A-site dissolution of BSCF after cycling. Compared to TEM images of cycled and as-prepared LaMnO_3 (LMO), BSCF shows formation of amorphous layers on the surface after cycling (Figure 2.4). Thus, the amorphized surface layer on BSCF likely resulted in the deviation of OER activity using the O 2p band center as the descriptor. Although the bulk band descriptor fails to explain the OER activity of BSCF, the stability of the electrocatalysts is correlated to the O 2p band center. This was further explained by the positive correlation between O 2p-band center and oxygen vacancy formation energy: BSCF has a closer O 2p-band center (-1.5 eV) to the Fermi level than LMO so it is easier for BSCF to form oxygen vacancies, resulting in surface amorphization and A-site dissolution [38,45]. The structure change of BSCF has also been studied via X-ray absorption spectroscopy (XAS) techniques [37] where Risch *et al.* pointed out that the amorphization is associated with the increasing number of edge-sharing Co octahedral in BSCF.

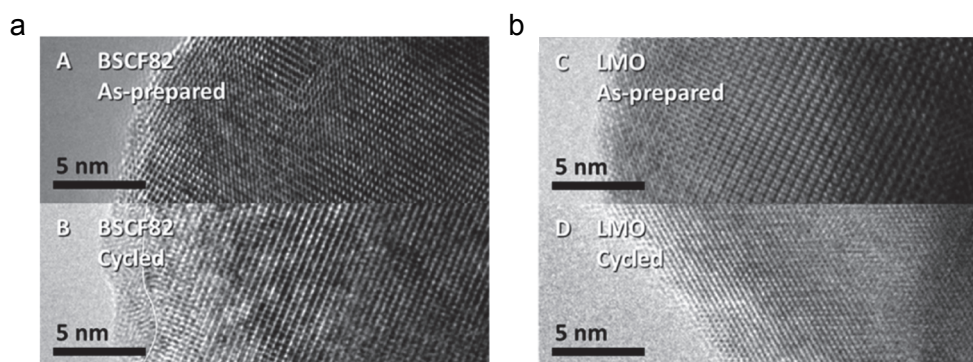


Figure 2.4. TEM images of as-prepared and cycled perovskites. (a) TEM images of A: as-prepared and B: cycled BSCF showed that amorphization on the surface of BSCF (b) TEM images of C: as-prepared and D: cycled LMO. Adapted from ref. [38] with permission. © 2012 American Chemical Society.

The surface stability of BSCF remains unclear despite its exceptional OER activity. BSCF is a perovskite that can accommodate a large number of oxygen vacancies [46] due to the low formation energy of oxygen vacancies [19,38]. In 2017, Han *et al.* demonstrated that the low energy penalty for oxygen vacancy formation in BSCF relates to high water uptake and high ion mobility [45]. The authors observed strong structural oscillations of BSCF in the presence of both water vapor and electron-beam irradiation using environmental TEM (ETEM) (Figure 2.5a). They claimed that the oscillation was related to the uptake of water vapor (Figure 2.5b) in BSCF due to formation of O₂. As seen in the electron energy-loss spectroscopy (EELS) in Figure 2.5c, BSCF in H₂O vapor showed an O₂ energy-loss peak, which is indicative of the generation of oxygen molecules under electron-beam irradiation. Overall, oxygen vacancies seem to explain well BSCF's surface stability. However, its OER activity still cannot be explained.

A new mechanism of OER in BSCF was proposed by Fabbri *et al.* in 2017 [35]. The authors claimed that dynamic reconstruction of self-assembled metal oxy(hydroxide) active layer on the BSCF nanoparticles is the reason for its high activity during OER. The formation of the oxy(hydroxide) oxygen was claimed to be due to lattice oxygen evolution reaction (LOER, oxidation of lattice oxygen), triggered by OER when the electrode is brought out of equilibrium [47]. The LOER at the perovskite surface also resulted in the dissolution of A-site cations ($\text{ABO}_{3-\delta} + \text{OH}^- \leftrightarrow \text{BO}(\text{OH}) + \text{A}^{2+} + \text{O}_2 + 3\text{e}^-$). The mechanism of self-reconstruction of the CoFeO(OH) active layer and the dissolution of Ba/Sr A-site cation is shown in Figure 2.5d. The ability of the structure to accommodate LOER is due to the flexibility of the perovskite structure, which is related to oxygen vacancies. The more vacancies, the more flexibility for the surface reconstruction, so the more active the perovskite oxides are as electrocatalysts for OER. Perovskite oxides with different oxygen vacancy content (δ) were compared in their studies. $\text{Ba}_{0.5}\text{Sr}_{0.5}\text{Co}_{0.8}\text{Fe}_{0.2}\text{O}_{3-\delta}$, $\delta \sim 0.75 > \text{La}_{0.2}\text{Sr}_{0.8}\text{CoO}_{3-\delta}$, $\delta \sim 0.4$ (LSC) $> \text{CoO}_{1-\delta}$, $\delta \sim 0.01$. BSCF with the largest number of oxygen vacancies showed the lower OER overpotential compared to LSC and CoO,

In short, BSCF was reported as a promising OER electrocatalyst in alkaline medium back in 2010s. The early reported e_g occupancy descriptor can explain the exceptional activity of BSCF among perovskite oxides but when it moved to a more generalized bulk O 2p band

center descriptor, BSCF OER activity seems to fail to scale with bulk band descriptor. It is noted that the use of the proposed descriptors to explain the OER trend of electrocatalysts is on the basis of the intrinsic, claimed surface. BSCF undergoes surface amorphization at the surface during OER so the bulk band descriptor does not apply. Finally, a more recent explanation on the basis of oxygen vacancies further describes the surface stability and OER activity of BSCF.

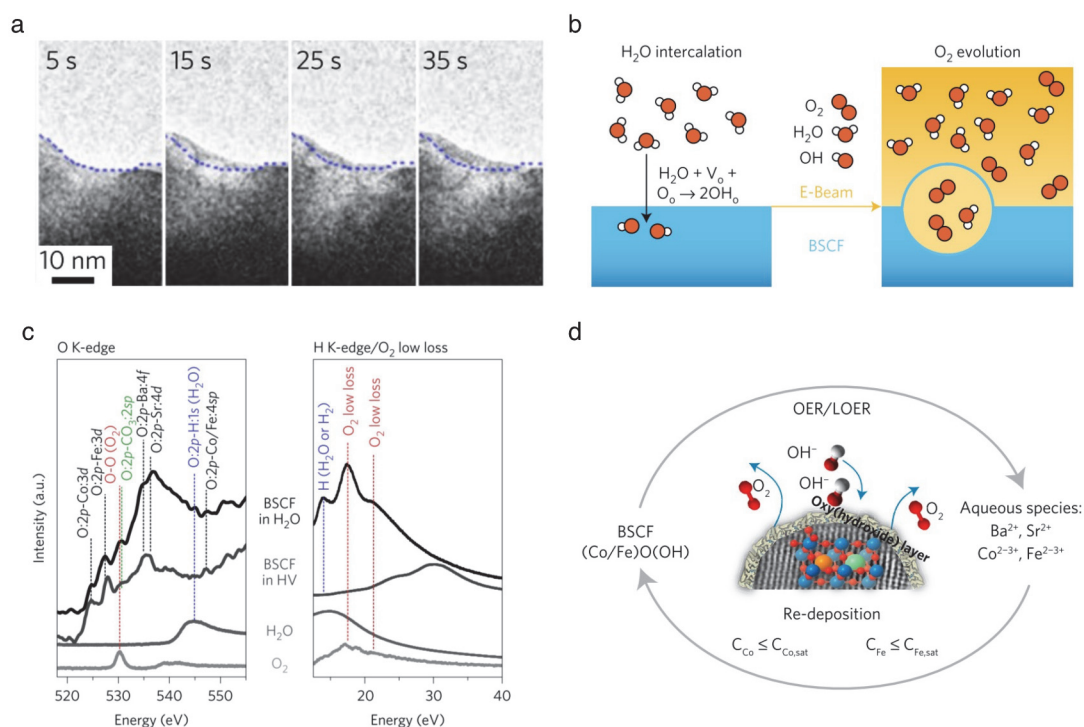


Figure 2.5. Surface stability of BSCF. (a) TEM images of structural evolution of the BSCF particle in water vapor under the electron beam. (b) Scheme of water uptake and oxygen evolution. Water uptake process occurred first to form hydroxyl groups and then hydroxyl groups were oxidized on lattice oxygen site into O_2 under the e-beam induced oxidative potential. (c) O K edge and low-loss EEL spectra of BSCF under different conditions. H_2O and O_2 reference EEL spectra are included. a-c Reprinted from ref. [45] with permission. © 2017 Springer Nature. (d) Proposed mechanism of formation of highly active $CoFeO(OH)$ surface layer and Ba/Sr A-site dissolution during OER/LOER. Reprinted from ref. [35] with permission. © 2017 Nature Springer.

2.3 Solid-liquid interfacial interactions

The solid-liquid interface is central to heterogeneous catalysis. Thus, following the discussion of the bulk and surface properties of OER electrocatalysts [48], the solid-liquid interfacial interactions are considered to broaden the understanding of OER electrocatalysis.

2.3.1 Charge transfer and surface restructuring

Charge transfer is a process that takes place at the solid-liquid interface in reactions involving electrocatalysts. It relates to the chemical adsorption/desorption of molecules or ions on the surface [49]. In particular for the surface of (110)-orientated RuO₂ single crystal surface interacting with molecules in acidic electrolyte [49], it has been reported that the redox peaks could be attributed to deprotonation of H₂O at the active sites of RuO₂ surface. In addition to chemical adsorption/desorption, surface restructuring during the electrocatalytic process is also induced by the charge transfer at the solid-liquid interface. For example, the aforementioned surface amorphization, A-site dissolution, and corner-sharing to edge-sharing of Co octahedra at the BSCF surface are related to charge transfer at the interface [37,38]. Surface restructuring during electrocatalytic operation conditions may play a role to enhance the activity of OER electrocatalysts, acting as a strategy to increase the number of active sites at the surface of the catalysts during the operation. The first example mentioned in the previous section was the dynamic surface reconstruction of BSCF proposed by Fabbri *et al.* [35]. Other than BSCF perovskite, Bergmann *et al.* reported that Co₃O₄ spinel structure reversibly transforms into amorphous CoO_x(OH)_y active surface layer at OER potential [50]. The surface transformation is closely related to the charge-transfer redox reaction at the surface. In general, the spinel structure consists of mixed valences: +2 in the tetrahedral sites (T_d) and +3 in the octahedral sites (O_h), with a 1:2 ratio, namely, [Co²⁺_(T_d)]₁ [Co³⁺_(O_h)]₂ in Co₃O₄. Two redox features are seen in the cyclic voltammogram of Co₃O₄ as shown in Figure 2.6a. The first one annotated A1/C1 refers to Co(II)/Co(III) while A2/C2 is Co(III)/Co(IV) redox reactions. Co²⁺_{T_d} ions of the crystalline Co₃O₄ in the near-surface get oxidized to +3 and change their coordination from tetrahedral to octahedral, resulting in the formation of the catalytic amorphous surface layer (Figure 2.6b). Co octahedral site, on the other hand, is inactive and

is not involved in oxyhydroxide phase transformation [51]. In addition to Co-based oxide OER catalysts, surface transformation at the solid-liquid interface was found in Ni-based OER catalysts. A typical example is the $\text{Ni}(\text{OH})_2/\text{NiOOH}$ transformation that is coupled to $\text{Ni}^{2+/3+}$ under potential cycling and NiOOH has been considered as an active phase for OER [52]. Thus, surface structure and surface interaction with the electrolyte are critical phenomena towards the understanding of OER electrocatalysts. The charge transfer process is one of the most important interactions for electrocatalytic OER in liquid. It can induce surface reconstruction and hence lead to active phase formation during OER.

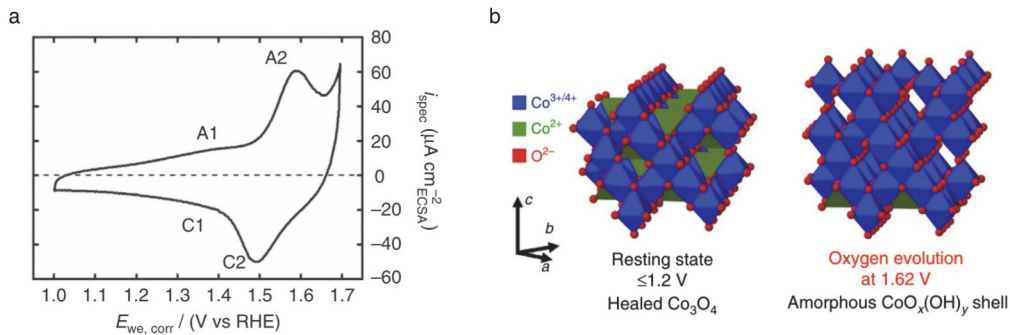


Figure 2.6. Surface restructuring on Co_3O_4 . (a) Cyclic voltammogram of Co_3O_4 . A1/C1 refers to $\text{Co}(\text{II})/\text{Co}(\text{III})$ while A2/C2 is $\text{Co}(\text{III})/\text{Co}(\text{IV})$ redox features. (b) Crystalline Co_3O_4 at resting state and amorphous $\text{CoO}_x(\text{OH})_y$ with Co octahedral coordination under OER potential. Both a and b are reprinted from ref. [50] with permission.

2.3.2 Surface wettability

In addition to the surface restructuring and charge transfer, one of the classic solid-liquid interactions is surface wettability. Typically, surface wettability is measured by the contact angle θ between a liquid droplet and solid surface, which is related to their interfacial tensions [53]. Three surface tensions depending on the interacting media need to be considered: solid-liquid (γ_{SL}), liquid-gas (γ_{LV}), and solid-gas (γ_{SV}). The equilibrium between these interfacial tensions determines the contact angle according to the equation:

$$\gamma_{\text{SV}} = \gamma_{\text{SL}} + \gamma_{\text{LV}} \cos \theta \quad (2.1)$$

This equation predicts that the more hydrophilic the surface is, the larger contact angle it has, and *vice versa*, as shown in the schematic illustration of Figure 2.7.

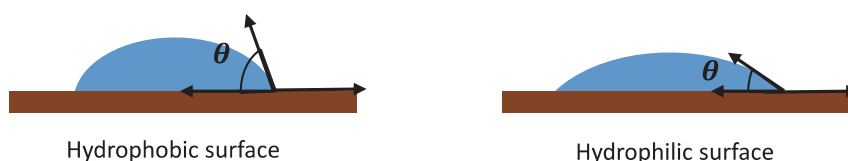


Figure 2.7. Contact angles (θ) of the hydrophobic/hydrophilic surface. Surface tensions balance between solid-liquid (γ_{SL}), liquid-gas (γ_{LV}), and solid-gas (γ_{SV}).

Application of external stimuli can also induce changes of the wettability of surfaces. In some cases, it can even be accomplished reversibly [54]. For example, switchable wetting induced by light illumination has been demonstrated on TiO_2 [55–57]. The formation of oxygen vacancies due to the illumination resulted in a reduction of the Ti oxidation state to +3, which led to the formation of the hydrophilic Ti-OH at the surface [56]. Other than light-induced hydrophilicity, electrical potential or temperature have also been demonstrated to adjust the surface wettability. It was shown that the wettability of a surface coated with a self-assembled monolayer (SAM) was altered under applied potential [58]. The switching configuration of the SAM layer has found to trigger the alteration of the wetting upon the application of the electric potential. Additionally, the temperature has been reported to induce hydrophilic/hydrophobic transition due to the modification of a thermal responsive polymer on surfaces [59].

Another way to adjust surface wetting is via electrowetting [60,61] which is induced by the alteration of surface tension at solid-liquid interfaces. When the electric potential is applied between a dielectric surface with a liquid, interfacial charges accumulate and form a capacitive system. Thus, the interfacial tension between the solid-liquid interface is altered due to capacitance formed. The change of the contact angle related to the interfacial capacitance is described by the Young-Lipmann equation assuming that the interfacial capacitance is a constant [60,61]:

$$\cos\theta - \cos\theta_0 \propto \frac{1}{2}cV^2 \quad (2.2)$$

where θ is the contact angle after application of the voltage V , θ_0 is the contact angle at equilibrium (at 0 V), and c is the capacitance at the solid-liquid interface. A schematic illustration of the electrowetting mechanism on a dielectric surface (EWOD) is shown in Figure 2.8. Typically, the applied potential to induce EWOD is relatively high (several tenths to several hundreds of volts) [60].

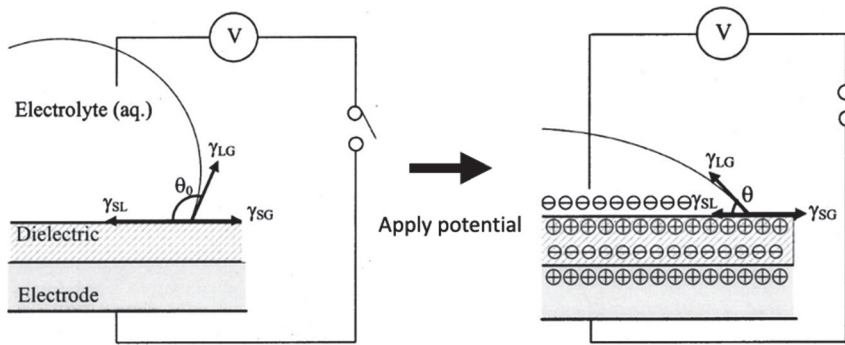


Figure 2.8. EWOD mechanism. The charges accumulate at the interface and adjust the contact angle when the electric potential is applied across the interface. Reproduced from ref. [60] with permission. © 2002 AIP Publishing.

Electrowetting can take place on conductive surfaces with much lower applied voltage. In typical electrowetting behavior occurring between conductor-liquid interface, the interfacial capacitance is determined by the charges of the electrical double layer. As the capacitance value is inversely proportional the thickness of the charged layer, a larger interface capacitance at the conducting surface can be produced than the one on a typical thick dielectric layer, resulting in lower voltage required to induce electrowetting [62]. The voltage can be as low as several volts on the conductive surface [62,63]. Ounnunkad *et al.* reported reversible electrowetting on the basal plane of graphite [64]. The range of the applied potential was lower than 1 V. They concluded that the interaction of water with graphite and the crystallinity of the material are responsible for the phenomenon of reversible electrowetting. In most cases, the interfacial capacitance is approximated to be a constant using the Helmholtz model of the

electric double layer [64]. However, constant capacitance is unrealistic due to the variation in electrode/electrolyte capacitance. Lomax *et al.* have measured the potential-dependent interfacial capacitance of graphite/LiCl_(aq) interface using AC impedance [62].

Additionally, electrochemical interactions or modifications at the solid-liquid interface can alter the interfacial capacitance and further influence electrowetting. Tang *et al.* reported that ion intercalation on a graphite surface induced pseudocapacitance, leading to the alteration of the electrowetting behavior [65]. Zehri *et al.* demonstrated active control of the wettability of copper oxide surface by switching the oxidation state of Cu electrochemically [66]. They showed that surface redox reaction at the Cu oxide surface can induce a change in the contact angle. Similar electrochemically induced modifications of surfaces have been demonstrated on liquid Ga by application of electric potential in alkaline medium and it was associated with the reversible formation of hydrophilic hydroxyl groups at its surface [67].

More importantly, wetting can influence the chemical properties such as catalytic performance. It has been reported that the effect of surface wettability is important for many aspects in heterogeneous catalysis such as activity, selectivity, and stability [68,69]. For example, surface functionalization like phosphorylation [70] and plasma treatments [71] have been shown to improve the hydrophilicity of NiFe hydroxide, a typical OER catalyst. Li *et al.* proposed that the enhanced electrochemical surface area after phosphorylation resulted in more catalytic active sites for water adsorption and oxidation [70] whereas Zhang *et al.* proposed that hydrophilicity of the surfaces promotes the charge-transfer rate between the electrolyte and electrode, and thus, leads to better OER activity [71].

2.4 Operando/*in situ* techniques for oxygen electrocatalysis

One of the central challenges in studying electrocatalysis is to understand their functionality and their activity, specifically, under operation conditions. In the past decades, researchers have developed a great variety of operando/*in situ* techniques to investigate the properties of electrocatalysts in real-time [72,73]. This section mainly focuses on X-ray based spectroscopy and (S)TEM based techniques as they have been applied for electrocatalytic studies.

2.4.1 X-ray based techniques

X-ray based techniques are the most widely used operando methods to study electrocatalysis under operation conditions. In this section, three X-ray based tools are covered: Ambient-pressure X-ray photon-electron spectroscopy (APXPS), X-ray absorption spectroscopy (XAS), and surface X-ray diffraction (SXRD).

2.4.1.1 Ambient-pressure X-ray photon-electron spectroscopy

XPS measures the emitted electrons that are excited by X-ray photons. The kinetic energy of the emitted electron reflects the electron binding energy. It is a surface-sensitive technique since the depth of penetration for photons and electrons is small and it is used to probe the surface electronic states such as coordination and valence of elements. Typically, XPS is performed in an ultra-high vacuum chamber which brings severe limitations to the application of operando/in situ analyses for electrocatalytic processes. Thus, ambient-pressure XPS has been developed using a combination of differential pumping systems and conical detectors close to the electrode surface which greatly reduces the limitation of ultra-high vacuum operating conditions [74]. In APXPS, a thin layer of the liquid electrolyte can be formed on the surface of electrocatalysts using the “dip-pull” method as shown in Figure 2.9a. Favaro *et al.* studied the chemical and structural evolution of different conformal CoO_x catalyst layers under OER with the condition that a thin liquid layer on the CoO_x surface is present [75]. They discovered the transformation of $\text{Co}(\text{OH})_2$ to $\text{CoO}(\text{OH})$ under precatalytic electrochemical conditions (Figure 2.9b). The limitation of the dip-pull method is the mass transport restrictions imposed by the thin-film electrolyte [72]. However, operando APXPS can provide information of surface electronic states and even reaction intermediates of the electrodes.

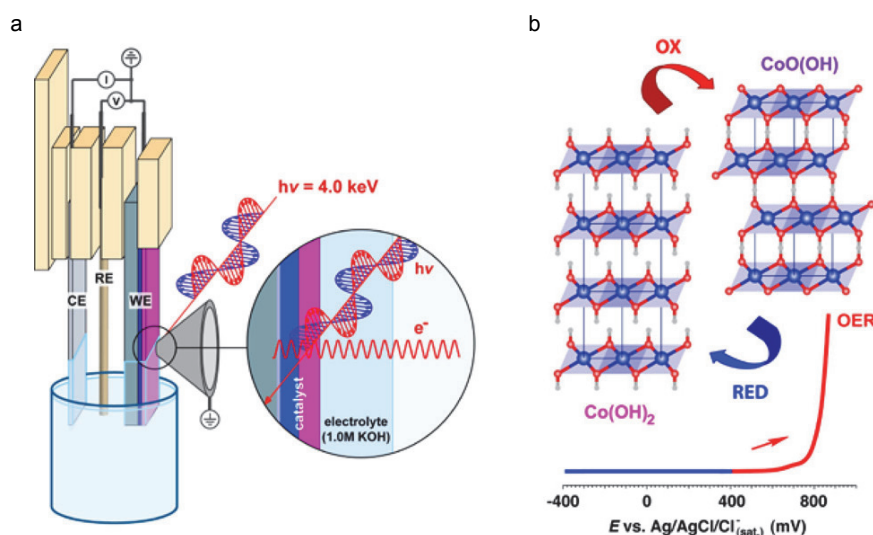


Figure 2.9. Operando ambient pressure XPS. (a) The dip-pull method to form a thin liquid layer at the electrode surface in operando APXPS. (b) Phase conversion of Co(OH)_2 to CoO(OH) under pre-OER condition. Reprinted from ref. [75] with permission. © 2017 American Chemical Society.

2.4.1.2 X-ray absorption spectroscopy

XAS measures the changes in X-ray absorption or fluorescence as a function of X-ray photon energy [76]. The X-ray energy is enough to excite core-level electrons to higher-level unoccupied states. The excitation process of the electron leads to absorption of the X-ray energy. XAS normally refers to an ionization edge of the electronic states of a specific element. For example, Co K edge represents the ionization process arising from the transition of a 1s electron to the unoccupied state of Co atoms. XAS can be separated into three regions: the pre-edge region, X-ray absorption near-edge structure (XANES, extending from the edge to about 50 eV), and extended X-ray absorption fine structure (EXAFS, extending from 50 eV and above up to 1000 eV). Depending on the edges and spectrum regions, XAS can provide a great variety of information of electronic structures ranging from valence, coordination, orbital filling, density of states, etc. It is a powerful tool to investigate the electronic structure and coordination environment of electrocatalysts, especially when it is applied under operation conditions [72,73,77]. In general, pre-edge and XANES regions reveal information of position/occupancy of orbitals, site symmetry, and oxidation state. The EXAFS region is further away from the ionization edge. It gives the information of bonding, near-neighbor distances, and coordination numbers. The signal originates from the interference between the outgoing and backscattered waves of photoelectrons ejected from the absorbing atoms. This

technique has been widely applied to OER electrocatalysts such as IrO_2 [78,79], NiFe oxyhydroxide [80,81], and Co-based oxides [82–84]. For example, in 2015, Friebel *et al.* systematically studied the highly active catalyst NiFeOOH for OER using operando Ni and Fe K edge XAS [81]. They showed that the shift of the pre-edge peak which reflects the 1s to 4p transition and the main absorption edge in Ni K-edge in XAS when the anodic potential applied was higher than 1.52 V, as shown in Figure 2.10a. The results suggested that Ni^{2+} oxidizes and this was associated with a structural change from $\text{Ni}(\text{OH})_2$ to NiOOH. Moreover, through EXAFS spectra, they revealed that the Fe–O bond distance in Fe–Ni hydroxides is smaller than in pure $\gamma\text{-FeOOH}$ while Ni–O remained identical under OER conditions. Instead of using K edge spectra, in 2021, Mefford *et al.* used Co L_3 edge XAS to probe the potential-dependent Co oxidation state of $\text{Co}(\text{OH})_2$ in combination with scanning transmission X-ray microscopy (STXM) (Figure 2.10b) [85]. They claimed that compared with determining oxidation state via edge position of K edge spectra, Co L edge spectra serve as fingerprints of the oxidation state and coordination environment around Co and can be easily identified by linear combinations of reference spectra. The evolution of Co L_3 edge operando XAS spectra under potential scan showed the trend of oxidation of Co^{2+} (Figure 2.10c) compared with the reference spectra of Co^{2+} , Co^{3+} , and $\text{Co}^{3.6+}$. The derived Co oxidation states are shown in Figure 2.10d using a linear combination method and fitting with an ideal solution model. Notably, no Co^{4+} is observed during OER according to their STXM-XAS characterizations.

Overall, operando XAS techniques probe the chemical and electronic states of the target catalysts under operation, providing invaluable multiple chemical and structural information of electrode materials during electrocatalysis. However, electrocatalytic reactions occur on specific surface-active site while the XAS analysis provides average information from samples. Thus, it exhibits some limitations on the mechanistic insights that can be revealed in site-specific catalytic reactions.

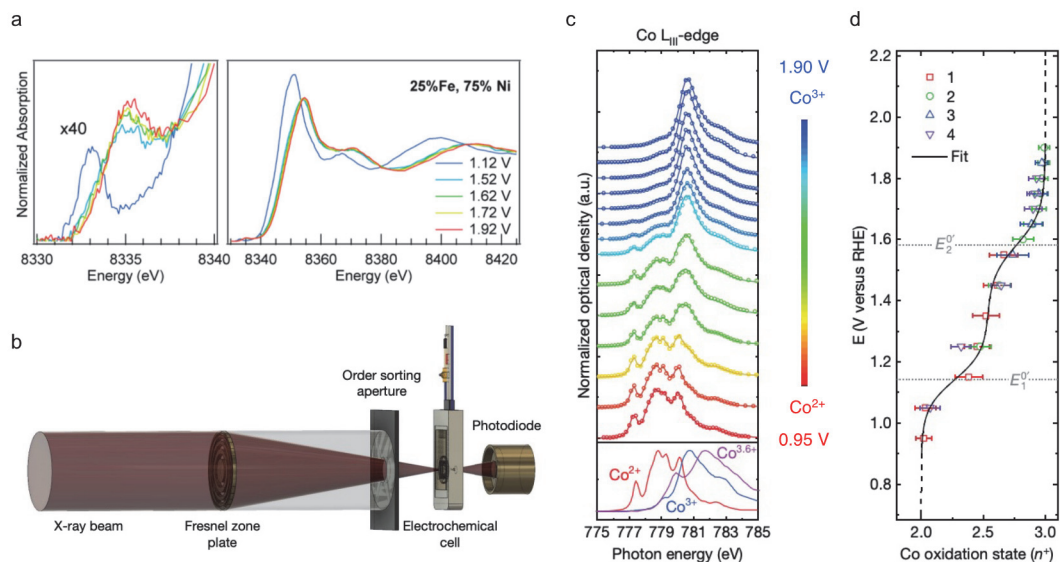


Figure 2.10. Operando XAS. (a) XANES of Ni K edge XAS of NiFe oxyhydroxide. Left Panel is zoom-in of pre-edge. Reprinted from ref. [81] with permission. © 2015 American Chemical Society. (b) Experimental setup of STXM-XAS. (c) Potential-dependent Co L₃ edge XAS spectra with reference β -Co(OH)₂ (Co²⁺), LiCoO₂ (Co³⁺) and Sr₆Co₅O₁₅ (Co^{3.6+}). (d) Co oxidation state of Co(OH)₂ plotted with potential vs RHE, with an ideal solution model fit. Reproduced from ref. [85] with permission. © 2021 Springer Nature.

2.4.1.3 Surface X-ray diffraction

Operando surface X-ray diffraction (SXRD) has been implemented for studying the surface structural changes under electrochemical conditions in the past decades [86–88]. Specifically, Reikowski *et al.* used operando surface X-ray diffraction technique to study Co oxide thin films, particularly Co₃O₄ (111) and CoOOH (001) [89]. By analyzing the out-of-plane grain size Δd_{\perp} with respect to the applied potential, they observed that CoOOH (001) (blue in Figure 2.11) remains stable in the applied potential range while a reversible structural change of Co₃O₄ (111) (red in Figure 2.11) occurs during potential cycling. They proposed that the observed potential-dependent restructuring of Co₃O₄ (111) is due to fast and reversible formation of a skin layer on the surface. The process reflects Co₃O₄/CoOOH transition at the potential 1.2 V versus RHE. The mechanism of the formation of a skin layer on Co₃O₄ (111) may be due to the displacement of Co²⁺ from tetrahedral to octahedral geometry site.

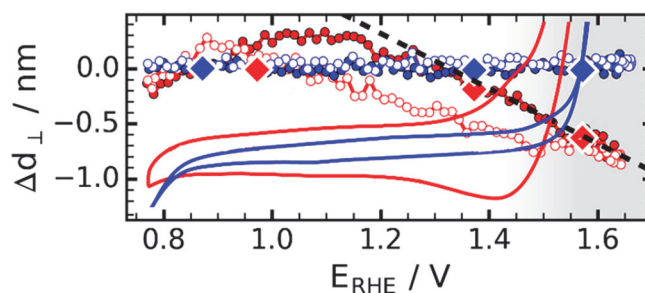


Figure 2.11. Potential-dependent out of plane grain size Δd_{\perp} . The red and blue represent Co_3O_4 (111) and CoOOH (001) thin films, respectively. Filled and open symbols refer to the positive and negative going potential sweep, respectively. The solid lines are CV curves. Reproduced from ref. [89] with permission. © 2019 American Chemical Society.

2.4.2 *In situ* (scanning) transmission electron microscopy

In addition to X-ray-based techniques, scanning transmission electron microscopy ((S)TEM) can also be used to image the morphological evolution of catalysts under working conditions. The main advantages of its implementation are the high spatial resolution, the ability to perform structural and chemical studies, and the unique ability to perform site-specific analysis (the detailed operation of electrochemical liquid-phase TEM (LP-TEM) will be discussed in Chapter 3). However, very few studies of oxygen evolving oxide catalysts have emerged thus far. Morphological and structural evolution of Co_3O_4 nanoparticles during OER conditions was recently reported using *in situ* electrochemical LP-TEM by Peña *et al.* [90] where an irreversible phase transformation of amorphous Co oxyhydroxide was observed. Crystalline Co_3O_4 nanoparticles were embedded in a matrix of amorphous Co oxyhydroxide-like phase (Figure 2.12a and b) after applying chronopotentiometry with high geometrical current. Their results contradicted the previously reported reversible structural modifications of Co_3O_4 [50,89]. This could be explained by the use of different electrochemical conditions. Their chronopotentiometry at relatively high current may induce irreversible phase transformation.

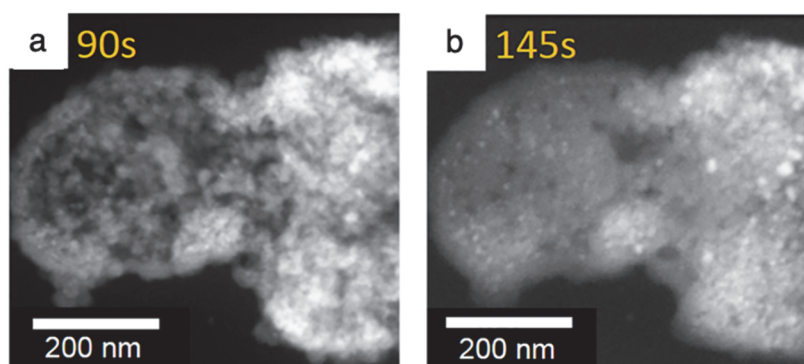


Figure 2.12. Co₃O₄ nanoparticles after chronopotentiometry. (a) *In situ* HAADF-STEM images of Co₃O₄ nanoparticles after 90s chronopotentiometry (10 mA/cm²_{GC}). (b) Formation of amorphous Co oxyhydroxide-like phase on Co₃O₄ after 145 s chronopotentiometry. Reproduced from ref. [90] with permission. © 2019 American Chemical Society.

Chapter 3 Methodology and Instrumentation

This chapter introduces the principles of the methodology and instrumentation implemented for obtaining the results of the thesis. It is noted that the main aspects of the instrumentation, necessary to understand the results of the thesis are included. A more detailed description can be found in refs. [91–93]. The first section (3.1) discusses the general background of (scanning) transmission electron microscopy ((S)TEM). Analytical electron energy-loss spectroscopy (EELS) under (S)TEM mode is covered in section 3.2 including descriptions of the principles, and its operation. The third section (3.3) covers the electrochemical liquid-phase TEM (LP-TEM).

3.1 Principles of (S)TEM

3.1.1 Overview of (S)TEM

An overview of a standard transmission electron microscope is shown in Figure 3.1a. Typically, the electron gun, i.e. the source of electrons, is a single crystal tungsten in a fine tip shape with a size a few tenths of nanometers. Due to the fine tip geometry, a strong electric field is created when anodic biasing (\sim kV range) is applied in front of the tip. The electrons are extracted from the tip using the electric field. This kind of electron gun is called field emission gun (FEG). To avoid oxidation of the W tip and maintain clean surface for field emission, ultra-high vacuum $\sim 10^{-10}$ torr is required in the FEG chamber. In this case the W tip is operated at ambient temperature and it is called cold FEG. Alternatively, the tip can be heated up and treated with ZrO_2 to improve the emission characteristics and it is known as

Schottky FEG, which is the most popular FEG currently. Cold FEG provides better spatially coherent electron beam meaning that a high energy resolution ~ 0.3 eV can be reached. Thermal assisted Schottky FEG gives greater stability of the electron source. After the electrons are generated from the electron gun, the electrons are further accelerated with high voltage (ranging from several tenth to several hundred kV) to achieve shorter wavelength λ , whose numerical value, taking into account relativistic effects, is given by the equation:

$$\lambda = \frac{h}{\sqrt{2m_0eV(1 + \frac{eV}{2m_0c^2})}} \quad (3.1)$$

where h is Planck's constant, m_0 is the electron rest mass, V is the accelerating voltage, and c is the speed of light. The acceleration process resulting in shortening the wavelength is the key to have extreme spatial resolution. As an example, for a TEM with 200 kV accelerating voltage, the wavelength of the electron is 2.5 pm.

Once the electron beam is generated, the electrons travel through a series of electromagnetic lenses and apertures, Figure 3.1a. The electromagnetic lenses control the path of the electron beam and they are used to deflect and/or focus the electron beam by altering the strength of the lenses depending on the operation needed. The apertures select the electron beam irradiation or control the convergent or collection angles during operation. The condenser lens system controls the condition and intensity of the electron-beam that illuminates the specimen. The following lenses typically are the objective, intermediate, and projector lenses (which will be discussed in the TEM subsection). Scanning coils are included in the column for the operation of scanning TEM mode. Eventually, the electrons are collected at the detector units after interacting with the specimen.

When the high energy electron beam interacts with thin specimen, it generates a wide range of secondary signal as shown in Figure 3.1b. Signals of transmitted electrons that penetrate the specimen such as directly transmitted electrons and forward scattered electrons are often collected using different detectors to perform imaging and diffraction. Analytical characterization such as energy dispersive spectroscopy (EDS) and electron energy-loss spectroscopy (EELS) can be performed by using the signals of X-ray and inelastic scattering

electrons, respectively. The following subsections describe the techniques of TEM, STEM imaging, diffraction, and EDS.

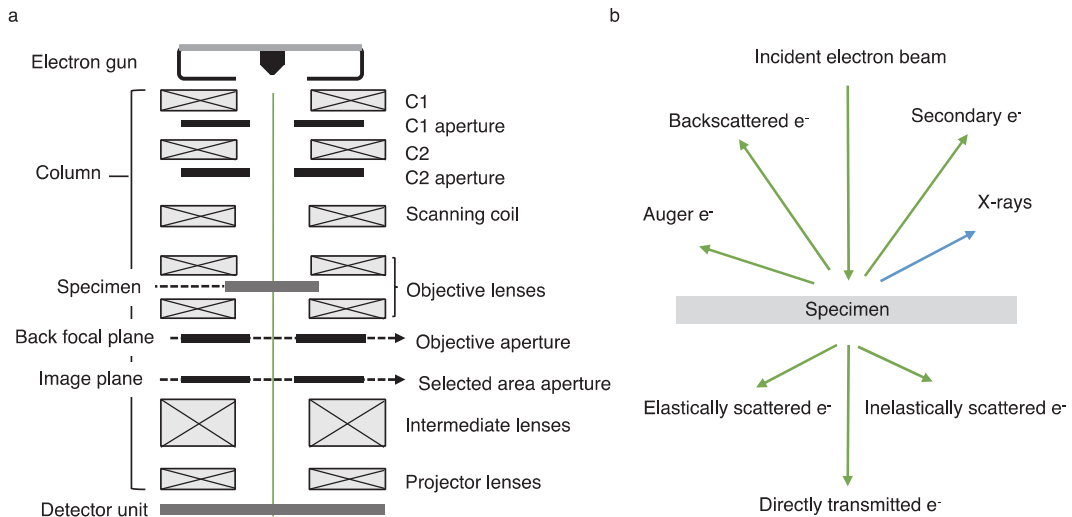


Figure 3.1. Overview of (S)TEM and electron-matter interactions. (a) Overview of a (scanning) transmission electron microscope. (b) Signals generated when a high-energy beam of electrons interacts with a thin specimen.

3.1.2 Principles of TEM operation in transmission mode

TEM mode is realized when a parallel and broad electron beam illuminates a thin specimen followed by collecting the transmitted electrons using detectors such as charge-couple devices (CCD) or complementary metal oxide semiconductor (CMOS). The illumination of the electron-beam is controlled by the condenser system of the microscope. The current of the electron beam can be tuned by adjusting the electromagnetic strength of the C1 which is related to the choice of spot size during operation. For large spot sizes, the crossover after C1 is higher so the electrons that pass through C2 are limited, resulting in a lower current of the electron-beam. C2 strength is related to whether the electron-beam converges on the specimen. C2 apertures determine the convergent angle α during the operation as shown in Figure 3.2a. The parallel illumination of the electron-beam can be achieved by underfocusing the C2 lens or using third condenser lens. The objective lens is responsible for image formation under TEM mode. It focuses the electrons emerging from exit surface of the specimen on the back focal plane (BFP). Under diffraction conditions on appropriate specimen, diffraction patterns are

formed on the BFP. Afterwards, the image is formed at the first image plane. To switch between TEM image mode and diffraction mode, the strength of the intermediate lens is modulated. The apertures that are placed on the image plane of the objective lens are selected area apertures. They are used to select the area for the diffraction patterns. The projector lens eventually projects the images or diffraction pattern onto the detector units. A schematic illustration of TEM image and diffraction modes are shown in Figure 3.2b. The image formation under TEM mode is based on the exit-plane wave which represents the electrons after interaction with the specimen. Thus, the contrast of TEM images is generated by the exit-plane wave. TEM contrast can be separated into amplitude contrast and phase contrast based on the wave properties of the electrons.

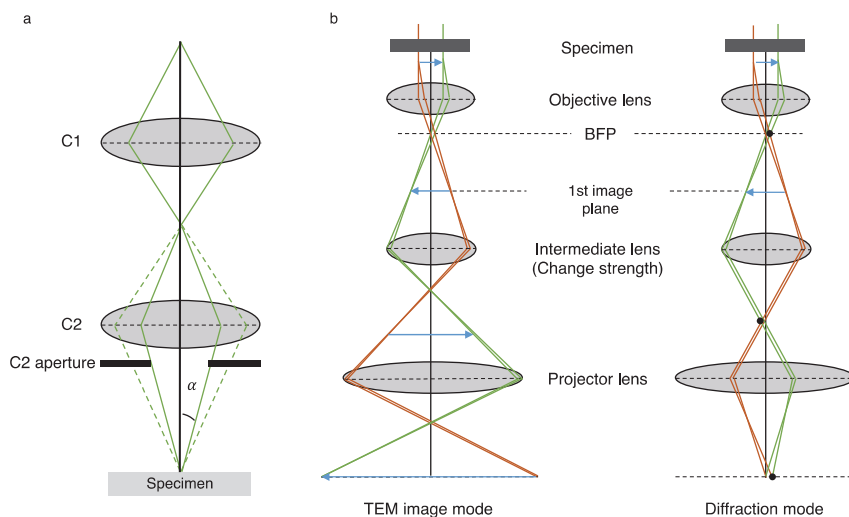


Figure 3.2. TEM and Diffraction operations. (a) A schematic illustration of how the C2 aperture controls the convergent angle α . (b) The ray path of the electron beam under TEM image mode and diffraction mode. The strength of the intermediate lens is stronger under TEM image mode.

The amplitude contrast represents the intensity difference of directly transmitted and scattered electrons. For thin specimen that elastic scattering is only considered, it consists of two principal types of elastic scattering: mass-thickness contrast and diffraction contrast. The mass-thickness contrast arises from the incoherently scattered electrons which represents Rutherford scattering. It reflects the thickness of the sample and it provides qualitative information about the atomic number Z of elements. A schematic illustration of mass-

thickness contrast is depicted in Figure 3.3a. The low mass-thickness region in the specimen results in low intensity, and *vice versa*. Diffraction contrast is related to the coherently scattered electrons that occurs at Bragg angles. In general, the image that is formed by collecting directly transmitted electrons is called bright-field TEM (BF-TEM). An objective aperture can be placed at the BFP to select the more centered direct transmitted beam. In this way, the amplitude contrast of BF-TEM can be improved. If the scattered electron-beam is selected by an objective aperture, a dark-field TEM (DF-TEM) images can be acquired. It is called dark-field as the scattered beam is selected so the contrast is inverted compared to BF-TEM. For example, a strong diffraction spot can be selected in a single crystal specimen to form a DF-TEM image which can be used to image defects. A schematic illustration of the manipulation of the objective aperture for achieving different amplitude contrast imaging conditions is shown in Figure 3.3b,c.

Phase contrast is generated by the phase difference of the exit-plane wave. The broad electron beam is described as a plane-wave. The exit-plane wave is thus the result of the interaction of the electron beam with the specimen and carries the structural information. On transmitting a crystalline specimen aligned to a zone-axis, the incident electron plane-wave undergoes diffraction. Each diffracted beam experiences a specific phase shift and forms a diffraction pattern on the BFP where a diffraction spot \mathbf{g} reflects a partial beam of wave vector $\mathbf{k}_{\mathbf{g}}$. Those diffracted beams interfere and form a phase contrast image. The simplest case of a phase contrast image is a lattice plane image. It is typically constructed by the interference of direct beams, \mathbf{g} and $-\mathbf{g}$. A lattice plane image then forms a set of lattice fringes where the periodicity reflects the d-spacing of lattice planes. Phase contrast depends on the transfer function of the objective lens which is related to defocus and spherical aberration. The periodicity of the lattice planes, that is, the d-spacing can be retrieved by mathematically applying a fast Fourier transform (FFT) to the HRTEM image.

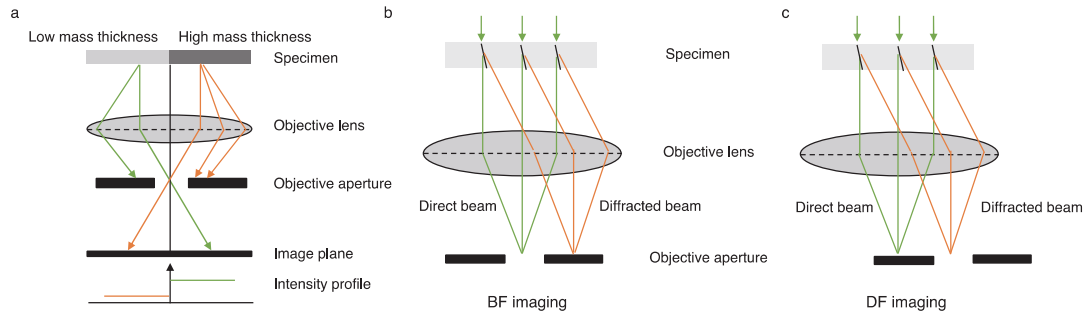


Figure 3.3. Mass thickness contrast and BF/DF TEM operations. (a) Mechanism of mass-thickness contrast in the BF imaging mode. Higher mass-thickness of the specimen leads to more elastic scattering, resulting in more scattered electrons being blocked by the aperture. (b) BF imaging mode. The direct beam is selected by the objective aperture. (c) Displaced the objective aperture to select diffracted beam for DF-TEM imaging.

3.1.3 Electron diffraction in TEM

Electron diffraction in TEM is based on Bragg's law. Considering a set of lattice planes with d spacing, the reciprocal lattice vector \mathbf{g} is given by:

$$|\vec{g}| = \frac{1}{d} \quad (3.2)$$

In the reciprocal space, the incident electron beam with a wavelength λ forms a vector with a value $1/\lambda$. The Bragg diffraction condition is satisfied when the value of momentum transfer in the diffraction is equal to a reciprocal lattice vector. Geometrical representation is shown in Figure 3.4. Thus, the reciprocal lattice points that match the Bragg conditions appear in the electron diffraction pattern. The most common electron diffraction technique is selected-area electron diffraction (SAED) based on a parallel electron beam illumination. The use of a selected-area aperture at the first image plane confines the region of interest for the diffraction. Although the selected-area aperture is physically located under the specimen, it acts virtually like an aperture above the specimen to select the region of interest. The area of selection depends on the size of the apertures. Typically, the selected area can be as small as several hundred nanometers. SAED pattern is useful for the overall inspection of the crystal structure. The polycrystalline structure appears to be ring SAED patterns due to a random direction of \mathbf{g} vectors. Single crystals form dotted SAED patterns depending on the symmetry of the crystal and the zone-axis.

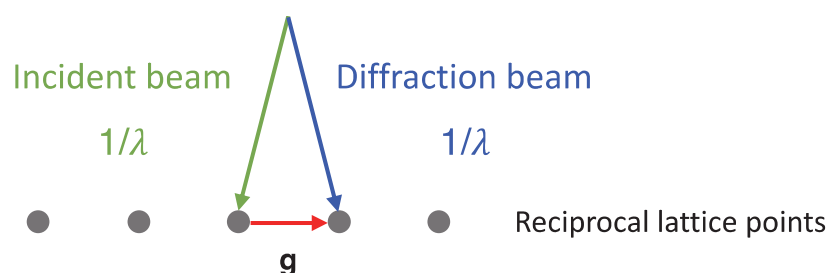


Figure 3.4. Electron diffraction in TEM. The electron diffraction occurs when the Bragg condition is satisfied. The reciprocal lattice vector is equal to the momentum transfer of incident beam and diffraction beam.

3.1.4 Principles of TEM operation in scanning transmission mode

In conventional STEM mode, the electron beam is formed into a small probe (on the sub-nanometer level size) that is converged using the condenser lens or upper objective lens above the specimen, Figure 3.5a. To form an image in scanning transmission mode, the electron probe is scanned across the specimen using scanning coils and the signal of the transmitted electrons are collected to form a raster STEM image. Detectors are placed underneath the specimen to collect the signal of the scattered electrons. A bright-field (BF) detector collects the directly transmitted beam and an annular dark-field detector (ADF) is used to collect the scattered electrons. When the elastic scattered electrons with high scattering angle are collected, it forms high-angle annular dark-field STEM (HAADF-STEM) images.

The signal of the incoherently elastic scattered electrons is highly sensitive to variations in the atomic number (Z) of the atoms in the specimen where the intensity of the scattered electrons is proportional to Z^α ($\alpha=1.2-1.8$) [94,95]. The contrast in the HAADF-STEM image originates from mass-thickness contrast. To collect the electrons with different scattering angles, the camera length is adjusted. The camera length refers to the virtual distance between the specimen and the detector. Short camera lengths correspond to high angle of scattered electrons that can be collected.

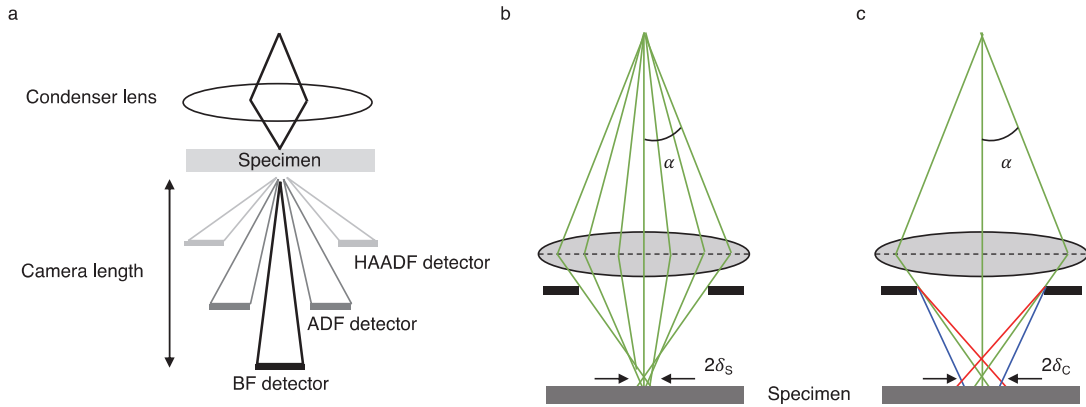


Figure 3.5. Principles of STEM. (a) A converged electron-beam illuminates on the specimen under STEM mode. (b) The effect of the spherical aberration in a lens. α and δ_s are the illumination angle and the radius of the broadening probe due to spherical aberration, respectively. (c) The effect of the chromatic aberration. δ_c is the radius of the broadening probe due to chromatic aberration.

STEM imaging can be performed on thicker samples due to the better penetration of the converged probe of electrons. It also provides better depth of focus than the one in transmission mode. The major advantage of STEM over TEM mode is the site-specific sub-nanometer electron beam irradiation that offers the capability to probe local information. In combination with analytical analyses such as electron energy-loss spectroscopy (STEM-EELS) and energy dispersive spectroscopy (STEM-EDS), chemical state, valence, and elemental composition maps other than imaging can be realized.

The spatial resolution in STEM is determined by the probe size of the electron-beam. The electron probe on the specimen plane is formed by the condenser or upper objective lenses. The electron probe size, excluding lens effects, is defined as the diffraction limit which is determined by the Rayleigh criterion, which associates the wavelength to the radius of the airy pattern [93]

$$\delta_D = 0.61 \frac{\lambda}{\alpha} \quad (3.3)$$

where α is the illumination semi-angle as shown in Figure 3.5b and λ is the wavelength of the electron beam. Eq. (3.3) gives the theoretical limit of the electron probe size. However, the imperfection of the lenses leads to broadening of the electron probe. This is known as

aberrations. An important effect that leads to smearing of the size of the STEM probe is spherical aberration. It concerns electrons that are initially further away from the optical axis of the lenses being bent by the lenses closer to the axis, as shown in Figure 3.5b. The broadening of the electron probe due to spherical aberration is δ_s and it is given by:

$$\delta_s = \frac{1}{4} C_s \alpha^3 \quad (3.4)$$

where C_s is the spherical aberration coefficient. Another important lens effect is chromatic aberration. It arises from the fact that the focal point of the lens depends on the energy of the electrons. The broadening effect of the chromatic aberration δ_c is shown in Figure 3.5c and it is described by:

$$\delta_c = C_c \frac{\Delta E}{E} \alpha \quad (3.5)$$

where C_c is the chromatic aberration coefficient, E is the energy of the incident electron beam, and ΔE is the energy spread of the electron beam. Thus, the electron probe size in STEM is defined by the three effects and can be expressed by:

$$\delta = \sqrt{\delta_D^2 + \delta_s^2 + \delta_c^2} \quad (3.6)$$

Using parameters for a conventional STEM ($C_s = 1$ mm, $C_c = 1$ mm, $\lambda = 2.5$ pm, $E = 200$ KeV, $\alpha = 10$ mrad, and $\Delta E = 1$ eV), a resolution $\delta = 0.3$ nm can be achieved. Recent advancements of probe-type C_s correction in STEM reduces the C_s value down to micrometer levels and gives sub-angstrom resolution. It is noted that the chromatic aberration is not the limiting factor for the resolution in conventional STEM since δ_c is several times smaller than δ_s and δ_D .

3.1.5 EDS

Energy dispersive spectroscopy involves characteristic X-rays that are emitted after the incident electrons interact with the specimen. The characteristic X-rays are generated in a two-step process during the interaction. As illustrated in Figure 3.6, first the incident electrons knock off the inner shell electrons that are bound to the nuclei. Then the outer shell electrons recombine with the hole, and the process emits the characteristic X-rays. The energies of the X-rays are characteristic of the difference in energy between the two shells and of the atomic structure. Thus, the technique is particularly useful for identification of elemental composition of samples. The relative ratio of two elements in a specimen can be quantified using EDS quantification. The ratio of two elements A and B is expressed by

$$\frac{C_A}{C_B} = k_{AB} \frac{I_A}{I_B} \quad (3.7)$$

C_A and C_B can be weight percent or atomic ratio of A and B elements in the specimen. Thus, $C_A + C_B = 100\%$. I_A and I_B are intensities of characteristic X-rays after background subtraction of A and B elements, respectively. k_{AB} is the sensitivity factor and varies with different pair of elements. To determine the k factor experimentally, a standard sample with known composition is used. Once the k-factor is defined, the atomic ratio of elements in the specimen can be quantified. In an ideal case, the Cliff-Lorimer ratio technique assumes that the specimen is thin enough so the absorption and fluorescence of the characteristic X-rays are negligible.

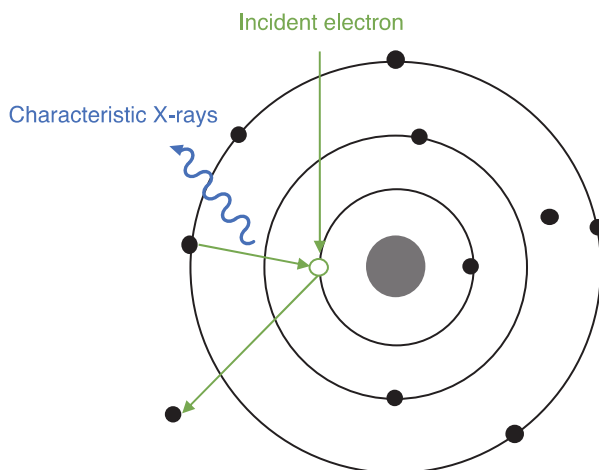


Figure 3.6. Generation of characteristic X-rays.

3.2 Electron energy-loss spectroscopy (EELS)

3.2.1 Physics of EELS

EEL signal has to do with the energy of the electrons that is lost when they interact with matter. From an atomic point of view, as shown in Figure 3.7a, the incident electrons collide with the atoms and an inelastic scattering event occurs as a result of Coulomb interaction between fast incident electron and electrons that surround the nucleus. The inelastic scattering event leads to energy transfer processes. The kinetic energy of the incident electrons E_0 is reduced by a certain amount of energy ΔE that is equal to the binding energy and kinetic energy of the ejected electrons. Thus, the energy-loss term in EEL spectra comes from the difference ΔE . As a vector representation, a schematic illustration of the process is shown in Figure 3.7a. The momentum p and energy E_0 of the incident electron are expressed by:

$$p = \hbar k_0 \quad (3.8)$$

$$E_0 = \gamma m_0 c^2 \quad (3.9)$$

where m_0 , \hbar , c , γ , and k are the rest mass of electron, Planck constant, velocity of light, and the wavefactor of the incident electron, respectively. If the incident electron is scattered by θ and the momentum is changed to k_f , the change of momentum, also known as scattering vector, is $\vec{q} = \vec{k}_0 - \vec{k}_f$. According to the conservation of momentum, the relationship of the scattering vector is:

$$q^2 = k_0^2 + k_f^2 - 2k_0 k_f \cos\theta \quad (3.10)$$

As the scattering angle θ is relatively small, $\ll 1$ rad and typically less than 100 mrad, the magnitude q of the scattering vector is approximated by the expression:

$$q^2 \approx k_0(\theta^2 + \theta_E^2) \quad (3.11)$$

where θ_E is the characteristic inelastic scattering angle corresponding to the average energy-loss of the incident electron, that is, $\Delta E/2$:

$$\theta_E = \frac{\Delta E}{2E_0} \quad (3.12)$$

The detail derivation of the magnitude of the scattering vector and characteristic angle can be found in Egerton's EELS textbook [92]. The inelastic scattering from solids can be described using bulk band diagram. The inelastic scattering of the incident electrons in the solid can be seen as the ionization process of the electrons in the solid. The high energy incident electrons ionize the occupied electrons to unoccupied states in the band energy diagram, Figure 3.7b. The ionization energy is thus related to the energy-loss of the incident electrons.

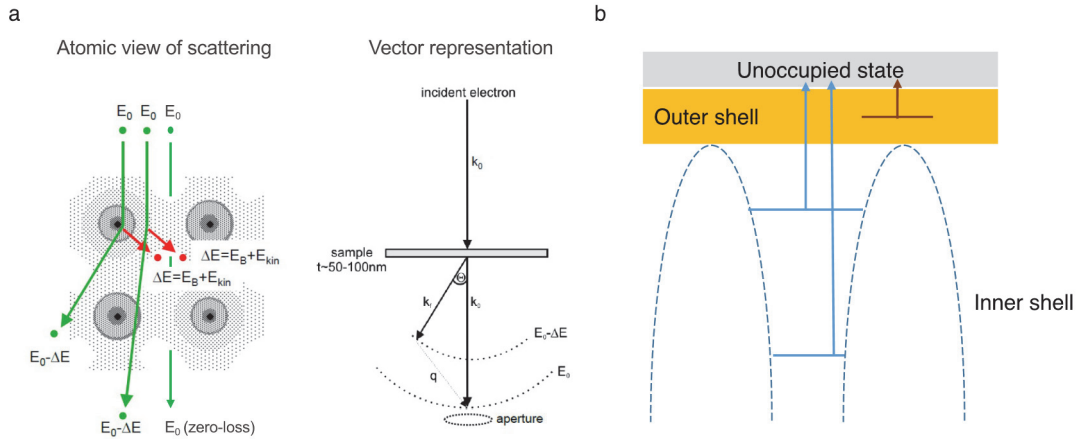


Figure 3.7. Inelastic scattering event in EELS. (a) Left: atomic view and right: vector representation. (b) Energy diagram in a solid. The blue arrows and brown arrow indicate the ionization process of inner shell and outer shell, respectively.

In a typical EEL spectrum, the energy-loss of the incident electron is plotted against its intensity, Figure 3.8a. Most electrons penetrate the specimen without inelastic scattering and hence the most pronounced feature in an EEL spectrum is the zero-loss peak. The full width at half maximum (FWHM) of the zero-loss peak reflects the coherency of the incident electrons and this is defined as energy resolution. Energy resolution is crucial for EELS. It determines whether the fine structure in the spectra can be resolved. Typically, a Schottky field emission gun (S)TEM (without exciting a monochromator) gives 1.1 eV FWHM of zero-loss peak using 0.1 eV/ch as dispersion. The energy resolution of a cold FEG can be as low as 0.3

eV. These values are enough to resolve the chemical shift of two oxidation states and pre-peak features in the core-loss EELS. The zero-loss peak intensity represents the probability of inelastic scattering when the incident electrons travel through the specimen and it can further provide information on the relative thickness of the specimen. If t is the specimen thickness and λ is the mean free of the inelastic scattering, the relative thickness t/λ is $\ln(I_t/I_0)$ where I_t and I_0 is the total integrated intensity and zero-loss peak integrated intensity, respectively.

The energy-loss region which represents electron scattering by phonons follows the zero-loss peak. This region normally merges with the zero-loss peak due to the fact that the energy-loss of phonon excitation is quite small. The typical inelastic scattering part in EELS has two main regions: low-loss and core-loss. The low-loss regime is within an energy-loss below 50 eV while core-loss ranges from 50 eV to 4000 eV. The low-loss regime in EELS provides information of inelastic scattering of outer shell electrons such as ionization of valence electrons which have reduced ionization energies. The inelastic scattering of outer electrons can also involve plasma resonance. The excitation process can be described as interaction with a plasmon pseudoparticle whose energy is $\hbar\omega_p$ where \hbar is Planck's constant and ω_p is the plasmon frequency. In thicker samples, the transmitted electron is inelastically scattered more than once. This effect is referred to plural scattering. In the case of the plasmon scattering, it forms a series of peaks at multiple plasmon energies. In most cases, plural scattering is unwanted and it is removed or deconvolved from the spectra to assist the interpretation of the results.

The core-loss regime is related to the ionization process of the electrons from the inner-shell resulting in a larger energy-loss. As the empty states are continuous, the ionization of the inner shell electrons forms an edge lying on the background in the core-loss EELS. The ionization edge is element and electronic state dependent. The nomenclature of ionization edges in EELS is shown in Figure 3.8b. For example, if the inner shell electrons of Ni are ionized from 2p to unoccupied states, it is called Ni L edge in EELS. Thus, the core-loss EELS provides information of inner shell electrons and elements in the specimen.

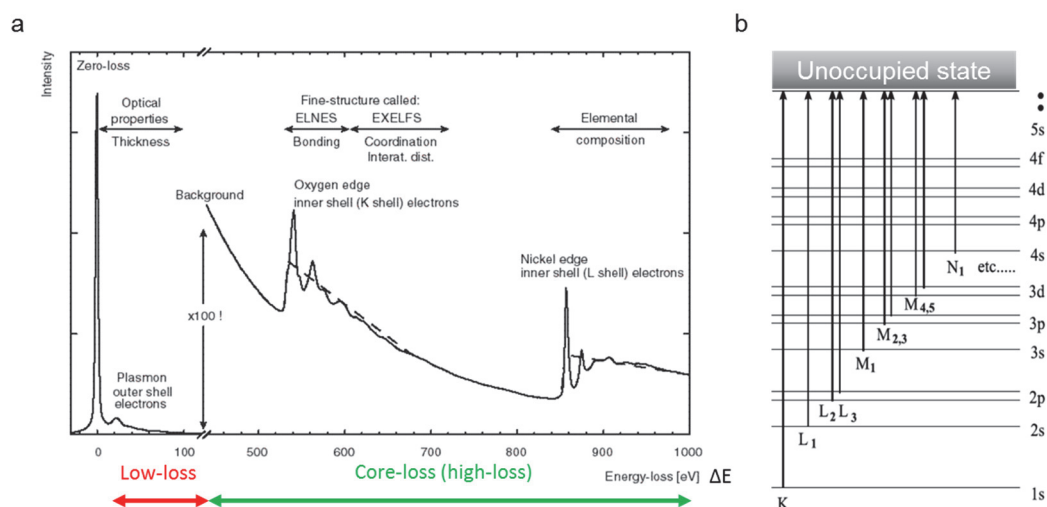


Figure 3.8. EELS spectrum and nomenclature of edges. (a) EELS spectrum includes zero-loss, low-loss, and core-loss spectrum. (b) Nomenclature of EELS edges of the transition of inner shell electrons to unoccupied state.

The core-loss region of the EEL spectrum contains information about the density of unoccupied states in the valence or conduction band and specifically this is represented in the energy-loss near edge structure (ELNES). A classic example of the ELNES is white lines in the L edge that represent 2p to unoccupied 3d states of the first-row transition metals. Due to the spin-orbit coupling, the 2p state splits into two levels: $2p_{3/2}$ (L_3) and $2p_{1/2}$ (L_2). The transition of split 2p states to narrow 3d unoccupied state forms two strong peaks, i.e., white lines, lying on the L edge. Figure 3.9a shows EEL spectra of $L_{3,2}$ edge of the first-row transition metals. The white line features become less discernible when the atomic number increases, directly reflecting the 3d unoccupied state. Cu shows no white line features. This is due to the fact that $3d^{10}$ is fully occupied so the white lines are not visible [96]. Additionally, oxidation states of the transition metals or metal oxides can be acquired on the basis of the energy shift or intensity ratio of the white lines [97]. The peak shift in the white line is also called chemical shift, which involves both the initial and final states of a core-electron transition. Qualitatively, a higher the oxidation state means fewer outer the electrons, which leads to stronger screening effect of electron excitation. Thus, the bound electron feels more binding from the nuclei, resulting in larger energy-loss of incident electrons after interaction. The intensity ratio of the two white-lines reflects the degeneracy ratio of the initial state $2p_{3/2}$ (L_3) and $2p_{1/2}$ (L_2).

However, due to spin-spin coupling, the white-line ratio depends on the number of electrons in the final 3d state and therefore varies with atomic number and oxidation state. Variation of intensity ratio and chemical shift of white-lines in different transition metal oxides are shown in Figure 3.9c. It is shown that the L_3 edge of Mn^{4+} has larger energy-loss than Mn^{3+} by 3eV. The L_3/L_2 white line ratio is also lower in Mn^{4+} .

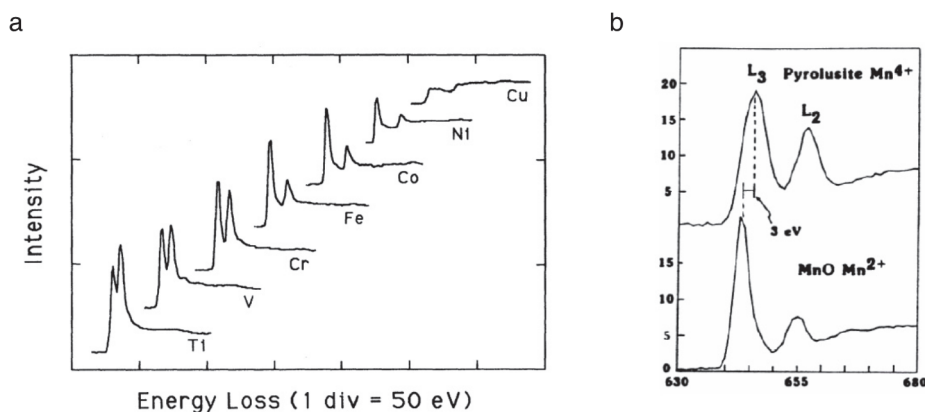


Figure 3.9. Core-loss EELS. (a) EELS $L_{3,2}$ edges for the 3d transition metals. Reproduced from ref. [96] with permission. © 1993 American Physical Society. (b) Alteration of intensity ratio of white lines and chemical shift of Mn with different oxidation states.

3.2.2 EELS acquisition

Finally, some information on some practical aspects of EELS acquisition is given. The spectrometer that collects the EEL signal is typically mounted post-column, Figure 3.10, where the back focal plane of the projector lens is used as the object. The EELS spectrometer includes a prism to split the electrons with different energy. After dispersion, the electron beam passes through a series of electromagnetic lenses placed after the prism. Finally, the electrons reach the detector and form an EEL spectrum. For EELS acquisition in practice, both convergent (α) and collection (β) semi-angles should be considered. A schematic illustration of α and β is shown in Figure 3.11a. Convergent angle represents how the electron beam converges to the specimen. It is normally determined by C2 aperture and the strength of condenser lens in the (S)TEM. Collection semi-angle represents how the electron get into the EEL spectrometer and it is determined by the EELS entrance aperture (in diffraction mode)

and camera length (CL). In STEM, the collection semi-angle β is defined by the entrance aperture radius divided by the camera length. Thus, by increasing the size of entrance aperture or by reducing the CL, β can be increased. It is noted that for quantification the partial cross section is affected by both α and β . Typically, for optimization of EELS collection, it is better to have large collection semi-angle to increase the intensity and signal-to-noise ratio. However, too large β results in compensating for energy resolution and signal-to-background ratio. The actual optimized collection angle depends on the specimen and can vary between microscopes.

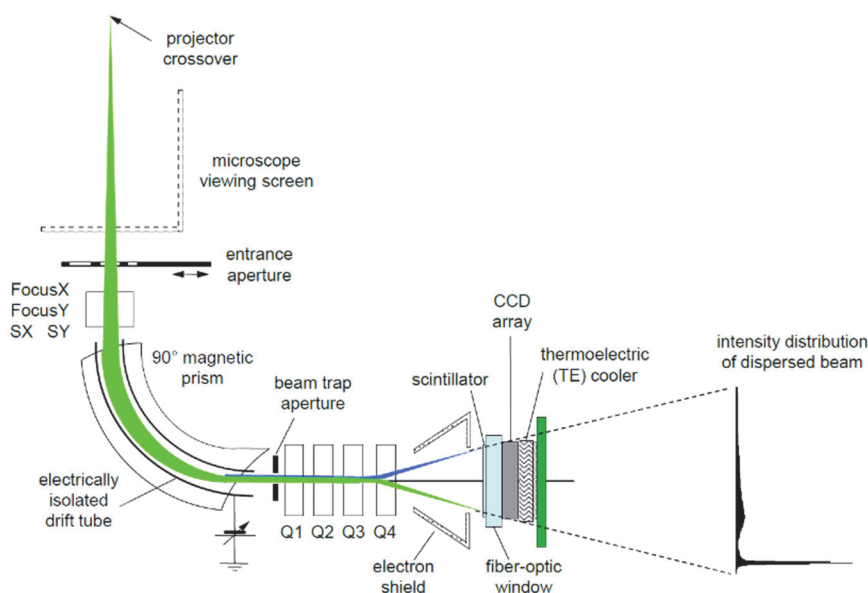


Figure 3.10. A schematic illustration of a post-column EELS spectrometer.

Regarding the acquisition mode in EELS, the electron beam can be located at specific position and collect EEL spectra in STEM mode. Alternatively, spectrum imaging can be performed to provide xy spatial information as well as EELS. In STEM spectrum imaging, the electron beam rasters on the specimen and EELS is collected on each pixel, rendering a three-dimension dataset with x, y, and ΔE as shown in Figure 3.11b.

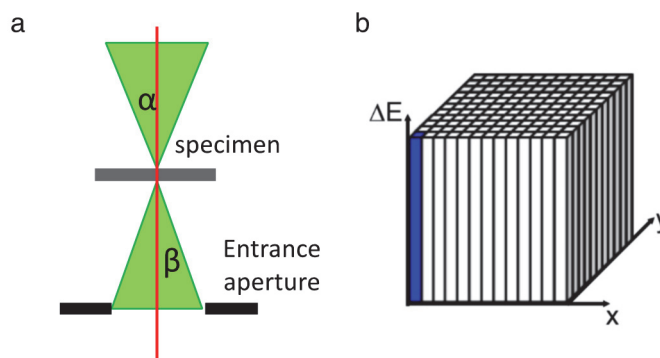


Figure 3.11. Convergent and collection angles and spectrum imaging. (a) A schematic representation of convergent (α) and collection (β) semi-angles. (b) EELS spectrum imaging data dimension under STEM mode.

3.3 Electrochemical liquid-phase (S)TEM

3.3.1 Background and principles of electrochemical liquid-phase (S)TEM

To enable *in situ* observation of liquid specimen in (S)TEM while maintaining the TEM column in high vacuum conditions (typically around 10^{-5} to 10^{-7} mbar) and simultaneously having electron transparent area for observation, well-developed micro-electro-mechanical systems (MEMS) with ultra-thin SiN_x membranes are typically utilized [98–101]. The suspended silicon nitride membranes also fulfil the electron transparent capability. The sealed cell of liquid specimen was first reported in 2003 for imaging the electrochemical applications and it involved imaging of Cu electrodeposition in aqueous electrolyte, published by Ross *et al.* [102]. They have further studied nucleation and growth in electrochemical processes [103–105]. After the capability of the electrochemical liquid-phase (S)TEM was demonstrated, many other electrochemical applications such as electrochemical etching [106], fuel cell [107,108], electrocatalysis [90,109–112], and lithium-ion batteries [113–115] have been reported.

An illustration of the TEM holder used to perform electrochemical LP-(S)TEM herein is shown in Figure 3.12a. Its tip can accommodate MEMS chips to seal the liquid. The liquid electrolyte is usually introduced into the reaction cell from the outside through integrated microfluidic tubing. Biasing can be performed by connecting the thin film electrodes on the

MEMS chips through external cables to a potentiostat. Typically, a liquid cell in (S)TEM is formed by sandwiching two chips, as shown in the cross-sectional view of the assembly in Figure 3.12b. Two o-rings are placed in between to seal the liquid and avoid breaking the vacuum of the TEM column. The top chip usually includes microfabricated thin-film metallic or glassy carbon electrodes to enable electrochemical measurements while the bottom chip has spacers to support the top chip, letting liquid flow through the membrane region. The thickness of the spacer ranges from several tenths of nanometers to several micrometers.

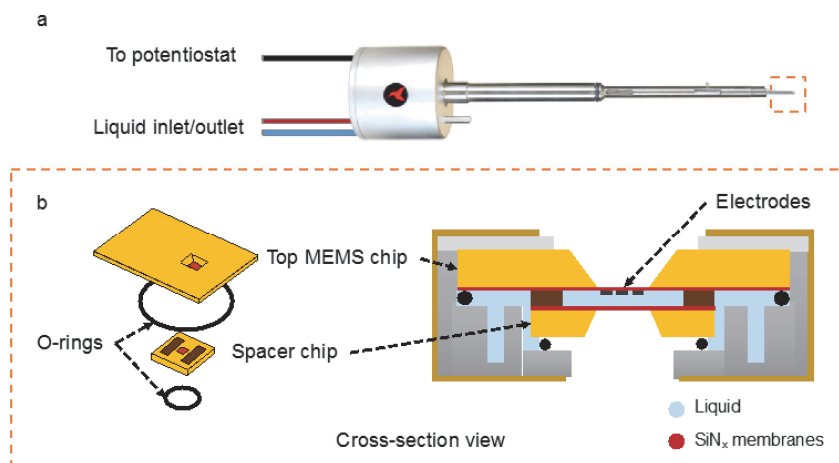


Figure 3.12. Liquid-phase TEM apparatus. (a) Electrochemical liquid-cell TEM holder used herein. (b) Zoom in and cross-section view of the liquid-cell assembly on the tip of the TEM holder.

3.3.2 Spatial resolution in LP-(S)TEM

The spatial resolution of LP-TEM has been theoretically and experimentally studied previously [101,116,117]. For thick specimen in which inelastic scattering strongly occurs, the chromatic aberration in the objective lens dominates the spatial resolution in LP-TEM and is described by:

$$d = \frac{1}{2} C_c \frac{\Delta E}{E} \beta \quad (3.13)$$

where β , C_c , ΔE , and E are semi-angle of objective aperture, chromatic aberration of objective lens, energy spread due to inelastic scattering, energy of the electrons, respectively. ΔE can be

calculated by the inelastic scattering cross section [116]. In the case of liquid water, for example, the spatial resolution in LP-TEM can be estimated by the following equation [101,116]:

$$d_{TEM,water} = 6 \times 10^{12} \beta C_c \frac{t}{E^2} \quad (3.14)$$

where t is the liquid thickness. The thickness of the nitride window is neglected, and the typical parameters of LP-TEM operation conditions are used ($\beta = 10$ mrad, $C_c = 2$ mm, $E = 200$ keV and $t = 1$ μm). Under these conditions, $d_{TEM,water}$ is estimated to be 3 nm which is larger than in the case of conventional TEM, therefore providing a reduced spatial resolution in the liquid cell. On the other hand, in scanning transmission mode, the spatial resolution is limited by the beam broadening in the presence of thick specimen [116]. Probe broadening occurs due to elastic scattering which increases the probe diameter as the beam passes through the sample, resulting in reduction of the spatial resolution [118,119].

The liquid thickness is one of the most critical parameters that influence the (S)TEM analyses. As the liquid-cell is inserted in the column of the microscope, it is subjected to the pressure difference between high vacuum (outside) and almost ambient pressure (inside the cell). Thus, the low-stress SiN_x membranes that seal the liquid may bulge under this pressure difference [120]. If the liquid completely fills the cell, the actual liquid thickness due to bulging of the membranes is thicker than the gap defined by the spacer. The liquid thickness can be reduced by forming a thin wetting liquid layer with the presence of gas or vapor on top of the liquid in the liquid-cell [121–123]. The liquid may be present only as a thin wetting layer on the interior surfaces of the liquid cell. In this case, the imaging resolution and contrast can be improved remarkably. Zhu *et al.* reported sub-nanometer resolution TEM imaging of Pd nanoparticles confined in a thin-liquid layer. The gas bubble was generated by radiolysis under electron beam irradiation [122]. Additionally, it has been reported that gas can be generated by electrolyzing the aqueous solution by applying external electric potential to achieve thin wetted liquid condition [123]. In addition to thin wetting liquid condition, researchers have demonstrated the use of graphene or 2D MoS_2 to seal liquid in TEM [124,125] and atomically-

resolved TEM images have been reported using graphene liquid-cell [124]. However, in these cases, electrochemical experiments cannot be performed due to lack of electrodes.

3.3.3 Energy-filtered TEM for LP-TEM

The effect of inelastic scattering plays a critical role for observations in liquid-phase TEM. Not only the spatial resolution becomes worse, as mentioned above, but the image contrast is also affected. The severe inelastic scattering produces a structureless background which can reduce TEM image contrast. One possibility to enhance the contrast in the LP-TEM is to use energy-filtering techniques. The reason why this technique can improve the TEM contrast will be discussed in next paragraph. In general, in EFTEM images are formed with electrons that have specific energies. It can be performed using two different types of energy filters: in-column or post-column. The in-column energy-filter, such as Ω -filter on JEOL TEMs, provides larger field of view than post column energy-filters during imaging and it is generally preferred. A schematic illustration of an in-column omega filter is shown in Figure 3.13a. The Ω -filter disperses the electrons off axis but brings them back onto the optic axis before entering the final projector lens. The ray path of EFTEM imaging using in-column filtering is shown in Figure 3.13b. The transmitted electrons are first dispersed by the magnetic prism. Then the electrons at specific energies within a finite energy-range (typically a few eV to tens of eV) are selected using an energy slit. Finally, the selected electrons form TEM images on the detector.

Zero-loss EFTEM selects the transmitted electrons that did not exhibit any energy-loss. It filters out inelastically scattered electrons in the TEM images so the contrast is enhanced. To better illustrate the contrast enhancement in zero-loss filtering, an example of filtered and non-filtered BF-TEM images of BSCF particles sitting on Pt thin-film electrode in liquid electrolyte is shown in Figure 3.13c,d. Compared to the unfiltered TEM image in Figure 3.13c, the zero-loss filtered TEM image in Figure 3.13d shows overall better contrast and it is more clear and less blurry. The polycrystalline structure of the Pt substrate is more visible. Additionally, a cloud feature surrounding the particle appears in zero-loss EFTEM. In fact, the cloud surrounding the particle is liquid electrolyte. Once the inelastically scattered electrons

traversing the liquid are removed by application of zero-loss EFTEM, the contrast of liquid becomes more visible.

Additionally, the spatial resolution of thick specimen can be improved by zero-loss EFTEM because the energy-slit can reduce the energy spread of the transmitted electrons in Eq. (3.13). However, the energy-slit also reduces the total number of electrons that can form TEM images. In this case, the spatial resolution may be limited by the electron dose (at dose-limited conditions) [116].

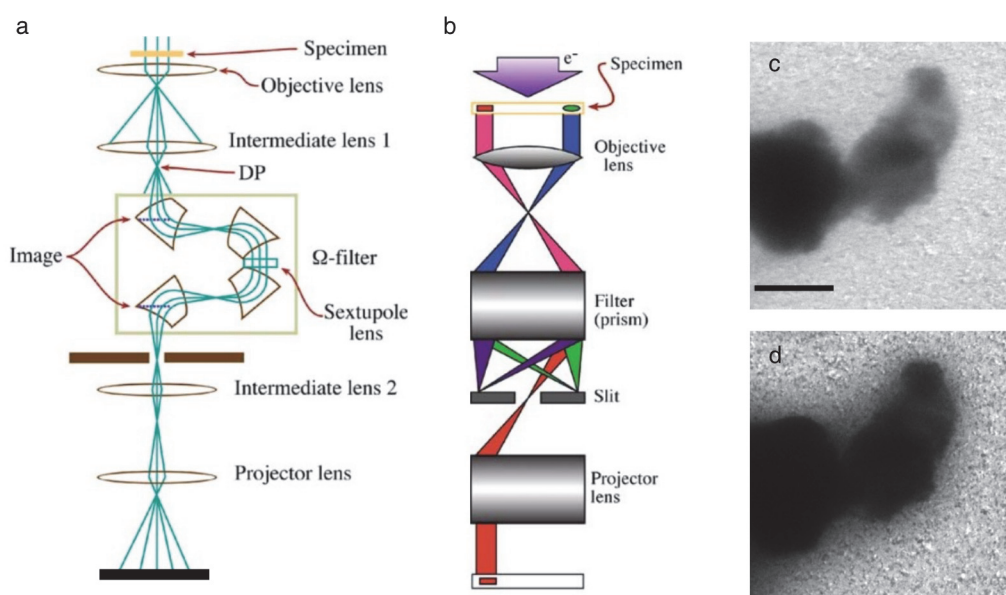
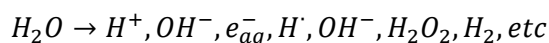


Figure 3.13. EFTEM in LP-TEM. (a) A schematic illustration of in-column omega filter. (b) A schematic illustration of ray path of EFTEM imaging. a and b are reprinted from ref. [126] with permission. © 2009 Springer Nature. (c,d) Comparison of TEM images of BSCF particles on Pt electrode enclosed in SiN_x membrane liquid-cell. (b) without zero-loss EFTEM. (c) with zero-loss EFTEM. The scale bar is 400 nm.

3.3.4 Electron-beam induced effects in LP-(S)TEM

Electron-beam can induce radiolysis of the liquid. For instance, radiolysis of water leads to the production of a series of species depending on the dose rate and initial solution [127]



Some of the species have free radicals which can be strongly oxidizing or reducing and can react with other radiolysis products in the solution. In the research field of radiation chemistry, simulations of the electron-beam induced effects on the concentration of radiolysis species in aqueous solution have been performed [128]. The chemical changes depend on the initial composition of the solution. For example, radiolysis generates H^+ ions and thus makes aqueous solutions more acidic. It has been proposed that by adding scavengers, the production of undesirable radiolysis products can be mitigated [129]. In addition to the use of scavengers, a more straightforward way is to directly lower the dose of the incident electron-beam. Although lowering the electron dose cannot fully eliminate the radiolysis, it can lower the radiation dose during an imaging experiment and mitigate the effects of radiolytic products. However, reducing the dose can affect the image quality and resolution. According to the Rose criterion, an object can be reliably detected if the pixel on the detector has a signal level above the background so that the signal-to-noise ratio exceeds a value of 3 to 5 [116]. Thus, too low dose may result in poor resolution and contrast in TEM. Recent advancements in direct electron detection (DDD) systems provide a new opportunity for realizing lowering the electron dose in liquid-cell TEM. Unlike conventional CCD and CMOS that have a window on top of the sensors, electrons directly impinge on the sensors of the DDD. Thus, the direct electron detector offers higher detective quantum efficiency (DQE), meaning that it is more sensitive compared to conventional CMOS or CCD cameras. Another advantage of direct electron detection is higher temporal resolution which is beneficial for capturing the evolution of the catalysts in transient state or early stage of catalytic reactions [109].

3.3.5 Microfabrication and configuration of electrochemical chips for LP-TEM

In order to successfully perform *in situ* electrochemical experiments in TEM, it is necessary to have an optimized configuration of the electrochemical chips. Customized chips provide the opportunity to design and fabricate the chips that fit the applications needed. Options such as electrode materials with different thicknesses are important for electrochemical experiments. In general, the chips are fabricated on Si substrates and consist of an electron transparent region and three electrodes: working (WE), reference (RE), and counter (CE) electrodes. The electron transparent region is made by suspending 50 nm SiN_x membrane on

Si substrate. Three electrodes are then patterned on the chip with membrane windows. Passivation layers such as SiO_2 or SU-8 are necessary to control the active surface of the electrodes in LP-TEM. This section introduces the microfabrication process of electrochemical chips used for the experiments within this thesis.

A schematic illustration of the process flow is shown in Figure 3.14a. To begin with, 200 μm thickness Si wafer was coated with double side 50 nm thin-film SiN_x . Many rectangular openings of SiN_x were patterned and etched via reactive-ion etching from the backside. Si substrate was then etched anisotropically from the backside of the wafer by immersing the wafer in the 20% KOH wet bench. Once the Si substrate was fully etched, the SiN_x on the front side of the wafers remained and formed suspended SiN_x membranes. The next step of the process was to pattern the electrodes on the membrane wafers using photolithography. Then, the thin-film metallic electrodes were deposited by e-beam evaporation followed by a lift-off process to remove unwanted the metallic thin-film. SiO_2 passivation layers were sputtered on the wafers. Then after patterning using photolithography some part of SiO_2 layer were etched by buffer HF solution. Thus, SiO_2 passivation layer covers some parts of the electrodes so the active surface area can be localized near the membrane region. Finally, the electrochemical chips were then diced out from the wafers. The runcard of the fabrication process is attached in Appendix A.

Examples of different designs of electrochemical chips are shown in Figure 3.14b-d. Figure 3.14b shows the electrode configuration with only WE patterned on the membrane region. Typically, the surface area ratio of CE/WE should be as large as possible to avoid having the counter electrode limit the reaction. As shown in Figure 3.14a, the WE electrode also possesses finger geometry within the membrane area. This provides more possibility of dropcast catalyst particles to partially stay on the WE electrode. In this case, the particles are connected on the Pt electrode to perform electrochemistry and can be characterized without the interference of the Pt substrate electrode. Moreover, site-specific loading of catalyst particles on WE can be performed more easily on the WE with larger surface area. Smaller electrode configurations like in Figure 3.14c,d allow better wetting of the electrolyte across the three electrodes, and it allows for larger electrolyte volume to electrode surface ratio.

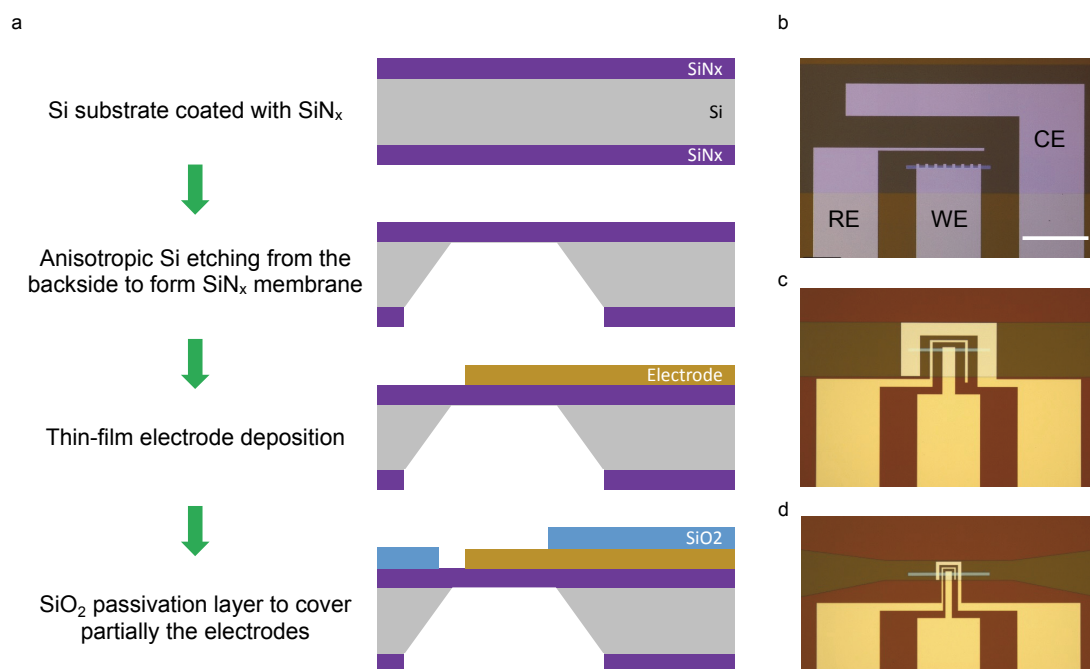


Figure 3.14. Microfabrication of electrochemical chips. (a) Microfabrication process flow of the electrochemical chips. (b-d) Different designs of electrochemical chips with three Pt thin-film electrodes. The scale bar is 500 μm.

3.3.6 Electrochemical measurements

Electrochemical measurements are typically performed using a potentiostat, which is an electronic device that can control the potential between different electrodes. Three-electrode system was used for the electrochemical measurements of this thesis. The advantage of the three-electrode cell is that a stable reference potential can be achieved. As there is very less current passing through the WE and RE, the reference potential of RE can be maintained at a stable reference potential. On the WE the electrochemical event of interest is performed. The potentiostat is used to control the applied potential of the working electrode with respect to the RE that has a well-defined and stable equilibrium potential. RE is used as a reference point against which the potential of other electrodes can be measured in an electrochemical cell. The purpose of the counter electrode is to complete the electrical circuit and the current is recorded as electron flow between the WE and CE.

It is critical to select proper working electrodes to perform electrochemical LP-TEM. As already mentioned, the electrochemical reactions are carried on MEMS chips so thin-film electrodes are used. The thickness of commercially provided thin-film electrodes is around several tenths of nanometers to ensure electrode transparency. However, to enhance image quality and to perform analytical (S)TEM in electrochemical LP-TEM, thinner electrodes are required. In the case of EELS, liquid-cell enclosures with SiN_x membranes having 15 nm Pt and 5 nm Ti adhesion layer were prepared to provide the signal-to-noise ratio of core-loss O K EEL spectra. In addition to thickness consideration, the materials of the thin-film WE should be selected according to the electrochemical reactions of interest. As the catalyst particles are dropcast on the working electrode, the substrate working electrode should be electrochemically inert. For example, for studying the hydrogen evolution reaction (HER), it is recommended to use glassy carbon and not Pt thin-film electrode since Pt is known to be a superior electrocatalyst for HER. For oxygen evolution reaction (OER), Pt thin-film electrodes can be used as a substrate working electrode as poorly conductive thin Pt oxide layer is formed at the surface under OER condition [130–132]. Additionally, Pt is more robust in an oxidative potential compared with glassy carbon thin-film electrode, hence, Pt electrodes were used herein.

Cyclic voltammetry (CV) methods sweep the potential with a certain scan rate. During CV measurements, potential cycling is applied and current response of the cell is collected. A cyclic voltammogram is formed by plotting current density against the applied potential. The current density-potential plot is also known as a polarization curve. Under these conditions, while the potential is cycling, TEM image sequences can be collected at the same time. The CV measurements can be further synchronized to the TEM image sequence so that information of the evolution with respect to the applied potential can be extracted. The procedure and codes of the synchronization used in this thesis are included in Appendix B. Other than CV, chronoamperometry (CA) can also be used to investigate the oxide catalysts under OER conditions. CA applies a constant potential and the current response is collected.

3.3.7 Potential calibration of Pt quasi-reference electrode for electrochemical LP-TEM

The reference electrode in an electrochemical cell should be placed close to the working electrode to minimize the uncompensated resistance R_u which depends on the conductivity of the solution and the distance between working and reference electrodes. During electrochemical measurements, the potential which the instrument records may not be the potential experienced by the WE electrode due to R_u . This phenomenon is called ohmic drop. Thus, iR_u compensation needs to be corrected in an electrochemical cell. The R_u can be measured by electrochemical impedance spectroscopy (EIS). Typically, the EIS measurement uses AC response. The measurement is displayed as Nyquist plot in which the imaginary part of the impedance is plotted against the real part for the range of frequencies applied. The R_u is the impedance when the frequency tends to infinity. In the MEMS chip configuration, the thin-film Pt RE is relatively close to WE. The distance between RE and WE is around several hundred micrometers. R_u in the microvolume liquid-cell is around several tenths to several hundreds of ohms in 0.1 M KOH electrolyte. The current range in the micro-volume liquid-cell is normally at most several hundred nA. In this case, the iR compensation is quite small and can be neglected in the micro-volume liquid-cell.

As the quasi-reference Pt thin-film electrodes are used in the liquid-cell, it is important to calibrate the reference potential value. For the electrocatalysis application, the applied potential is normally referred to as the reversible hydrogen electrode (RHE). It is considered as a subtype of the standard hydrogen electrode (SHE), which is based on the hydrogen redox half reaction:



The standard reduction potential of hydrogen half-cell at pH=0 is defined to be 0 V vs. SHE. Therefore, if SHE is used as a reference electrode, the applied potential is referred to as reduction potential of SHE (E_{SHE}). To convert the applied potential that is referred to RHE, the pH of the electrolyte on the basis of Nernst equation needs to be considered according to the following equation:

$$E_{RHE} = E_{SHE} + 0.059 \times pH \text{ (V)} \quad (3.16)$$

To further calibrate the Pt quasi-reference on the MEMS chip, its equilibrium potential against an external bulk reference electrode needs to be measured. For instance, the potential difference between the Pt thin-film quasi-reference electrode and external Ag/AgCl reference electrode in pH=13 of KOH electrolyte is ~ -0.06 V. Since the equilibrium reduction potential of Ag/AgCl bulk reference electrode versus SHE is $E_{SHE} = 0.2$ V, the applied potential that is referred to RHE using Pt quasi-reference electrode in a pH 13 KOH electrolyte is converted using the following equality:

$$E_{RHE} = E_{Pt \text{ quasi}} + 0.2 - 0.06 + 0.059 \times 13 \text{ (V)} \quad (3.17)$$

Figure 3.15a shows the CV curves of Co_3O_4 particles that were dropcast on a Pt working electrode. The red curves are three CV cycles performed using external bulk Ag/AgCl reference electrode that is incorporated on the tip of a liquid-phase TEM holder (Figure 3.15b). The blue curves show the CV cycles of the same working electrode in the same cell using Pt quasi-reference electrode. In both CV measurements, the pre-peak feature of Co_3O_4 in the liquid-cell in 0.1 M KOH electrolyte shows Co III/IV pre-peak feature at 1.5 V vs. RHE, which is in agreement with the value reported in literature using a bulk electrochemical cell and a 0.1 M KOH solution [133]. It is noted that the noise in the CVs of Co_3O_4 could be due to the contact of the bulk reference electrode. Another method to calibrate the Pt quasi-reference electrode is to use an internal reference. For example, the equilibrium potential of ferrocyanide/ ferricyanide redox pair is known to be at 0.4 V vs. SHE [134]. Thus, the potential of the quasi-reference electrode can be calibrated by the known potential of the redox couple.

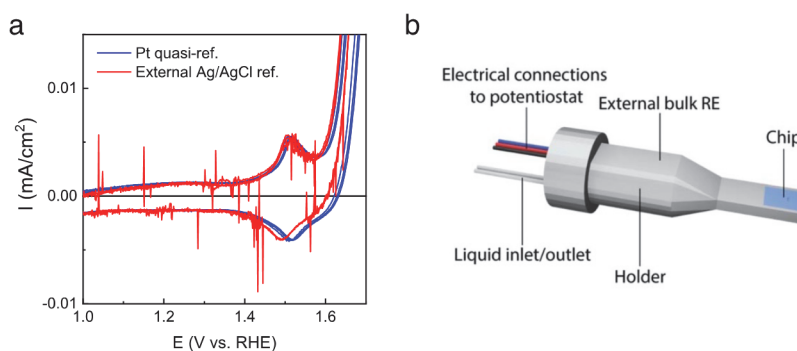
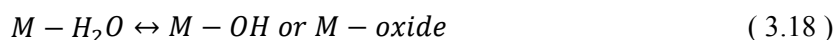


Figure 3.15. Potential calibration of Pt quasi-reference electrode. (a) CVs of Co_3O_4 using bulk Ag/AgCl (red) and Pt quasi-reference electrode (blue). (b) A schematic illustration of bulk reference electrode on the tip. Reprinted from ref. [135] with permission.

The redox pair for the noble metals as quasi-reference electrodes in an aqueous electrolyte is given by the reaction:



Thus, the stability of the Pt quasi-reference electrode in the liquid-cell depends on the equilibrium potential of the redox pair. It can be affected by the pH of the electrolyte, liquid wetting condition, adhesion layer underneath of the Pt thin-film, or the chemical species produced or consumed at the WE or CE [136].

Chapter 4 Oxygen Evolution Reaction in $\text{Ba}_{0.5}\text{Sr}_{0.5}\text{Co}_{0.8}\text{Fe}_{0.2}\text{O}_{3-\delta}$ Aided by Intrinsic Co/Fe Spinel-Like Surface

The contents of this chapter are adapted from the published article: [39]

Oxygen Evolution Reaction in $\text{Ba}_{0.5}\text{Sr}_{0.5}\text{Co}_{0.8}\text{Fe}_{0.2}\text{O}_{3-\delta}$ Aided by Intrinsic Co/Fe Spinel-Like Surface. Shen, T.-H.; Spillane, L.; Vavra, J.; Pham, T. H. M.; Peng, J.; Shao-Horn, Y.; Tileli, V. *Journal of the American Chemical Society* **2020**, 142 (37), 15876–15883. <https://doi.org/10.1021/jacs.0c06268>.

The Supporting Information referred to in the text is included in Appendix C

Contribution of T.-H. Shen: Performed the experiments, analyzed the data, and wrote the manuscript with contributions from all authors.

4.1 Introduction

Energy can be stored by splitting water into hydrogen and oxygen gas ($\text{H}_2\text{O} \rightarrow 2\text{H}_2 + \text{O}_2$). In the past decades, the development of catalysts for the anodic oxygen evolution reaction (OER, $4\text{OH}^- \rightarrow \text{O}_2 + 2\text{H}_2\text{O} + 4\text{e}^-$) in water electrolyzers has progressed remarkably [11,137–139]. Co-based oxides of various crystal structures, including perovskites and spinels, show a flexibility for tuning the electronic structure and lattice arrangement with respect to cation substitution, which renders them suitable catalysts for OER [12,23,140–142]. Among them, $\text{Ba}_{0.5}\text{Sr}_{0.5}\text{Co}_{0.8}\text{Fe}_{0.2}\text{O}_{3-\delta}$ (BSCF), a complex perovskite of the ABO_3 family, exhibits outstanding OER electrocatalytic properties in alkaline solution [12,35,36,143].

The exceptional activity of BSCF towards OER has been proposed to result from structural and chemical alteration at the surface during the reaction [35,37,38]. For example, surface amorphization and $\text{Ba}^{2+}/\text{Sr}^{2+}$ dissolution of BSCF at OER potentials was linked to increased OER currents [38]. Additionally, the change of Co ion arrangement from corner-sharing octahedra to edge-sharing octahedra, which was claimed to lead to formation of B-site oxyhydroxide (BOOH), was associated with the increasing of active sites for OER [37]. Recently, it was pointed out that a dynamic process of self-assembled $\text{CoFeO}(\text{OH})$ oxyhydroxide surface layer on BSCF during OER could be responsible for its highly active electrocatalytic properties [35]. In fact, the oxyhydroxide phase is agreed to be an active phase for OER [75,144,145], and it was reported that Co-based oxides, especially of the spinel family, are active OER catalysts due to the formation of oxyhydroxide phase when anodic potential is applied [50,89,144–146]. This active oxyhydroxide phase transformation depends on the valence and coordination of cations in the spinel structure [51,144,147,148]. On the other hand, the self-assembled B-site oxyhydroxide surface layer and A-site leaching process on BSCF was attributed to lattice oxygen evolution reaction (LOER, oxidation of lattice oxygen, $\text{ABO}_{3-\delta} + \text{OH}^- \leftrightarrow \text{BO}(\text{OH}) + \text{A}^{2+} + \text{O}_2 + 3\text{e}^-$) [35,47], triggered by OER. The authors argued that the ability to induce LOER is related to the flexibility of the perovskite structure to form oxygen vacancies. BSCF has an ability to accommodate large amount of oxygen vacancies [46], thus, it could have more flexibility for LOER.

To study the catalyst transformations undergoing electrochemical reactions, X-ray-based techniques such as XAS [35,50,148], X-ray photoelectron spectroscopy (XPS) [75], and X-

ray diffraction (XRD) [89] are widely used. These X-ray-based techniques have shown great success in understanding surfaces of catalysts, however, their lack of high spatial resolution remains a drawback that hinders direct imaging of active sites. In contrast, the electron probing transmission electron microscopy (TEM) techniques are routinely performed at nanometer spatial resolution, providing an opportunity to probe the surface of catalysts and to gain insights concerning crystal structure, composition, valence [149,150], 3d unoccupied state [151], and coordination environment [152].

Herein, complementary TEM-based imaging/diffraction and electron energy-loss spectroscopy (EELS) techniques are used to study in detail the surface structure of as-synthesized and post-OER BSCF. A mixed valence Co/Fe spinel-like surface with Co^{2+} and Fe^{3+} valence is revealed near the surface. For the experiments, a lab-on-chip setup that, unlike the convention electrochemical cell set-up, is used to ensure that the surfaces of loaded BSCF particles are directly exposed to electrolytes during electrochemical reactions. The postmortem EELS results reveal stable valence and composition of the spinel-like surface after chronoamperometric (CA) measurements. Moreover, identical location (scanning) TEM ((S)TEM) was used to track the morphological evolution of identical BSCF surface after cyclic voltammetry (CV). The pre-OER behavior as measured in CV of BSCF in a liquid-cell TEM holder suggests Co redox reactions similar to the ones of the Co_3O_4 spinel. Finally, a mechanism of reversible Co/Fe oxyhydroxide phase transformation from the Co/Fe spinel-like surface is proposed to pinpoint the role of the spinel-like surface and its effects on the OER activity of BSCF.

4.2 Experimental Section

4.2.1 Materials

$\text{Ba}_{0.5}\text{Sr}_{0.5}\text{Co}_{0.8}\text{Fe}_{0.2}\text{O}_{3-\delta}$ (BSCF) particles were synthesized using a nitrate combustion method reported previously [12,37,38,45]. X-ray diffraction of the synthesized BSCF revealed a perovskite structure (space group: $\text{Pm}\bar{3}\text{m}$) with a lattice parameter 3.99 Å [12]. CoO (Cobalt (II) oxide, 99.99% trace metals basis, Sigma-Aldrich) and LiCoO_2 (Lithium cobalt (III) oxide, 99.8%, Sigma-Aldrich) were used as standards to provide reference Co $\text{L}_{2,3}$ electron energy-

loss near edge structure (ELNES) fingerprints for the cobalt +2 and +3 oxidation states. Co_3O_4 (Cobalt (II,III) oxide, nanopowder<50 nm particle size, 99.5% trace metals basis, Sigma-Aldrich) was used for the CV comparison.

4.2.2 Lab-on-chip setup

4.2.2.1 Working electrode preparation

Customized microelectromechanical systems (MEMS)-fabricated chips patterned with a glassy carbon electrode and electron transparent SiN_x were used to deposit the catalysts and perform electrochemical measurements. The BSCF catalyst suspension was prepared by dispersing BSCF powders in isopropanol (IPA) and Nafion. This protocol was chosen to represent standard electrochemical preparation methods. To ascertain that no damage was induced on BSCF during the preparation process, two control experiments were performed. The surface of dry-deposited pristine BSCF particles was probed, which showed similar character with the surface of the particles after IPA preparation (Figure C1), and the surface properties of pristine BSCF particles directly dispersed in 0.1 M KOH were found to fully agree with the chemical character of IPA prepared and KOH immersed BSCF particles (Figure C2 and Table C1). The suspension was then dropcasted on to the electrodes on the MEMS chips and left to dry (a few minutes).

4.2.2.2 Electrochemical measurements

A potentiostat (Bio-Logic SP-300) with an ultra-low-current probe was used to perform electrochemical (EC) operations. All the EC measurements were performed in a three-electrode configuration and using 0.1 M KOH solution as an electrolyte. An immersion set-up was used to perform EC measurements for postmortem TEM analysis. A schematic of the immersion set-up is shown in Figure C3. A Pt wire was used as the counter electrode, and an Ag/AgCl (3 M NaCl, MF-2052, BASi) was used as a reference electrode. After immersion or electrochemical treatment, the chips were rinsed with deionized water (18.2 M Ω .cm, Milli-Q).

All applied potentials in this paper are reported relative to the reversible hydrogen electrode (RHE).

4.2.2.3 Identical location TEM methodology

The MEMS chip with loaded BSCF particles was initially used to characterize the BSCF particles of interest. After initial TEM analysis, the chip was subjected to electrochemical operations. The identical particles were then reanalyzed. The methodology allowed to trace the identical particles of interest within multiple rounds of electrochemical experiments.

4.2.3 (S)TEM, EDS, and EELS characterizations

The (S)TEM data acquisition was performed using a spherical aberration (Cs) corrected TEM (Titan Themis 60-300, ThermoFisher Scientific) except the part of morphological evolution using a conventional TEM (Tecnai Osiris, ThermoFisher Scientific). Both Titan Themis and Tecnai Osiris are equipped with a high brightness Schottky field emission source (XFEGTM). All experiments were performed at 200 kV or 300 kV. Energy dispersive spectroscopy (EDS) analysis was performed on BSCF particles using a Super-X windowless EDX detector fitted to the Titan Themis and Tecnai Osiris. EELS data were acquired under STEM mode on Titan Themis. Energy-loss spectra were acquired with a post column electron energy-loss spectrometer (GIF Quantum ERS, Gatan) at convergence and collection angles of 28 mrad and 19.8 mrad respectively. Energy dispersions used were 0.1 eV/ch and 0.25 eV/ch giving energy resolutions of 1.2 eV and 1.8 eV respectively. All data was acquired using the spectrum image (SI) acquisition method and DualEELSTM. The low loss energy offset was set to 0 eV in order to enable post acquisition zero-loss peak and plural scattering correction of the core-loss spectral datasets. The background of the spectra was subtracted, and plural scattering was deconvolved using the Fourier-ratio method implemented in the Gatan Microscopy SuiteTM (GMS) software.

4.2.4 *In situ* electrochemical cell

The *in situ* electrochemical experiments were performed using a liquid-electrochemistry TEM holder (Hummingbird Scientific). Customized MEMS chips (top chips) with three Pt electrodes and 1 μm spacer chips (bottom chips) were mounted on to the TEM holder to seal the micro volume liquid-cell with o-rings in between. One of three ultra-thin Pt electrode is used as a quasi-reference electrode. This Pt quasi-reference electrode was calibrated as 0.165 ± 0.04 V vs. SHE by measuring the potential against an external alkaline reference electrode (0.1 M KOH filled, RE-61AP, BASi) in 0.1 M KOH solution. The ultra-thin Pt electrode with larger surface area on the MEMS chips was used as a counter electrode. Both top and bottom chips were air-plasma treated for 2 minutes to functionalize the surfaces. The BSCF suspension were taken with a capillary (1 mm OD/0.6 mm, ID/ 90 mm length, Digitimer Ltd) pulled by a micropipette puller (Narishige PC-10, Tokyo, Japan) and then dropcasted on the working electrode using a micromanipulator (Narishige MMO-4 hydraulic micromanipulator). After the oxide suspensions were dropcasted on the top chip, 0.1 M KOH was injected into the liquid-cell through the flow tubes (360 μm OD) to perform cyclic voltammetry.

4.2.5 Electrochemical measurements in conventional bulk cell

CV measurements were performed with a conventional three-electrode chemical setup composed of: a disk glassy carbon electrode of 3 mm diameter as working electrode, a platinum wire as a counter electrode and an alkaline reference electrode (0.1 M KOH filled, RE-61AP, BASi). The catalyst suspension was prepared by dispersing Co_3O_4 powder and carbon black in isopropanol and Nafion. The ink was then sonicated in an ultra-sonicator for 1h before being drop-casted onto the working electrode with a dose of 0.26 mg/cm^2 . A rotating disk electrode (RDE, Pine Instrument Company) was used at a rotating speed of 1600 rounds per minute to remove thoroughly the bubbles formed at the electrode surface.

4.3 Results and Discussion

4.3.1 Structural and chemical analysis of BSCF surfaces

First, the surface structure of pristine BSCF particles was investigated. The dropcasted BSCF particles are surrounded by secondary phases, as shown by the high-angle annular dark-field scanning TEM (HAADF-STEM) image in Figure 4.1a. The identical particle was then immersed in 0.1 M KOH solution for 3 hours to remove soluble Ba/Sr rich secondary phases, Figure 4.1b. Energy dispersive spectroscopy (EDS) elemental maps of Ba, Sr, Co, and Fe (Figure C4) of the BSCF particle corroborate Ba/Sr rich composition of the surrounded secondary phases. The corresponding secondary phases are indicated with white arrows in Figure 4.1a. These phases might be attributed to reactions between BSCF and CO_2 and H_2O at ambient conditions [153]. A close-up HAADF-STEM image of the BSCF surface after KOH immersion in Figure 4.1c reveals a 20 nm thick shell structure (change in contrast). Moreover, statistical analysis of STEM-EDS quantification maps of surface and bulk from several particles confirms the Co/Fe-rich composition of this shell, Figure C5. In practice, the near surface demonstrates a gradual transition which takes place over several tenths of nanometers as shown in Figure C6a.

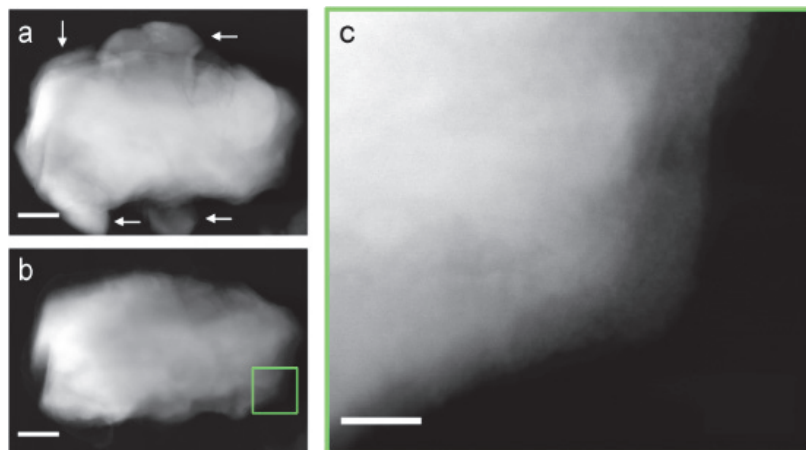


Figure 4.1. Identical location TEM study on surface structure of BSCF. (a) HAADF-STEM image of a pristine BSCF particle. White arrows indicate some of the large Ba/Sr rich secondary particles. (b) HAADF-STEM image of the same BSCF particle after KOH immersion for 3 hours (scale bar in a,b is 100 nm). (c) Close-up HAADF-STEM image of green rectangular box in (b) (scale bar is 20 nm).

To detail the properties of this surface transition in Figure 4.2c, EELS was performed. The probed region of interest (green box in Figure C6a) is divided into four sub-regions from the surface (1) to the bulk (4) as illustrated in the ADF image of Figure 4.2a. The core-loss components of EEL datasets corresponding to each sub-region are depicted in Figure 4.2b where three main features emerge. First, the Co $L_{3,2}$ white lines in the surface-probed spectra (sub-region 1) shows a chemical shift of ~ 1.5 eV to lower energy-loss compared with bulk EELS (sub-region 4). The shift of Co $L_{3,2}$ white lines indicates a change of valence [149]. Thus, to quantitatively map the valence of Co, multiple linear least square (MLLS) fitting methods using EEL spectra of CoO (Co^{2+}) and LiCoO_2 (Co^{3+}) as standards were applied. The quality of the MLLS fitting is confirmed by the randomized distribution of the reduced χ^2 map shown in Figure C7. The MLLS fitting coefficient maps of Co^{2+} and Co^{3+} in Figure 4.2a reveal that Co ions at the BSCF surface sit at +2 oxidation state whereas the expected +3 is probed in the bulk. Second, the gradual suppression of the Co $L_3/\text{Ba } M_5$ peak ratio and increasing of the Fe L_3 intensity near the BSCF surface further confirm the Co/Fe rich surface shell revealed by STEM-EDS analysis. Last, the surface O K ELNES is significantly different from the bulk. The change in the fine structure of the O K ELNES is related to the perovskite-to-spinel transition [154] at the BSCF surface. O K ELNES from the bulk sub-region 4 shows perovskite characteristics with a flat broad O K peak near 540 eV while sub-regions 1, 2, and 3 have a sharp peak near 540 eV which corresponds to the O K ELNES of spinel structure at the surface. In short, the chemical profile of the BSCF surface suggests the presence of a Co/Fe spinel-like phase.

Insights on the local chemical environment can also be attained by close inspection of the O K pre-peak (asterisk at ~ 532 eV) in Figure 4.2b. This feature is associated with the transition of the oxygen 1s to unoccupied 2p states hybridized with unoccupied metal 3d states in transition metal (TM) oxides [43,151], which provides information on the oxidation state and coordination of the TM sites surrounding the excited oxygen atom [155,156]. The reduction of the O K pre-peak intensity in sub-region 1 of the EEL spectra indicates greater content of the +2 valence of cobalt at the surface, consistent with the MLLS fitting results in Figure 4.2a. This observation can be interpreted by a decrease of unoccupied Co 3d states hybridized to O 2p [151]. The reduced oxidation state of Co has been previously found to be a consequence of the formation of oxygen vacancies for charge compensation [35,46,149,155]. However, the

underlying Co/Fe spinel structure plays the role of host structure to preserve Co^{2+} valence at the surface, irrespective of the oxygen vacancy formation since the spinel structure consists of mix valences: +2 in the tetrahedral sites (T_d) and +3 in the octahedral sites (O_h) with 1:2 ratio, for example $[\text{Co}^{2+}_{(T_d)}]_1 [\text{Co}^{3+}_{(O_h)}]_2$ in Co_3O_4 . In fact, the reduction of O K pre-peak intensity at the surface is an indication of cation deficient spinel structure or reduced TM-O bonding covalency. Both factors can contribute to a decrease of unoccupied 3d density of states, resulting in a weaker O K pre-peak [156]. On the other hand, the Fe $L_{3,2}$ edge suggests that iron remains in the +3 oxidation state over the entire region without exhibiting a chemical shift (in comparison to Fe^{3+} EELS standard, Figure C8). Thus far, the distribution of cations (Co^{2+} , Co^{3+} , and Fe^{3+}) occupied in either T_d or O_h sites remains unclear. However, it is assumed that when the structure changes from perovskite to spinel, the cobalt ions occupy the T_d sites with +2 oxidation state, that is, Co^{2+} is mainly T_d at the outermost surface while Fe^{3+} ions occupy O_h sites. This observation is supported by a recent report that Fe^{3+} is prone to occupy O_h site in Fe doped Co_3O_4 as the formation energy is lower based on DFT calculations [157]. It has also been reported that $\text{Fe}^{3+}_{(O_h)}$ confines Co^{2+} to the T_d site at the Co/Fe spinel, resulting in high activity for OER [147].

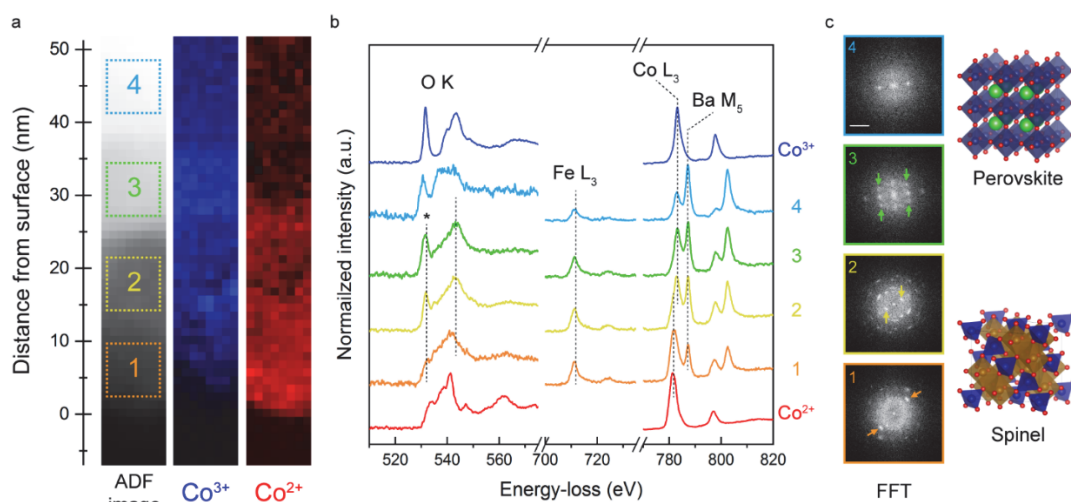


Figure 4.2. EELS and electron diffraction analysis of BSCF surface. (a) ADF image close to BSCF surface and the corresponding MLLS fitting maps of Co^{2+} and Co^{3+} . (b) O K, Fe $L_{3,2}$, Co $L_{3,2}$, and Ba $M_{5,4}$ edges EEL spectra with respect to the 4 sub-regions of interest in (a). CoO (Co^{2+}) and LiCoO_2 (Co^{3+}) reference EEL spectra for MLLS fitting are also included. (c) Selected area FFT patterns with respect to 4 sub-regions indicated on the ADF image. The green, yellow, and orange arrows indicate the reflections {113}, {111}, and {400} of Co/Fe spinel structure respectively (scale bar is 5 nm^{-1}).

To further confirm the spinel-like surface, structural analysis of the same particle in Figure 4.2c was performed by matching the reflections in the selected area fast Fourier transform (FFT) of TEM images (Figure C6b). The four sub-regions and their corresponding FFT patterns are shown in Figure 4.2c. The FFT pattern from the inner bulk BSCF (sub-region 4) shows $\{101\}$ reflections indicative of the expected perovskite structure with a lattice constant of 3.99 Å [12]. Moving towards the surface, additional reflections start to emerge. The d-spacings of non-perovskite reflections correspond to crystal planes of $(\text{Co, Fe})_3\text{O}_4$ spinel structure, with a unit cell constant of ~ 8.35 Å. For example, the d-spacings of the reflection spots indicated by green, yellow, and orange arrows are matched with spinel reflections $\{113\}$, $\{111\}$, and $\{400\}$, respectively. Further analysis demonstrating the spinel characteristic at the surface can also be found in Figure 4.3 and the d-spacing reflections of perovskite and spinel are included in Table C2. The FFT patterns of Co/Fe spinel and BSCF in Figure 4.3 infer the orientation relationship $(001)_{\text{Co/Fe spinel}} // (001)_{\text{BSCF}}$ as both FFTs match reflections viewing from the $[001]$ zone axis. The FFT pattern of perovskite region shows (100) reflection which is forbidden for spinel structure. Regarding the interface structure between spinel and perovskite, it is unclear how the strain is accommodated or whether defects are formed at the interface. In a particle-based morphology, it is challenging to obtain a well-defined interface to fully analyze the transition. However, it is expected that the spinel-perovskite interface is gradual. The spinel occurs more like a phase transformation on the BSCF surface, which may lead to the gradual transition, due to A-site deficiency/dissolution during the synthesis process or exposure to ambient air. Our EEL spectra also reveal the gradual transition as shown in Figure 4.2. On the other hand, the TEM image and the corresponding EDS Co map in Figure C9 also indicate that the Co/Fe spinel does not form a continuous layer on the BSCF surface. The spinel structure is partly covering the surface with exposed perovskite structure in places.

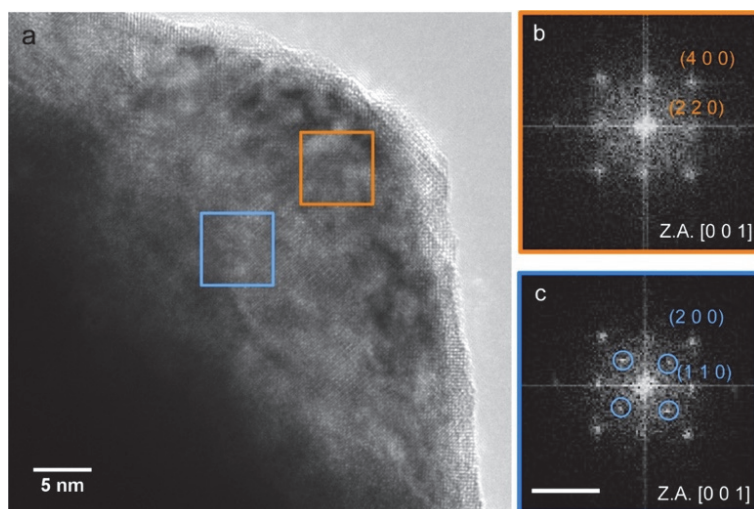


Figure 4.3. Spinel structure at BSCF surface. (a) High resolution TEM image of BSCF surface. Light-blue square and orange square indicate the perovskite and spinel regions, respectively. The zone axis is [001]. (b) Selected area FFT pattern of orange square region showing reflections from spinel structure. (c) Selected area FFT pattern of blue square region showing perovskite reflections. The blue circles indicate the {100} perovskite reflections. The scale bar is 5 nm⁻¹.

4.3.2 Electrochemical evaluation of Co/Fe spinel surface

The revealed spinel-like surface poses questions on its evolution and the role it plays during OER. To better understand the mechanism of this unique surface to the improved OER activity of BSCF, a series of local postmortem analysis using benchtop and identical location electrochemical experiments were performed.

4.3.2.1 Chemical stability after CA

First, the BSCF surface by postmortem EELS analysis (Figure C10a,b) after CA measurements in 0.1 M KOH was investigated. Figure 4.4a shows the EELS peak positions of Co L₃ edge for both bulk and surface with respect to applied potential. The superimposed black line is the current-potential plot of BSCF under anodic potentials. The Co L₃ peak positions do not demonstrate a shift after the potential was applied in the OER regime, indicating a stable Co oxidation state both in bulk and surface. Additionally, a long-term, ageing conditions were applied by holding the potential at 1.7 V vs. RHE for 3 hours. The position of the Co L₃ edge for both bulk and surface remains identical to the ones taken immediately after KOH

immersion indicating that the surface Co oxidation state is +2 and the bulk is +3, as illustrated in Figure 4.4b (the corresponding EEL spectra are shown in Figure C10c,d). As a possible OER mechanism, it has been reported that LOER [35] can take place at BSCF perovskite surface. This would lead to an irreversible change of the valence of Co after OER. In contrast, the results suggest that a reversible change of Co oxidation state might occur at the surface, meaning that Co^{2+} transforms to Co^{3+} at the surface when the applied potential exceeds the $\text{Co}^{2+}/\text{Co}^{3+}$ redox potential, and Co^{3+} reduces reversibly to Co^{2+} when the potential is removed. Thus, Co/Fe spinel-like surface is likely responsible for this reversible change of Co oxidation state since structurally reversible evolution of spinel Co_3O_4 during OER has been reported previously [50]. It is also noted that the chemical stability of the Fe $L_{3,2}$ peak position in the EEL spectra before and after OER conditions (Figure C10) indicate that Fe remains at +3 both at the surface and in the bulk.

Furthermore, the intensity ratio of Co L_3 /Ba M_5 absorption edges in surface EEL spectra that were acquired after CA measurements are similar to the ratio of Co L_3 /Ba M_5 in the surface spectra acquired after KOH immersion only (Figure 4.4c and the corresponding EEL spectra in Figure C10). That is, the Co/Fe-rich surface is maintained after oxidative potentials are applied. Previous studies showed that the A-site cation leaching process at BSCF surface resulted from OER during cycling or holding potential [35,37,38]. Our local probing suggests that the Co/Fe-rich spinel structure is formed prior to the OER onset or during synthesis, as indicated previously [158,159].

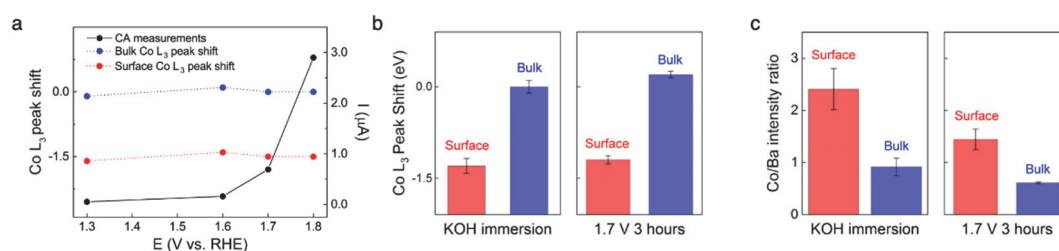


Figure 4.4. Postmortem studies of BSCF bulk (blue) and surface (red) after CA measurements. (a) Current-potential plot of BSCF (black) and Co L_3 peak position after 1.3, 1.6, 1.7, and 1.8 V vs. RHE. Each potential was held for 1 minute. (b) Shift of Co L_3 peak position and (c) Co L_3 /Ba M_5 intensity ratio of bulk and surface after KOH immersion for 3 hours compared to the CA measurements at 1.7 V vs. RHE for 3 hours. The values in (b) and (c) are averaged from three EELS datasets and the error bars represent a standard deviation.

4.3.2.2 Morphological evolution after CV

Although the postmodern EELS analysis after CA shows the reversibility and stability of the Co/Fe spinel-like surface, imaging of a single particle before and after cyclic voltammetry (CV) measurements reveal morphological changes, Figure 4.5. The overall shape of a BSCF particle remains unchanged during the entire potential cycling process, however, from the TEM images in Figure 4.5a it is evident that a rougher surface morphology arises after cycling. The close-up HAADF-STEM images in Figure 4.5b depict the tendency of the BSCF surface to adopt a porous surface, whose porosity increases as the number of cycles increases. Based on XAS studies, it has been hypothesized that BSCF can develop porosity after CV experiments [37]. However, the possibility that the degradation is an effect of electron beam induced irradiation cannot be excluded. Still, the potential cycling seems to weaken the Co/Fe spinel-like surface, which then makes it more sensitive to electron-beam after each CV measurements.

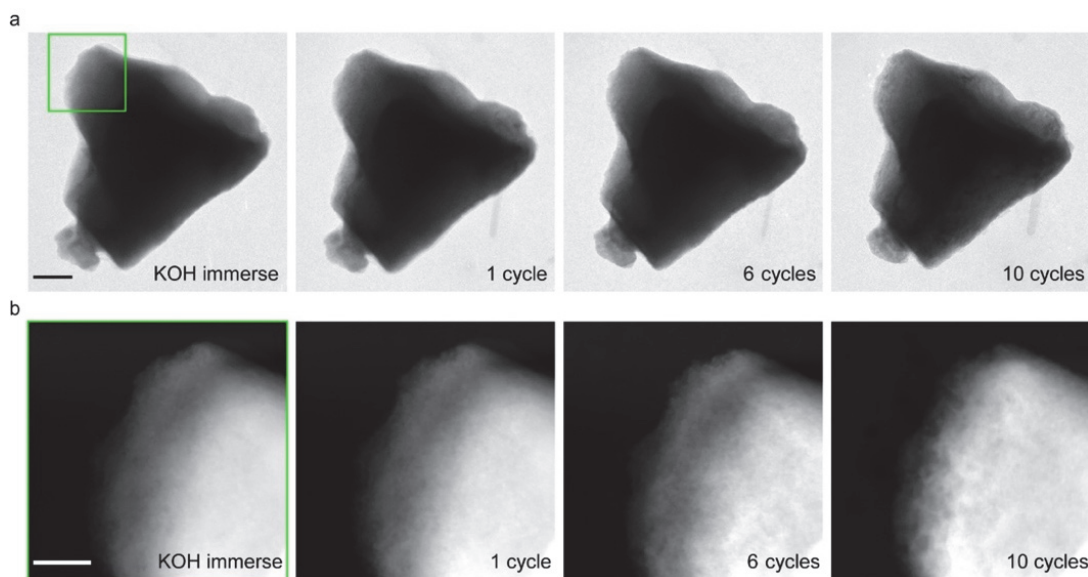


Figure 4.5. Morphological evolution of an identical BSCF particle after cyclic voltammetry. The potential range is 1.1 V – 1.8 V vs. RHE and the scan rate is 10 mV/s (a) TEM images of the full BSCF particle (scale bar is 100 nm) after CV. (b) Close-up HAADF-STEM images of green rectangular box in (a) (scale bar is 50 nm).

4.3.3 *In situ* electrochemical behavior of BSCF

To support the effect that the presence of the Co/Fe rich surface phase will entail on the active OER sites of BSCF, *in situ* electrochemical measurements were performed in a liquid-cell TEM holder. Using the micro-cell to cycle the BSCF particles enable us to fully control the loading and acquire polarization curves that are dominated by surface effects. Figure 4.6a depicts the seventh CV cycle of the bare Pt current collector and the CV curve of the BSCF loaded working electrode. A pre-peak feature is discerned around 1.3 V vs. RHE in BSCF while no pre-peak is visible in the CV of the Pt electrode. The 4th to 10th cycle of the measurements are shown in Figure C11, and the calculated potential values of the pre-peak positions in each cycle are depicted in Table C3. The pre-peak feature near this range has been correlated to the redox potential of $\text{Co}^{2+}/\text{Co}^{3+}$ in Co_3O_4 spinel [160]. Thus, to link the CV characteristics of the two systems, the polarization curve of Co_3O_4 was acquired using the bulk, rotational disk electrode setup because it provides exact measurements of Co redox potentials (Figure 4.6b). Two characteristic pre-peaks are evident. The first pre-peak wave of Co_3O_4 is at 1.1 V vs. RHE which signifies the +2 to +3 transition of Co ions [161,162]. It has been reported that the $\text{Co}^{2+}/\text{Co}^{3+}$ redox at ~ 1.1 V vs. RHE is related to formation of surface hydroxide ($\text{Co}^{2+}-\text{H}_2\text{O}+\text{OH}^- \rightarrow \text{Co}^{3+}-\text{OH}_{\text{ad}}+\text{H}_2\text{O}+\text{e}^-$) for Co-based oxide surfaces [145,162]. It is believed that the pre-peak in BSCF is also associated with this transition but it exhibits an anodic shift. Based on previous studies of Co-based oxides, the anodic shift of Co redox peak is a consequence of Fe incorporation in the structure [51,145], which again confirms the Co/Fe rich BSCF surface. This anodic shift may be also due to pH variation in the *in situ* electrochemical cell, as reported previously [162]. The second pre-peak at around 1.5 V versus RHE in the CV of Co_3O_4 is a fingerprint of the Co^{3+} to Co^{4+} transition, which is also likely to have shifted anodically and merged into the OER current regime in the CV of BSCF.

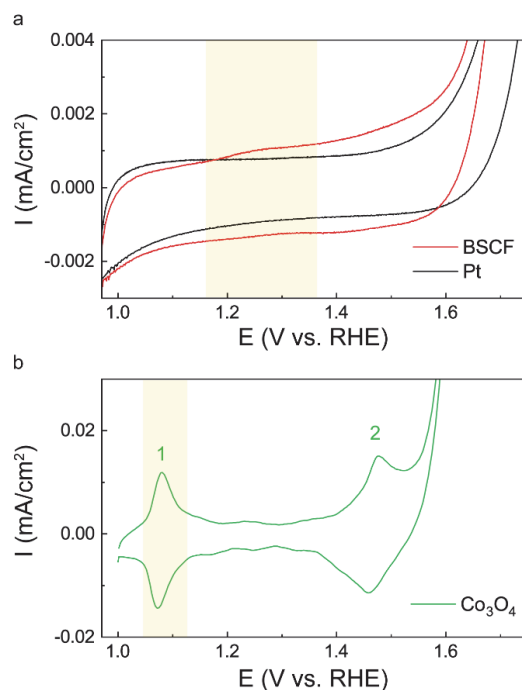


Figure 4.6. CV measurements of BSCF, Pt, and Co₃O₄. (a) *In situ* CV measurements of BSCF and Pt in a micro-volume electrochemical cell. (b) CV measurements of Co₃O₄ using rotational disk electrode set up in a bulk electrochemical cell. The colored regions indicate Co²⁺/Co³⁺ redox reaction. Both scan rate is 10 mV/s.

4.4 Mechanism

Based on insights gained by local probing of the BSCF surfaces prior and following OER, a reversible surface reconstruction of oxyhydroxide formation occurring at the Co/Fe spinel-like surface is proposed. The proposed mechanism is supported by the reversible oxyhydroxide phase transformation in Co₃O₄ spinel ($\text{Co}_3\text{O}_4 + \text{OH}^- + \text{H}_2\text{O} \leftrightarrow 3\text{CoOOH} + \text{e}^-$) [50,89], and this phase transformation is linked to the Co redox couple Co²⁺/Co³⁺ occupied in tetrahedral coordination in Co₃O₄ [51]. When the applied potential is higher than Co²⁺/Co³⁺ redox potential, Co²⁺ in Co/Fe spinel-like surface oxidizes into Co³⁺ accompanied by formation of Co/Fe oxyhydroxide. A schematic illustration of the mechanism is shown in Figure 4.7. The proposed mechanism explains the chemical stability revealed by the postmortem TEM studies, and it is believed that this reversible surface reconstruction during OER cycling results in the weakening of the Co/Fe surface lattice, which is manifested by porous-like structure. Most importantly, the formation of Co/Fe oxyhydroxide [144] can explain the excellent OER

activity of BSCF due to the active Co/Fe oxyhydroxide phase for OER [75,144,145]. We believe that the underlying perovskite structure is likely not directly involved in the oxyhydroxide formation. The robust BSCF perovskite structure underneath the Co/Fe spinel surface likely enhances the electron transport (low bandgap oxide) [163] and thus, augments the impact of the Co(Fe)OOH active phase on the overall OER activity.

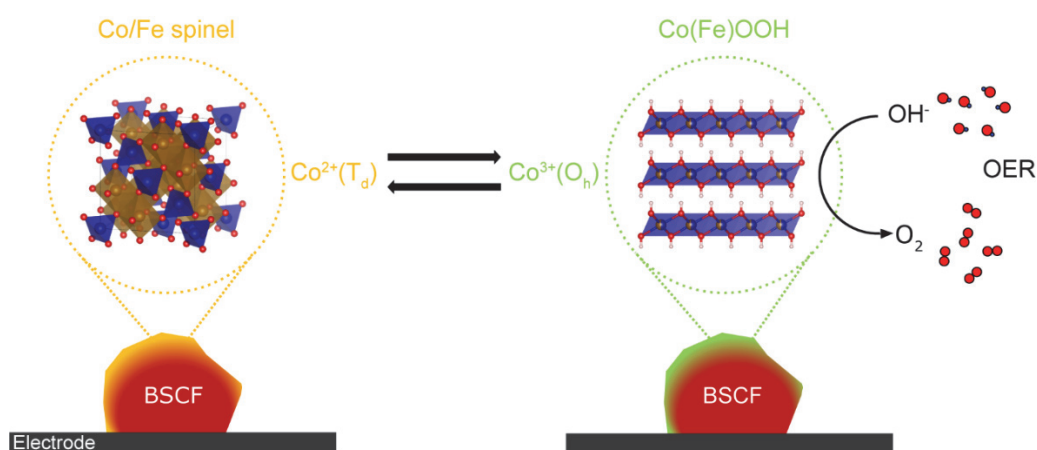


Figure 4.7. Proposed model of surface reconstruction of formation of Co/Fe oxyhydroxide at the spinel-like surface of BSCF during OER cycling.

4.5 Conclusions

BSCF is typically compared to other members of the perovskite family of catalysts in which it significantly overtakes all other oxides in catalytic performance. To date, the OER descriptors proposed for the perovskite group as a whole have also been used to discuss the high activity of BSCF in correlation with its oxygen vacant lattice. Herein, it is shown that the remarkable OER activity of BSCF is associated with an intrinsic Co/Fe spinel-like surface. Upon immersion in alkaline solution and dissolution of secondary, water-soluble phases, the underlying $\text{Co}^{2+}/\text{Fe}^{3+}$ spinel-like surface is unveiled. Postmortem EELS characterization of the surface spinel after CA showed that the oxidation state $\text{Co}^{2+}/\text{Fe}^{3+}$ remains unaffected, although a weak and electron-beam sensitive surface is revealed after CV. The discovery of this chemically stable but weak Co/Fe surface after OER explained via a reversible Co/Fe oxyhydroxide surface reconstruction mechanism occurring on this spinel-like surface. Thus,

this work exemplifies the crucial role that surface-sensitive and electrochemical micro-cell TEM techniques can play in detailing the active sites of catalysts and can provide a new characterization framework aiding development of novel design routes for targeted catalyst preparation.

Chapter 5 Switchable Wetting of Oxygen-Evolving Oxide Catalysts

The contents of this chapter are adapted from the published article: [164]

Switchable Wetting of Oxygen-Evolving Oxide Catalysts. Shen, T.-H.; Spillane, L.; Peng, J.; Shao-Horn, Y.; Tileli, V. *Nature Catalysis* **2022**, 5(1), 30–36. <https://doi.org/10.1038/s41929-021-00723-w>

The Supporting Information referred to in the text is included in Appendix D.

Contribution of T.-H. Shen: Performed the experiments, analyzed the data, and wrote the manuscript with contributions from all authors.

5.1 Introduction

Switchable wetting properties of solid surfaces from a hydrophobic to a hydrophilic character are of great interest for stimuli-responsive smart materials. In particular, the solid–liquid interface between a functional inorganic material and a liquid is exploited in a wide range of technological applications spanning from electrochemical energy systems [48], water purification [165], tunable optical lenses [166], self-cleaning surfaces [167], and sensors [57]. With respect to metal oxides, a reversible wettability can result in structural or chemical modifications induced by a variety of stimuli including light illumination [56,168], electrical potential [60,62,66,169], and temperature [170]. Potential-induced wettability of metal oxides proceeds through electrowetting [60,61] especially for dielectric oxides such as Al_2O_3 [171] and TaO_x [172]. When the potential is applied, the charges are accumulated at the interface and are arranged in the form of a capacitor, resulting in reduction of the surface tension at the solid–liquid interface [60]. Additionally, the surface chemistry of metal oxides can electrochemically change, and therefore the wettability of metal oxides can be altered via redox reactions. For example, it has been reported that the hydrophobic Cu_2O surface reduces to hydrophilic metallic copper when a cathodic potential is applied.

In practice, the wettability of solid surfaces under an applied potential can play a critical role in energy conversion [70,71,173] and especially with respect to heterogeneous catalysis [68,69]. Hydrophobic surfaces have also been reported to promote CO_2 reduction on a copper surface [55]. Moreover, studies showed that enhancement of the hydrophilicity of NiFe hydroxide by phosphorylation [70] or plasma treatments [71] can increase the activity of the oxygen evolution reaction (OER)—the anodic, sluggish reaction in water splitting [10]. Hydrophilicity of the surfaces has been shown to promote the charge-transfer rate between the electrolyte and electrode, enhancing OER activity [71], whereas perovskite oxides with more hydrophobic surfaces have been shown to be more active for the oxygen reduction reaction (ORR) [173]. It becomes evident that a fundamental understanding of the potential-regulated wetting of catalytic particles could unlock its effect on their activity and stability.

To characterize the wetting character of catalysts, analyses in planar structures are mainly performed [70]. The most common technique involves measurement of the contact angle between a liquid droplet and a solid surface, which is related to interfacial tension [53]. During

such measurements, optical images of droplets on thin-film surfaces are taken at a fairly bulk scale (approximately several hundred micrometers) [174]. Specifically, for determining the electrowettability, electrical impedance spectroscopy (EIS) is used to acquire information about the relationship between accumulated charges and wetting under an electric potential [175]. More surface-sensitive techniques such as X-ray photoelectron spectroscopy have been used to study the relationship between wetting and surface state especially in the case of water-splitting catalysts [173]. Liquid-phase transmission electron microscopy (TEM) shows promise for exploring these effects on a single-particle level [116].

In this study operando TEM in liquids is used to probe the dynamic wetting behavior of oxygen-evolving cobalt-based oxide catalysts under potential cycling, including probing of the highly OER-active perovskite $\text{Ba}_{0.5}\text{Sr}_{0.5}\text{Co}_{0.8}\text{Fe}_{0.2}\text{O}_{3-\delta}$ (BSCF). The potential-dependent variation of the contrast, which indicates the movement of the surrounding alkaline solution in the images, is associated with the modification of the wettability at the oxide surfaces. Overall, at low potentials, the hydrophobicity of the oxides reduces when an anodic potential is applied due to electrowetting induced by OH^- accumulation at the interface. The reduction of hydrophobicity is stabilized after formation of the hydrophilic oxyhydroxide phase on BSCF and spinel Co_3O_4 at a potential of ~ 1.2 V versus the reversible hydrogen electrode (RHE), which is related to the $\text{Co}^{2+}/\text{Co}^{3+}$ redox reaction. At anodic applied potentials higher than 1.6 V versus RHE, electron energy-loss spectroscopy (EELS) confirms the evolution of O_2 that leads to a thinner liquid environment.

5.2 Experimental section

5.2.1 Materials

BSCF particles were synthesized using a nitrate combustion method reported previously [12]. X-ray diffraction of the synthesized BSCF revealed a perovskite structure (space group, $\text{Pm}\bar{3}\text{m}$) with a lattice parameter of 3.99 \AA [12]. CoO (cobalt(ii) oxide, 99.99% trace metals basis, Sigma-Aldrich) and Co_3O_4 (cobalt (II III) oxide, nanopowder $<50 \text{ nm}$ particle size, 99.5% trace metals basis, Sigma-Aldrich) were used.

5.2.2 Working electrode preparation

Customized microelectromechanical (MEMS) fabricated chips patterned with three ultrathin platinum electrodes were used to deposit the catalysts and perform the operando TEM experiments. The catalyst suspensions were prepared by dispersing cobalt-based oxide powders in isopropanol. The suspensions were then dropcast on to the electrodes on the MEMS chips and left to dry (minutes).

5.2.3 Electrochemical measurements

A potentiostat (Bio-Logic SP-300) with an ultralow-current cable was used to perform electrochemical operations. All the electrochemical measurements were performed in a three-electrode configuration. The geometric surface area of the platinum working electrode is 0.001 cm². For the operando experiments performed on the MEMS platinum chips, one of three ultrathin platinum electrodes is used as a quasi-reference electrode. This platinum quasi-reference electrode was calibrated as 0.2 ± 0.04 V versus SHE by measuring the potential against an external alkaline reference electrode (0.1 M KOH filled, RE-61AP, BASi) in 0.1 M KOH solution. The ultrathin platinum electrode with a larger surface area on the MEMS chips was used as a counter electrode.

5.2.4 Liquid-phase TEM setup

Liquid-phase TEM analysis was performed using a liquid-electrochemistry holder (Hummingbird Scientific). First, the customized platinum chips (top chips) and 1 μ m spacer chips (bottom chips) were air-plasma treated for 2 min to functionalize the surfaces. After the oxide suspensions were dropcast on the top chips, both top and bottom chips were assembled on to the TEM holder. Finally, 0.1 M KOH was injected into the liquid cell through the flow tubes.

5.2.5 Operando TEM and selected-area electron diffraction analyses

The operando TEM and selected-area electron diffraction (SAED) measurements were performed in a JEOL 2200FS TEM operated at 200 kV. Zero-loss energy-filtered techniques were performed with the in-column omega energy filter to remove inelastic scattering of the system that includes the SiN_x membranes and liquid. A 12 eV energy-selecting slit was centred on the zero-loss peak in the EELS for the operation of energy-filtered TEM imaging and SAED acquisition. For the TEM imaging, a direct electron detector (DE-16, Direct Electron) with high sensitivity and temporal resolution was used to record TEM images using StreamPix software package, while the CVs were simultaneously recorded. The frame rate of the recording was set to 20 f.p.s., and the camera binning was set 2 to give a final image size of 2,048 × 2,048 pixels. The raw TEM images are averaged each 10 frames, providing TEM image sequences with 2 f.p.s. SAED patterns during cycling were acquired on a CMOS detector (OneView, Gatan) with a frame exposure time of 0.5 s.

5.2.6 Image segmentation

The TEM images were segmented to calculate the one-dimensional cloud length. Each frame of the TEM images was divided into three classes for the particle, cloud and background using the plugin Trainable Weka Segmentation in FIJI image-processing software. The classifier was trained with a random forest algorithm. After the classifier was trained, it was applied to the TEM image sequences to classify the three regions in the images. An example of the postprocessed segmentation of the first frame is shown in Figure D1. The segmented images of three cobalt oxides are shown in Figure D2. Once the images were segmented, the targeted region, for example, the cloud, was thresholded to calculate the area. A rectangle (red in Figure D2) perpendicular to the particle surface was drawn across the particle and cloud. The length of the cloud within this rectangle was calculated.

5.2.7 EELS characterization

EELS characterization. EELS data were acquired in STEM mode. The STEM-EELS data acquisition was performed using a spherical aberration (Cs)-corrected TEM (Titan Themis 60-300, ThermoFisher Scientific) equipped with a high brightness Schottky field emission source (XFEG). All experiments were performed at 300 kV. Energy-loss spectra were acquired with a post column electron energy-loss spectrometer (GIF Quantum ERS, Gatan) at convergence and collection angles of 28 and 19.8 mrad, respectively. The energy dispersion was 0.1 eV per channel, giving an energy resolution of ~ 1.1 eV. Operando EEL spectra were acquired in spot mode using time-series and dual-EELS modes. The low loss energy offset was set to 0 eV to enable post-acquisition zero-loss peak and plural scattering correction of the core-loss spectral datasets. The background of the core-loss spectra was subtracted using Gatan Microscopy Suite software.

5.2.8 EELS quantification

A JEOL F200 CFEG (S)TEM fitted with a K3 GIF Continuum and operated at 200 kV was used to acquire EEL spectra from BSCF particles dropcast on to lacey carbon support film for elemental quantification. The probe current was 200 pA during acquisition, and the convergence angle and collection angle were 8 and 16 mrad, respectively. Spectrum image data were acquired in dual-EELS mode using a K3 electron-counting detector at spectrometer energy dispersions of 0.45 eV per channel. Low-loss and high-loss spectral acquisition times were 1 and 5 ms, respectively, giving a total dwell time of 6 ms per Spectrum Image pixel. Zero-loss peak lock was enabled. Two-dimensional array spectrum images were acquired in multiple passes, giving a total accumulated acquisition time of 30 ms per SI pixel. Line profile spectrum images were calculated from the two-dimensional array datasets, post-acquisition, to improve the signal-to-noise ratio for EELS quantification. Standards-based quantification with plural scattering correction was used to determine chemical concentration profiles for oxygen, iron, cobalt, barium and strontium. Concurrent standards were used for cobalt quantification, allowing separate concentration profiles to be determined for Co (II) and Co(III). Reference spectra for Co (II) and Co (III) were acquired from CoO and LiCoO₂ powders.

5.3 Results and discussion

5.3.1 Operando TEM observation of BSCF under potential cycling

BSCF particles were dropcast on customized electrochemical chips patterned with three platinum thin-film electrodes as shown in Figure 5.1a. The operando TEM measurements were performed on a BSCF particle (dark contrast) that sits on the platinum working electrode, ensuring the electrochemical connection of the system (Figure 5.1b). Bright-field (BF) TEM images were acquired during three cycles of cyclic voltammetry (CV) ranging from 1.0 to 1.85 V versus RHE (Figure 5.1c) using an alkaline solution of 0.1 M KOH as the electrolyte. Figure 5.1d shows representative BF-TEM images of the particle's response to the three CV cycles. Interestingly, a reversible phenomenon of a dense cloud surrounding the particles and subsequent dissolution of the cloud was observed which is coupled with the potential cycling. In particular, the cloud formation substantially diminished during the anodic scan and increased during the reverse cathodic scan. Image processing consisting of thresholding and segmentation was applied to determine the modification of the contrast from the BF-TEM images. A quantitative calculation of the cloud length that surrounds the particle plotted as a function of the applied potential is depicted in Figure 5.1e. The figure illustrates that the values of cloud length decrease and reversibly increase under potential cycling. This long-range alteration of the environment surrounding the BSCF particles is around several hundred nanometers, and hence the cloud cannot be associated with the direct imaging of the electrical double layer which is at most several nanometers [176]. Additionally, this phenomenon probed in liquid-phase TEM is inherently different from the structural oscillations of BSCF particles induced by the electron beam in water vapour, as previously reported [45]. In our case, the operando measurements were acquired at a fairly low electron beam dose ($3 \text{ e}^-/\text{\AA}^2 \text{ s}$), resulting in negligible electron beam irradiation-induced effects.

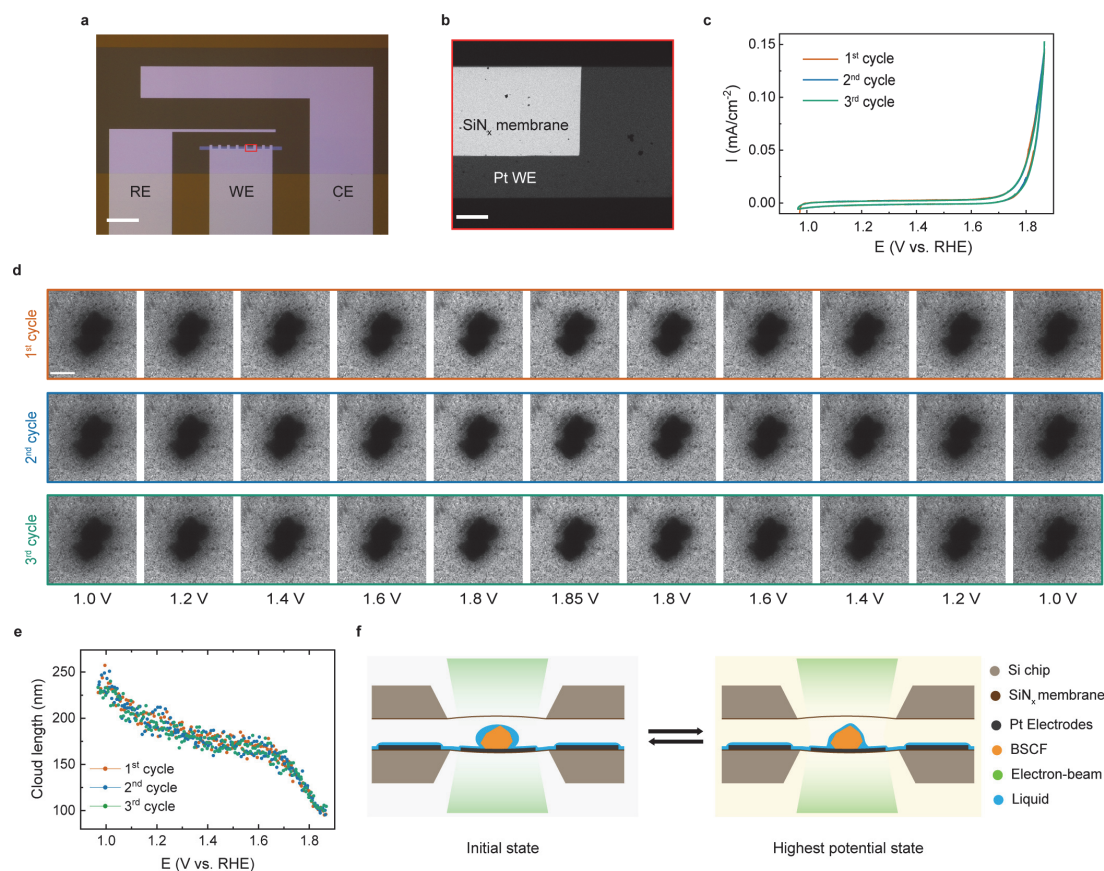


Figure 5.1. Real-time monitoring of a BSCF particle during CV measurements. (a) Optical microscopy image of a customized electrochemical chip with three platinum thin-film electrodes: RE, reference electrode; WE, working electrode; CE, counter electrode. Scale bar, 250 μm. (b) Close-up TEM image of the WE loaded with BSCF particles. Scale bar, 5 μm. (c) Polarization curves of three CV cycles in 0.1 M KOH in a liquid-cell enclosure. Scan rate, 20 mV/s. (d) TEM images at different potential stages for the first, second and third cycles. Acquisition was done at a dose rate of 3 e⁻/Å⁻² s. Scale bar, 400 nm. (e) Cloud length in each frame of the TEM images as a function of applied potential (versus RHE). (f) Schematic of reversible liquid movement surrounding BSCF particles in a liquid-cell enclosure. Shown are the initial state (1.0 V versus RHE) when the hydrophobic surface character of the BSCF surface accumulates liquid, and the final state (1.85 V versus RHE) where a more hydrophilic surface character is probed. All potential values are reported versus RHE.

It is believed that this long-range alteration is associated with the fluctuation of the liquid that wets the BSCF particles in the presence of the liquid electrolyte. The ability to produce such contrast from the liquid solution implies that the TEM liquid cell is not completely filled with the electrolyte and the particles are not fully immersed in liquid. In practice, the electrolyte forms a layer across the electrodes and the particles, as shown in the schematics of Figure 5.1f. The contrast in BF-TEM is associated with amplitude contrast. The difference in liquid

thickness generates the contrast in BF-TEM which thus indicates the dynamic movement of the liquid during cycling. It should be noted that bulging of the membranes would not lead to such locally induced amplitude contrast. When the potential sweeps to lower values, the liquid surrounding the particles becomes thicker and generates the contrast of the cloud, whereas at higher anodic potentials, the contrast around the surface of the BSCF particles disappears due to the thinner liquid that wets the surface of the particles. This pronounced potential-dependent liquid movement is attributed to the surface functionalization of the BSCF particles. That is, the wettability of the BSCF surface triggers the liquid movement and hence the amplitude contrast of the cloud surrounding the particles changes in the BF-TEM images. For all three cycles, at the initial state, the surfaces display a hydrophobic character (Figure 5.1f, left), whereas at the highest potential state the surface of the particles exhibits a hydrophilic character (Figure 5.1f, right). Remarkably, Figure 5.1 illustrates that BSCF exhibits identical reversible wetting for each cycle stimulated by the application of the potential. Furthermore, at the anodic potential of ~ 1.65 V versus RHE an abrupt release of the cloud surrounding the particles was observed. This depletion of the liquid at this potential range appears to be related to the OER take-off potential, as seen in Figure 5.1c.

5.3.2 Operando EELS analysis of molecular oxygen evolution

To corroborate that the evolution of oxygen can lead to this abrupt dissipation of the cloud surrounding the particles at ~ 1.65 V versus RHE, operando EELS in scanning TEM (STEM) mode was performed in the liquid cell during potential cycling. The evolution of molecular oxygen during the OER can be probed by monitoring the oxygen's core-loss K edge. Overall, the oxygen K edge in EELS is associated with the transition of the oxygen 1s to unoccupied 2p states. For the binary O_2 molecule, the signature peak feature in the oxygen K EEL spectra is at an energy-loss of 531 eV and it depicts the transition of oxygen $1s \rightarrow \pi^*$ [177]. To record the evolving molecular oxygen in relation to the applied potential in real time, we probed the environment in close proximity to the particle-liquid interface as shown in the schematic illustration in Figure 5.2a. The convergent electron-beam was placed next to the BSCF particle to avoid electron-beam-induced irradiation effects shown by the red dot in the annular dark-field image in Figure 5.2b. EEL spectra were continuously acquired during CV (Figure D3) to

monitor the evolution of the O_2 peak. Figure 5.2c shows the acquired oxygen K EEL spectra at 1.0 V and 1.9 V versus RHE from the first cycle. The distinct peak feature at 531 eV in the spectrum at 1.9 V indicates molecular oxygen evolution, whereas the broad peak at 540 eV appearing in all oxygen K EEL spectra is related to the background signal that comes from the KOH solution and the SiN_x membrane. To evaluate the appearance of molecular oxygen, the O_2 peak area at 531 eV is divided by the broad peak area at 540 eV. This is defined as O_2 peak intensity ratio (more information on the calculation can be found in Figure D4). The O_2 peak intensity ratio evolves periodically as a function of elapsed time, as shown in Figure 5.2d, which can be correlated with the potential during the CV measurements. This observation unambiguously confirms that the change of the cloud length at ~ 1.65 V versus RHE in Figure 5.2e is related to O_2 evolution.

At the same time, the specimen thickness (t) in units of the local inelastic mean free path (λ) varies inversely with the relative O_2 peak intensity (overlaid in Figure 5.2d). The relative thickness includes information that has to do with the SiN_x membranes, liquid and electrodes in the direction parallel to the electron beam (as sketched in Figure 5.2a). The relative thickness (t/λ) is determined by the intensity ratio of the zero-loss peak to the total EEL spectrum as shown in Figure D5. The fluctuation of the relative thickness confirms the dissolution of the cloud and indicates that the liquid becomes thinner when oxygen is being evolved. Additionally, similar operando EEL measurements were performed on Co_3O_4 as shown in Figure D6. In this case, the relative O_2 intensity also varies periodically with molecular oxygen evolving at high anodic potential. Finally, it is noted that this periodic evolution of relative O_2 intensity or relative thickness did not occur on a pure platinum working electrode (Figure D7). Interestingly, according to our operando BF-TEM image sequence in Figure 5.1d, no bubble formation is observed under potential cycling despite the evolved molecular oxygen signal being clearly detectable in the EEL spectra. This indicates that the diffusion of the evolved O_2 in the thin liquid is fast enough to avoid gas bubble formation during cycling, since gas bubble formation during gas evolving reactions is a dynamic process of the continuous local release of the supersaturation of dissolved gas near the catalyst surfaces when diffusion or convection are not fast enough [178].

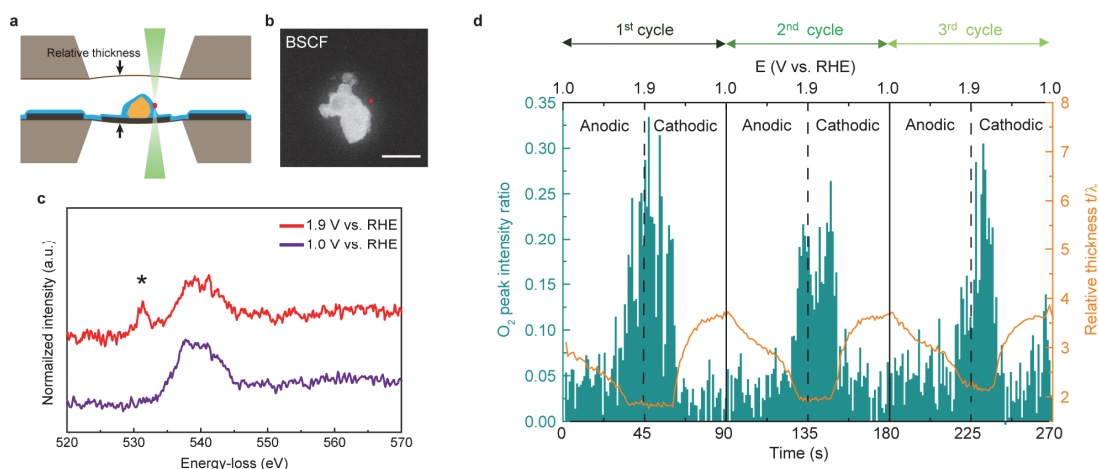


Figure 5.2. Operando EELS analysis of molecular oxygen evolution in close proximity to BSCF particles. (a) Schematic of STEM-EELS probing near BSCF particles in a liquid-cell enclosure. (b) High-angle annular dark-field STEM image of BSCF particles in a liquid-cell enclosure. The red point indicates where the electron-beam position is placed for EELS acquisition. Scale bar, 1 μm . (c) Oxygen K EEL spectrum. The asterisk at 531 eV indicates the peak feature that results from molecular oxygen evolution. (d) Plot of O₂ peak intensity ratio (green) and relative thickness (orange curve) as a function of elapsed time (bottom axis) and applied potential (top axis) corresponding to CV measurements in Figure D3. The relative thickness is defined on the basis of low-loss EEL spectra (Figure D5).

5.3.3 Switchable wetting behavior of cobalt-based oxides

To better understand the origins of the reversible wettability of BSCF, electrochemical liquid-phase TEM was performed on two other oxygen-evolving cobalt-based oxides: CoO and Co₃O₄. CoO crystallizes in the rock-salt structure with Co²⁺ ions occupying octahedral sites (O_h) while Co₃O₄ belongs to the spinel crystal structure with cobalt ions having mixed valence of +2 in the tetrahedral sites (T_d) and +3 in the octahedral sites with a ratio of 1:2. The sequence of the BF-TEM images of BSCF, Co₃O₄ and CoO under potential cycling are shown in Figure D8 and Figure D9 respectively, and their CV polarization curves are shown in Figure D10. In all three cases, a similar cloud contrast was formed around the particles at the beginning of the scan and dissolved progressively with the application of the anodic potential. To quantitatively analyze the results and compare the behavior of the different oxides, the one-dimensional cloud length of each oxide was normalized to the value of the cloud length at the launch of the synchronized imaging with the scan, at 1.0 V versus RHE. Figure 5.3a depicts the normalized cloud length as a function of applied potential of the first three cycles and reflects the changes in the wetting character during potential cycling. The plots of the first five cycles of the three

cobalt-based oxides are shown in Figure D11. Overall, the three oxides show periodic variations in the normalized cloud length with respect to the applied potential, indicating reversible wettability during cycling. The trend is similar in all cases. They show a decreasing cloud length at anodic potentials, up until the highest applied potential, before switching to increasing cloud lengths at cathodic scans. The normalized cloud length curves of BSCF and Co_3O_4 exhibit three characteristic regions at each half-cycle at low potentials ($<1.2\text{ V}$ versus RHE), intermediate potentials ($1.2\text{--}1.65\text{ V}$ versus RHE) and high potentials ($>1.65\text{ V}$ versus RHE). When the anodic potential is applied, the cloud starts to diminish, indicating a reduction in the hydrophobicity of the surfaces. At the beginning of the intermediate potential region, at $\sim 1.2\text{ V}$ versus RHE, a distinctive slope flattening occurs. The variation with respect to the applied potential is accompanied by the stabilization of the cloud surrounding the particles, indicating that the surface wetting character of BSCF and Co_3O_4 at the intermediate potential range ($1.2\text{--}1.65\text{ V}$ versus RHE) does not altered notably and the OH^- charge accumulation stabilizes. The slope change at 1.2 V versus RHE results from the surface cobalt redox reaction. In fact, the redox feature (A1/C1) is found in the polarization CV curves of both BSCF and Co_3O_4 (Figure 5.3b,c, respectively). Moreover, the CV of Co_3O_4 shows an additional cobalt redox feature A2/C2 at 1.5 V versus RHE. No notable change occurs at 1.5 V versus RHE in the Co_3O_4 normalized cloud length plot, meaning that the first surface cobalt redox reaction dominates its wetting behavior. In fact, the two redox features A1/C1 and A2/C2 are attributed to $\text{Co}^{2+}/\text{Co}^{3+}$ and $\text{Co}^{3+}/\text{Co}^{4+}$, respectively [160]. This indicates that $\text{Co}^{2+}/\text{Co}^{3+}$ plays a major role in the wettability characteristics of the cobalt-based oxide catalysts. Although $\text{Co}^{3+}/\text{Co}^{4+}$ redox peaks are more pronounced in the CVs of CoO and Co_3O_4 , this does not lead to further modification of the cobalt local oxygen-coordination shell [89]. Thus, the reaction does not have notable effect on the surface wettability. The abrupt reduction in the normalized cloud length plot of BSCF at the third region, above 1.65 V versus RHE, is linked to the evolution of O_2 . For Co_3O_4 , no pronounced reduction in the cloud surrounding the particles is seen in the third region. This could be attributed to the fact that Co_3O_4 is less OER-active than BSCF [4]. In contrast to the other two oxides, CoO varies almost linearly with respect to the applied potential, with the slope remaining constant during the first half-scans. In other words, the reduction of the hydrophobicity of CoO remains constant across the first redox feature and the accumulation of OH^- is continuous across the full potential range. This nearly constant slope could be attributed to the indistinct A1/C1 redox feature, as shown

in Figure D12, which can be related to the Co^{2+} octahedral coordination in the rock-salt crystal structure. It has been reported that the octahedrally coordinated Co site is inactive and it is not involved in the oxyhydroxide phase transformation [51]. Thus, Co^{2+} ions in octahedral sites may lead to a less pronounced $\text{Co}^{2+}/\text{Co}^{3+}$ redox feature [133]. Finally, both BSCF and Co_3O_4 exhibit relatively stable wetting behavior across the three cycles, with BSCF being particularly stable across the anodic and cathodic scans. For CoO , however, its wettability changes are not as stable as for the other two oxides as shown in Figure D11. The average slopes are getting steeper as the cycle number increases. This could be related to the previously reported irreversible CoO to Co_3O_4 transformation at the initial cycles that causes the interfacial capacitance to change [133].

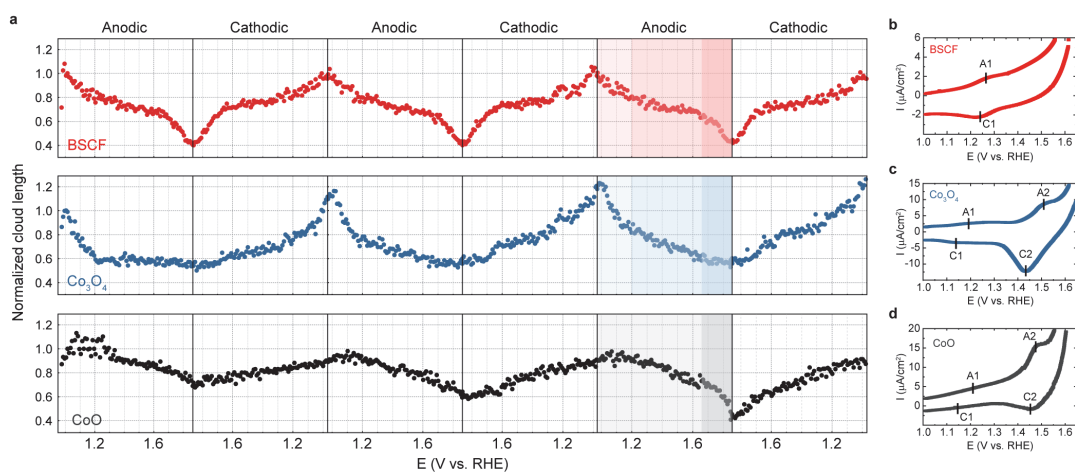


Figure 5.3. Potential-induced switchable wetting behavior of cobalt-based oxides. (a) Plot of normalized cloud length as a function of applied potential for the first three cycles. The cloud length was normalized from the values of cloud length at 1.0 V versus RHE. (b–d), Representative cyclic voltammograms of BSCF (b), Co_3O_4 (c) and CoO (d) in the potential range 1.0–1.65 V versus RHE. Scan rate, 10 mV/s. The measurements were performed in a microvolume liquid cell. A1/C1 and A2/C2 redox waves are attributed to $\text{Co}^{2+}/\text{Co}^{3+}$ and $\text{Co}^{3+}/\text{Co}^{4+}$, respectively. Cobalt-based oxides are heavily dropcast on the electrochemical chips to see redox features. The full range of polarization curves are shown in Figure D12.

5.3.4 Proposed mechanism of wetting behavior

A mechanism of switchable wetting detailed for the highly active BSCF under potential cycling is schematically illustrated in Figure 5.4. The suggested potential-dependent wetting

transition of BSCF at the low potential region <1.2 V versus RHE can be explained by the theory of electrowetting as defined by the Young–Lippmann equation:

$$\cos\theta - \cos\theta_{eq} \propto \int C(E)EdE \quad (5.1)$$

This equation relates the difference of the contact angle θ after application of the electric potential E to the contact angle at equilibrium (at 1.0 V versus RHE in our case), θ_{eq} , with the potential-dependent capacitance at the solid–liquid interface, $C(E)$. It indicates that on application of the electric potential a thin layer of OH^- ions accumulates at the interface, giving rise to interface capacitance that results in a contact angle modification. In practice, this equation implies an overall reduction of the contact angle under the applied potential, providing a qualitative explanation of the reduction of the hydrophobicity and a transition towards a hydrophilic character in BSCF at the low potential range. At 1.2 V versus RHE, the change of slope is related to the surface $\text{Co}^{2+}/\text{Co}^{3+}$ redox reaction in tetrahedral coordination [51,147]. This redox feature has been attributed to reversible oxyhydroxide (CoOOH) phase transformation, which for the Co^{2+} in spinel proceeds with the electrochemical reaction $\text{Co}_3\text{O}_4 + \text{OH}^- + \text{H}_2\text{O} \leftrightarrow 3\text{CoOOH} + \text{e}^-$ at 1.22 V versus RHE [89,133]. The detailed EELS quantification profile of all elements in BSCF (Figure 5.4) confirms the predominance of Co^{2+} ions at the surface with a characteristic increase in the Co^{2+} concentration from 0 at.% at the inner bulk to ~ 20 at.% at the surface (light blue profile). The full range of EEL spectra are shown in Figure D13. Previously it is shown that the perovskite BSCF particles possess a Co/Fe spinel surface with reduced cobalt valence which enables the Co(Fe)OOH phase transformation [39]. The spinel–perovskite double structure and its stability during cycling are confirmed by operando selected-area electron diffraction measurements (Figure D14), while the subtle changes of the $\{113\}$ spinel reflections indicate the restructuring of the spinel surface during cycling. The formation of Co(Fe)OOH at the surface modifies the adsorption of OH^- ions at the interface, leading to alteration of the interface capacitance. Additionally, taking into account the previously reported intrinsic oxyhydroxide phase hydrophilicity in nickel-based catalysts [179], it is concluded that BSCF transitions towards a hydrophilic character at 1.2 V versus RHE, which remains relatively stable until 1.65 V versus RHE. Similar electrochemically induced modification of intrinsic surface activity has also been

demonstrated on oxidation of copper surface [66] and liquid gallium [67] by application of electric potential.

At the third region, above 1.65 V versus RHE, the evolution of O₂ results in a globally thinner liquid layer. The influence of the OER on local liquid movement can be attributed to two factors. First, the increase in the volume of the gas-filled region compresses the liquid layer during the OER. As the cell is not completely filled with liquid, gas is also present in the cell. The evolved molecular O₂ from the catalytic oxide surface dissolves and diffuses through the thin liquid layer, and once the molecular oxygen reaches the gas–liquid interface, it precipitates and induces the growth of the volume in the gas-filled region. The growth of the gas region thus attenuates the thickness of the liquid. Second, the liquid electrolyte surrounding the surface of the particles is consumed during the OER, which leads to a reduced liquid layer. Both effects act synergistically and contribute to liquid movement at potentials where the OER takes place.

Further, our results help access how the liquid moves under the OER. The relative thickness that is extracted from the low-loss EEL spectra is indicative of the thickness of the cell in its entirety along the z direction (parallel to the electron beam) while the normalized cloud length provides information about the in-plane liquid movement (perpendicular to the electron beam). In the OER regime the normalized cloud length is continuously decreasing on the anodic scan, whereas the relative thickness reaches a plateau and remains unaltered (as shown in Figure D15). This means that the liquid thickness is reduced in the in-plane direction (due to the consumption of liquid surrounding the particles) while the overall thickness of the cell does not change.

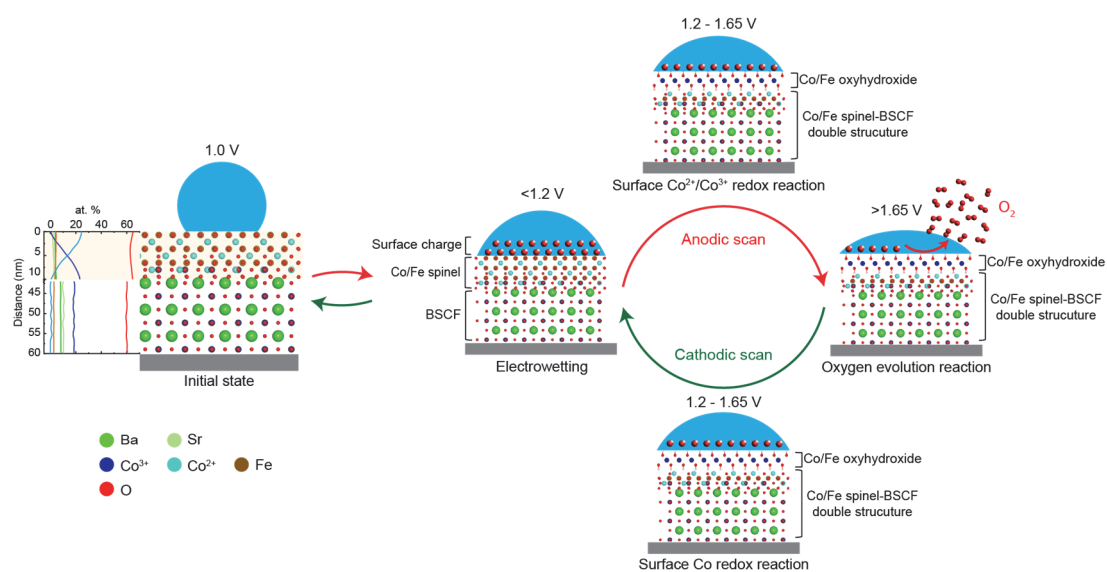


Figure 5.4. Proposed mechanism of switchable wetting at the BSCF oxide surface under potential cycling. Electrowetting induces a hydrophobic to hydrophilic transition on the initial Co/Fe spinel surface on BSCF. The EELS quantification profile of all elements in BSCF is shown next to the schematic of the initial state. Zero distance corresponds to the surface. Cobalt ions with +2 oxidation state are present at the BSCF surface while the valence of cobalt in bulk is +3 (as expected in the perovskite). The bulk atomic percentages correspond well to the stoichiometry of $\text{Ba}_{0.5}\text{Sr}_{0.5}\text{Co}_{0.8}\text{Fe}_{0.2}\text{O}_{3-\delta}$. Co/Fe oxyhydroxide forms at the Co/Fe spinel surface at 1.2 V during anodic scan, holding the hydrophilic character. The surface oxyhydroxide further catalyzes the OER at higher potential so the surrounding liquid is thinner. The process is reversible.

5.4 Conclusions

Switchable wetting behavior at oxygen-evolving catalyst surfaces has been demonstrated, specifically cobalt-based oxides, on the basis of relating the contrast seen in electrochemical liquid-phase TEM to the movement of the liquid surrounding the particles. The alteration of the surface wetting character shows three distinct regions during cycling, which are related to electrowetting and surface reconstruction mechanisms. At low applied potential (<1.2 V versus RHE), electrowetting and potential-dependent interfacial capacitance induce a hydrophobic to hydrophilic transition. The formation of an oxyhydroxide phase at the surfaces at 1.2 V versus RHE also leads to the attainment of a hydrophilic wetting character. For potentials larger than 1.65 V versus RHE, the surface oxyhydroxide further catalyzes the adsorbed hydroxide ions at the solid–liquid interface to form molecular oxygen, as verified by operando EELS measurements. Liquid-phase TEM can provide unique insights of wetting

dynamics in real time, opening a pathway to better understand the solid–liquid interface interactions. Moreover, its capability to detect the products of catalytic reactions at a single-particle level was shown.

Chapter 6 Towards EELS Quantification of O₂ in LP-TEM

In this chapter, an approach to quantifying molecular oxygen using EELS is discussed. First, the qualitative studies of molecular oxygen evolution under chronoamperometry are detailed. The next section introduces the fundamentals of EELS quantification process along with the quantification of gas components in environmental TEM (ETEM). Next, EELS quantification process in cell enclosure is described. The air-cell enclosure and nitrogen concentration with known ratio in the SiN_x membranes were first used to test the quantification process. Finally, the process is applied for the quantification of the amount of a molecular oxygen bubble generated by the application of potential in a liquid-cell enclosure.

6.1 Oxygen evolution of an IrO₂ particle

The EEL spectra of the molecular oxygen evolution depicted in Chapter 5 were acquired under spot mode as time elapsed, providing the evolution with respect to the applied potential at a single position. The drawback of the spot mode acquisition is that the spatial information is lacking. Another way to perform EELS acquisition is to use Spectrum Image (SI) under STEM mode. This acquisition method thus provides 2-dimensional information and the capability of mapping. Figure 6.1a illustrates the scanning of the electron-beam across an IrO₂ particle that is dropcast on an ultra-thin film Pt electrode in a liquid-cell enclosure with 0.1 M KOH electrolyte. A thin-film liquid wets the particle. At the same time, a constant anodic potential at 1.95 V versus RHE is applied. The current response of chronoamperometry in Figure 6.1b is stabilized at ~80 nA. During the EELS acquisition, dual-range EELS was applied. The low-

loss EELS provides the thickness map while the core-loss O K edge offers information of molecular oxygen distribution under the application of the potential. Figure 6.1c shows an ADF image of IrO₂ and its corresponding relative thickness map of the SI under chronoamperometry. The bright contrast in the ADF image indicates the IrO₂ particle. Compared to the relative thickness map, the center of the particle shows the relative thickness (t/λ) value as large as 2.5 while the t/λ is ~ 1.3 at the position close to the edge to the particle. The t/λ decreases to ~ 1 when the position moves farther from the particle. As the relative thickness reflects the overall thickness of the cell that is parallel to the electron-beam direction, the decreasing of its value indicates a gradient of liquid profile that is thicker at the edge of the particle (dark green spot in Figure 6.1c) and thinner at the position being further away from the particle (light green spot in Figure 6.1c). The O K EEL spectra of dark and light green spots are shown in Figure 6.1d. The O K EELS from the dark green spot shows a notable molecular oxygen feature at 531 eV under OER conditions.

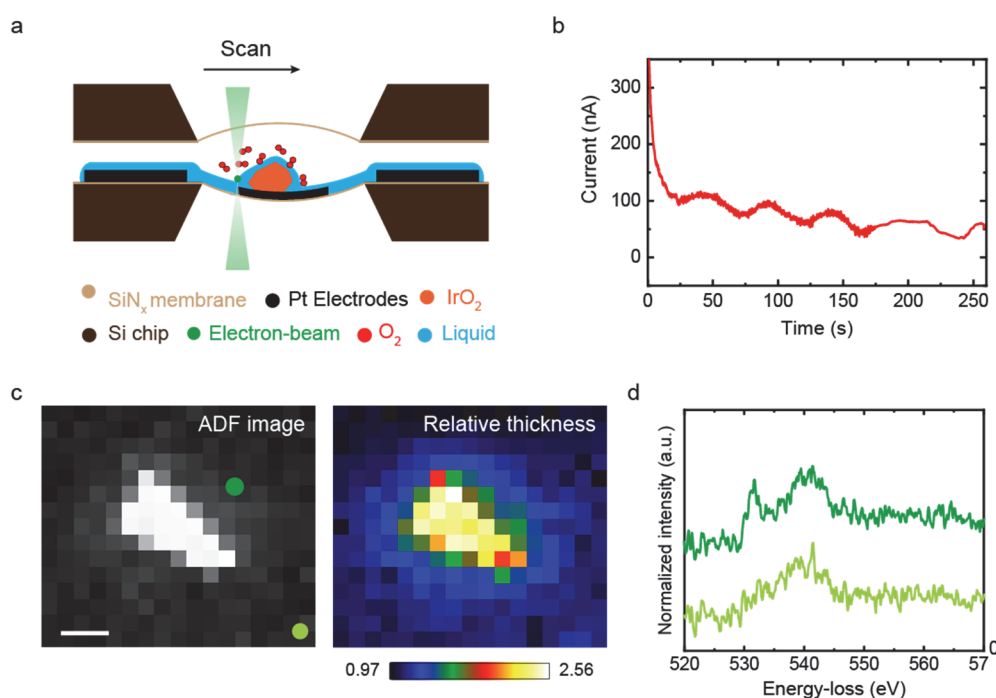


Figure 6.1. Probing molecular oxygen evolution near a single IrO₂ particle. (a) A schematic illustration of probing molecular oxygen evolution near a single IrO₂ particle using Spectrum Image. 2D scan is performed under OER condition. (b) Current response with respect to time of chronoamperometry at 1.95 V versus RHE. (c) ADF image and relative thickness map of the IrO₂ particle. Scale bar, 100 nm. (d) O K EEL spectra of dark and light green spots in the ADF image.

To further understand the molecular oxygen distribution in the Spectrum Image, multiple least linear square fitting (MLLS) was performed to separate the contribution of the components in the O K EEL spectra. The fitting coefficient of a component in MLLS fitting is qualitatively proportional to the amount of the component. Figure 6.2 shows the fitting coefficient maps of the three components at O K edge: IrO₂, molecular oxygen, and liquid electrolyte. Prior to the MLLS fitting, the Spectrum Image was denoised by principal component analysis (PCA) to have better fitting results. The fitting coefficient map of IrO₂ does not match the ADF image of IrO₂. This may be due to failure of the MLLS fitting to accurately decompose at the position of the thick IrO₂ particle. The fitting coefficient map of O₂ shows that the value is higher at the position closer to the IrO₂ particle. This could be qualitative evidence of the O₂ evolution from a single IrO₂ particle. The fitting coefficient map of the liquid electrolyte also indicates that increased amount of the liquid at the position that is closer to the edge of the particle. The map is thus consistent with the relative thickness map in Figure 6.1c. Overall, the MLLS fitting shows the capability to separate the contributions of different components in O K EEL spectra, providing qualitatively O₂ and liquid electrolyte maps.

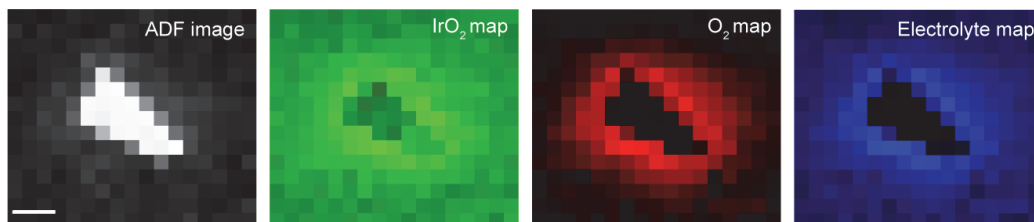


Figure 6.2. Fitting coefficient maps of IrO₂, and O₂, and electrolyte. A constant potential 1.95 V vs. RHE was applied. Scale bar, 100 nm.

6.2 EELS quantification process for the molecular oxygen

The section above and Chapter 5 demonstrated qualitatively the probing of molecular oxygen evolution using EELS under STEM mode. However, to evaluate the absolute amount of molecular oxygen in the EEL spectra, quantification is needed.

6.2.1 Fundamentals of EELS quantification

Typically, quantification of EEL spectra approximately evaluates the areal density, N , in terms of measurable quantities using the integral intensity of the ionization edge k up to a specific width Δ [92]

$$N = \frac{I_k(\beta, \Delta)}{I_t \sigma_k(\beta, \Delta)} \quad (6.1)$$

where N , I_k , I_t , σ_k , β , Δ are the areal density of atoms, integral intensity at edge k , total integrated intensity, inelastic partial scattering cross-section, collection angle, and signal integration width, respectively. The effect of plural scattering is convolved in the core-loss ionization edge intensity. Thus, the plural scattering may have an impact on the quantification especially when the specimen is thick or involves high atomic number Z elements. In Figure 6.3 the plural scattering deconvolution is shown. The convolution of the plural scattering in the core-loss ionization edge may alter the edge shape or intensity which may lead to inaccurate quantification results. In certain cases, such as low thickness of the specimen or pure gas samples, the effect of plural scattering is negligible. Otherwise, for thick samples, plural scattering should be removed prior to performing the quantification or be included during the quantification process.

The partial scattering cross-section $\sigma_k(\beta, \Delta)$ is the most important parameter to be determined during EELS quantification. The role of the partial scattering cross-section represents the scattering strength of the atoms of interest under specific conditions. It can be generally described by the energy differential cross-section $d\sigma/dE$ when the scattering angle is $\ll 1$ rad [92]

$$\frac{d\sigma}{dE} = \frac{8\pi a_0^2 R^2}{Em_0 v^2} \ln[1 + (\beta/\theta_E)^2] \frac{df_n}{dE} \quad (6.2)$$

where E is the energy-loss, R is the Ryberg constant, θ_E is the characteristic scattering angle, a_0 is the Bohr radius, v is the electron velocity, and m_0 is the electron rest mass. The df_n/dE is known as the generalized oscillator strength (GOS). It represents a transition matrix of the

initial and final states during the scattering process. Two of the most common approximations of the GOS are the hydrogenic and Hartree-Slater atomic wave functions. Once the GOS is theoretically calculated so the energy differential cross-section is determined, the partial scattering cross-section $\sigma_k(\beta, \Delta)$ can be calculated with the following equality:

$$\sigma_k(\beta, \Delta) = \int_E^{E+\Delta} \frac{d\sigma}{dE} dE \quad (6.3)$$

In practice, the quantification process in DigitalMicrograph software uses the model-based quantification [180]. It means that a model fit of integral intensity at the ionization edge is incorporated. For instance, considering an ionization edge of an element, the background is treated as a power-law (E^{-r}) while the edge is modeled by a single theoretical cross-section ($\sigma(E)$). A model fit to integral intensity at core-loss is performed during the quantification process so the intensity can be expressed by:

$$aE^{-r} + b\sigma(E) \quad (6.4)$$

Multiple linear least square (MLLS) fitting algorithm is used to determine the fitting coefficient a and b within a specific fitting energy-loss range and collection angle. The fitting procedure assumes that the effect of the plural scattering is negligible or removed. If the sample is thick and the low-loss EELS data are provided, the effect of plural scattering is handled by forward convolution of the model cross-section. Thus, the fitting coefficient b is proportional to the areal density. Relative quantification of two different elements A and B can be written as

$$\frac{N_A}{N_B} = \frac{I_A(\beta, \Delta)}{I_B(\beta, \Delta)} \frac{\sigma_B(\beta, \Delta)}{\sigma_A(\beta, \Delta)} = \frac{b_A}{b_B} \quad (6.5)$$

For absolute quantification, the coefficient of the cross-section term, b , is divided by the total spectrum intensity I_t . The result thus gives the areal density N .

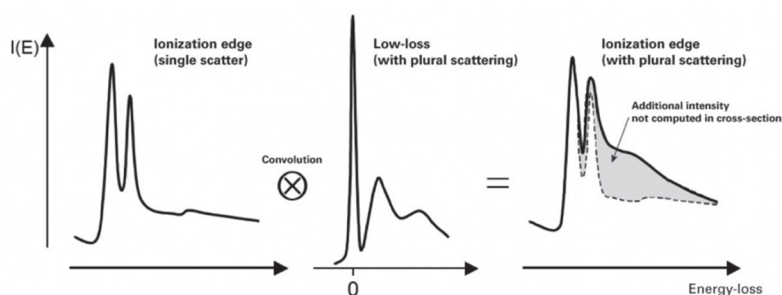


Figure 6.3. A schematic illustration of the convolution of plural scattering to the core-loss ionization edge. Reproduced from ref. [181] with permission. © 2002 Springer Nature.

6.2.2 Quantification of gas composition by EELS in environmental TEM

Environmental TEM (ETEM) ETEM has been used to demonstrate the power to study dynamic gas-solid reactions in catalytic materials [45,182]. *In situ* analysis of gas composition by EELS in ETEM has been reported [183,184]. For instance, Crozier *et al.* quantified the relative O/C ratio of CO gas in ETEM using core-loss EELS based on the concepts detailed in the previous section. Hartree-Slater cross sections in Digital Micrograph software were used and plural scattering in the core-loss EEL spectra was excluded due to the low scattering parameters ($t/\lambda < 0.2$). They reported that average O/C ratios were 0.68 ± 0.05 for CO gas showing that the values were low by 30% [184]. In their ETEM experiments, the gas cell had a large gap with the pole of ~ 5 mm and therefore the inelastic scattered electrons at the top and bottom of the cell may follow different trajectories. In this case, the fraction of the inelastic scattered electrons entering the spectrometer may be different, resulting in discrepancies in the quantification procedure. Other than core-loss EELS quantification, they also performed gas component analysis using low-loss EELS, which is particularly useful to quantify molecular hydrogen gas. Information on the component gases was available but the molar concentrations of the gas mixture were unknown. The authors used a linear combination of the individual low-loss EEL spectra of the component gases to determine the molar concentration of the mixture. They tested their procedure using air for which the O/N ratio is expected to be 0.268. The average O/N molar concentration ratio using the linear combination method was 0.28 ± 0.01 , which is within 4% of the expected value.

6.2.3 Standard-based EELS quantification

A single cross-section model may not give a reliable fitting of the ionization edge because the theoretical cross-section models do not fully reflect the electron scattering/transition processes. The theoretical models assume that atoms are isolated and spherical, meaning that the bonding and structure of the specimen in the materials are not included in these cross-section models. Further, the electron-loss near edge fine structures (ELNES) such as white lines are not included in the theoretical cross section models. Thus, the MLLS fitting can fail. In fact, multiple cross-section models are included in the fitting to improve the accuracy of the quantification so more than one cross-section models derived from known standards to perform MLLS fitting are used. The approach is particularly useful for separating closely overlapping edges. Additionally, the ELNES features from a known standard can be stored in a cross-section model and fitted in the quantification process. ENLES features at the edge onset can be described by acquiring EELS experimental standards. The EELS standards scale the experimentally measured edge shape by splicing a theoretical cross-section in the tail area to create an appropriately scaled experimental cross-section. In this way the measured EELS standards are converted into the scattering cross-section $\sigma(E)$. The standard-based quantification can be possibly used for quantifying molecular oxygen in O K EELS data. As shown in the O K in Figure 6.1d, the molecular oxygen peak feature at 531 eV is lying closely to the broad bump feature at 540 eV which is related to the oxygen in the liquid and SiN_x. Thus, by performing the fitting process using standard spectra of pure O₂ gas and liquid electrolyte the contribution in the EEL spectra can be separated.

6.3 EELS quantification in cell enclosure

It is necessary to validate the quantification workflow by performing experiments on control systems. To evaluate the quantification procedure, it was first tested on an air-cell enclosure that is sealed with two SiN_x membranes. Next, the EELS quantification was applied to a condition including liquid electrolyte and O₂ gas.

6.3.1 Air-cell enclosure

Air can be used as a standard to validate the quantification since the O₂ to N₂ ratio is well known (0.268). The air-cell enclosure is similar to the liquid-cell one. It consists of two SiN_x membranes enclosing air. The environment outside is vacuum. A schematic illustration is depicted in Figure 6.4a. The EEL spectrum of N K and O K edges of the air-cell enclosure after background removal and deconvolution of plural scattering is shown in Figure 6.4b. EEL spectra were acquired using Spectrum Image. Standard spectra of the nitrogen and oxygen K edges in SiN_x membranes were also acquired under vacuum cell conditions. N₂ and O₂ reference EEL spectra were extracted from Atlas in DigitalMicrograph software. The four EEL standard spectra that were used in the quantification are included in Figure 6.4b. Molecular nitrogen shows a strong peak feature at 401 eV which is due to the transition of 1s to π^* antibonding state. The broad peak at 410 eV is the contribution of nitrogen in SiN_x. Molecular oxygen appears as a notable sharp peak feature at 531 eV, and the broad feature at 540 eV is related to oxygen in SiN_x. Once the standard spectra were determined, they served as components for the quantification. They were first measured in DigitalMicrograph software and they were converted in units of cross-section. Then, those cross-sectional models as well as a background model were applied to fit the integral intensity at each ionization edge of EEL spectra of the air-cell. As the low-loss data were provided, plural scattering is convolved back in each cross-sectional model. For example, N K edge ionization edge intensity can be written as three components: background, nitrogen in SiN_x, and N₂ gas:

$$aE^{-r} + b\sigma(E)_{N \text{ in } SiN} + c\sigma(E)_{N_2} \quad (6.6)$$

MLLS algorithm is then applied to determine the fitting coefficients a, b, and c. The areal density of each component is the fitting coefficient divided by the total intensity and the cross-section. Further, the ratio of each component can also be determined. The quantification results are shown in Table 6.1. They indicate that the O₂/N₂ ratio is 0.247 which lies with 8% of the correct value of O₂/N₂ = 0.268 in air.

Next, the areal density of nitrogen in SiN_x membranes is considered to test the quantification results. As the nitrogen concentration (at/nm³) in low-stress SiN_x has been reported to be ~45 (at/nm³) [185], the nominal areal density can be calculated if the thickness of the SiN_x is

known. As the air-cell enclosure includes two membranes, the total SiN_x thickness is 42(top) + 38(bottom) = 80.2 nm based on reflectometer measurements. Thus, the nominal areal density of the two SiN_x membranes is 3609 at/nm², considering a vacuum cell. The EELS quantification of nitrogen areal density is 3420 at/nm², which is within 5% of the nominal value.

Finally, the areal densities of N₂ and O₂ in the air-cell enclosure are considered. According to ideal gas law, the volume density of gas molecules at ambient pressure is 0.0247 molecules/nm³. In the thickness of the cell, the bulging effect of the SiN_x membranes under the pressure difference in a TEM column also needs to be considered [120]. The maximum deflection at the center of a bulged rectangular SiN_x membrane can be estimated by the following equation:

$$p = \frac{2t\sigma_0}{a^2}d + \frac{8Et}{6a^4(1-\nu^2)}d^3 \quad (6.7)$$

where p , t , σ_0 , a , d , E , ν are the pressure applied to the membrane, the thickness of the membrane, the residual stress, the half width of the membrane, the deflection at the center of the membrane, Young's modulus, the thickness of the membrane, and Poisson ratio, respectively. Eq. (6.7) validates when the aspect ratio the membrane is more than 4 which is true for both our chips. A schematic of a deflected membrane under pressure difference is shown in Figure 6.5. The residual stress is 250 MPa for the low stress nitride. Typical mechanical parameters are used for low stress SiN_x: $E=235$ GPa, $\nu=0.28$.

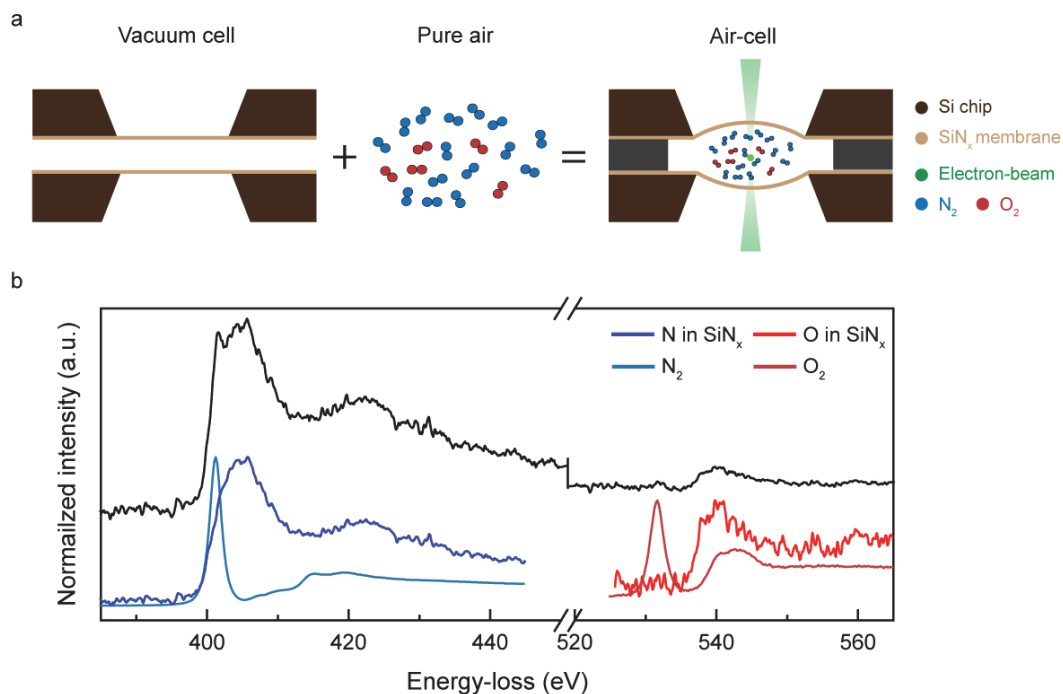


Figure 6.4. EELS quantification in air-cell. (a) A schematic of air-cell. (b) The EEL spectrum of air-cell enclosure and standard spectra of N₂, O₂, N in SiN_x, and O in SiN_x.

Under this experiment, the pressure inside the air-cell is assumed to be 1 atm as the inlet/outlet of the tubes are open to ambient conditions. The half width of the membrane, a , is 25 nm for both our top and bottom chips. Thus, the bulging equation gives $d = 1.2 \mu\text{m}$ of the deflection at the center of the membrane. Considering two membranes and 1 μm spacer, the maximum thickness of the cell is $\sim 3.4 \mu\text{m}$. Thus, the nominal maximum areal density of gas molecules in a bulged air-cell is 168 at/nm^2 . The areal density of air, based on the EELS quantification, is $109+449=549 \text{ at/nm}^2$ showing that the analysis gives an augmented value by 226%. The large discrepancy of the quantification remains unclear. It could be related to a possible erroneous estimation of either the pressure inside the cell or the thickness in the air-cell itself.

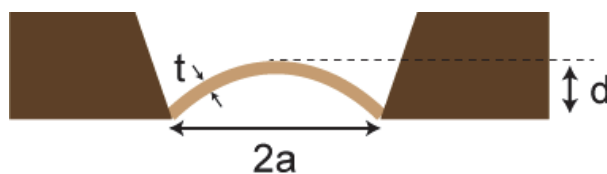


Figure 6.5. A deflected membrane under pressure difference. $2a$ is the width of the membrane. d is the deflection of at the center of the membrane. t is the thickness of the membrane.

Although the standard-based EELS quantification of the air-cell enclosure gives an O/N ratio that matches the nominal value of air, discrepancies of the calculation of the areal density can still occur. In fact, the quantification process strongly depends on the quality of the fitting. Change of the background or fitting windows may significantly affect the quantification results. EEL spectra with low signal-to-noise ratio can also result in poor fitting.

Table 6.1. EELS quantification results of air-cell

	Areal density (at/nm ²)	Relative composition
N in SiN _x	3420±170	1
N ₂	440±20	0.13
O in SiN _x	1370±70	0.4
O ₂	109±6	0.032

6.3.2 Liquid-cell enclosure with O₂ gas

The quantification procedure was further applied to quantify the amount of oxygen in liquid-cell enclosure. The system contained also the ultra-thin film Pt working electrode. The cell was initially filled with 0.1 M KOH electrolyte and the inlet/outlet tubes were closed to ensure the cell was fully saturated with liquid. Later, a high anodic potential at 2.5 V versus RHE was applied to generate O₂ gas in the cell. EELS was continuously acquired when the CA was applied. The O₂ gas bubble created a thin-film liquid condition which is beneficial for EELS acquisition. A schematic illustration of the presence of the O₂ gas in the liquid-cell enclosure is shown Figure 6.6a. The EELS of N K and O K and the standard spectra for fitting and

quantification are shown Figure 6.6b. Oxygen in the liquid electrolyte and SiN_x membranes are seen as a single standard spectrum. As with MLLS fitting, including similar standards in the system may result in overfitting artifacts. Thus, using a single standard spectrum for similar standards could avoid overfitting. The quantification results are shown in Table 6.2. The total SiN_x membrane thickness was 69 nm for this cell, giving a nominal 3105 (at/nm²). The quantification results indicate 2090 at/nm² for N which is low by 32% of the nominal areal density. The discrepancy may be related to the Pt working electrode which leads to noisier EEL spectra and affects the fitting. Interestingly, the quantification results show molecular nitrogen also. This may be attributed to the dissolved N₂ in the electrolyte which can precipitate when the gas bubble forms.

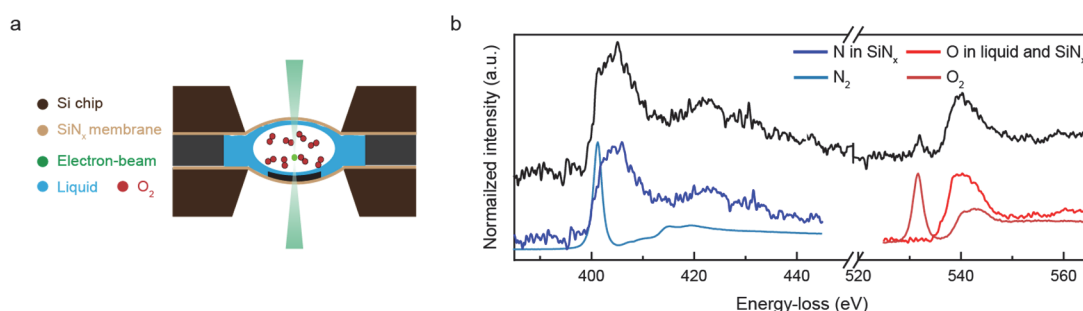


Figure 6.6. EELS quantification in liquid-cell with O₂. (a) A schematic illustration of a O₂ in a liquid-cell enclosure. (b) The EELS spectrum of liquid-cell with O₂ gas and the standard spectrum that were used to perform quantification.

Table 6.2. EELS quantification of liquid-cell with a O₂ gas

	Areal density (at/nm ²)	Relative composition
N in SiN _x	2090±100	0.5
N ₂	291±15	0.07
O in liquid and SiN _x	4200±70	1
O ₂	820±40	0.2

6.3.3 Discussion on areal density of O₂

The quantification results show that the areal density of O₂ is 820 at/nm². To validate the areal density results, the value of the nominal areal density of the O₂ bubble needs to be known. However, it is difficult to calculate this value in the cell enclosure based on the current response of the CA measurements. Typically, when the potential is applied, molecular oxygen is produced and it is initially dissolved in the liquid electrolyte. The formation of a gas bubble indicates the release of the supersaturation of gas in the electrolyte. However, not all the produced O₂ is responsible for the formation of the bubble. Some O₂ may dissolve in the liquid electrolyte. Additionally, O₂ bubble may form outside the electron transparent region. Another factor is that the pressure of the gas bubble is unknown so the nominal volume density cannot be known. These factors make the calculation of the nominal value of the O₂ areal density in a bubble difficult. Thus, it remains challenging to judge the areal density value under this condition.

6.4 Conclusions

In this chapter, an approach to quantify molecular gas in a cell enclosure using EELS quantification was demonstrated. The quantification process was based on multiple linear square fitting of standard spectra. It was shown that the contribution of molecular oxygen fine structure in EELS can be separated and quantified. The quantification process was first tested in an air-cell enclosure. The quantified O/N ratio matched the nominal values. However, discrepancies occurred in the absolute values of the areal density. Further, EELS quantification was applied to the quantification of OER conditions on a Pt working electrode under chronoamperometry. Still, discrepancies emerged in the evaluation of the areal density. Optimization of the EELS quantification process is needed to have reliable quantification results. Better quality EEL spectra could improve the accuracy of the quantification and reduce discrepancies.

Chapter 7 Conclusions and Perspectives

The work presented herein involved the development and application of (scanning) transmission electron microscopy ((S)TEM) techniques for probing oxygen-evolving oxide catalysts. The contribution concerned all aspects of these materials; from the as-synthesized powders, to their lab-on-a-chip characterization and postmortem analysis, to their dynamic monitoring under realistic conditions and towards the quantification of active surfaces.

In detail, we first focused on the surface characterizations and postmortem studies of oxygen evolution reaction (OER) oxide catalysts. (S)TEM techniques combining imaging and spectroscopy were used to characterize one of the most active OER oxide catalysts, perovskite $\text{Ba}_{0.5}\text{Sr}_{0.5}\text{Co}_{0.8}\text{Fe}_{0.2}\text{O}_{3-\delta}$ (BSCF). The characterization revealed a unique surface structure, a pristine Co/Fe spinel-like surface with Co^{2+} , prior to OER. The Co/Fe spinel-like surface was linked to OER-active CoFe oxyhydroxide phase transformation by relating to electrochemical measurements. The findings suggest that (S)TEM techniques that provide information of morphology, crystal structure, composition, and valence were crucial for understanding the pristine surface of OER catalysts after immersion in electrolyte. Further, the postmortem and identical location (S)TEM studies based on lab-on-a-chip setup revealed morphological and chemical information after OER. The unique lab-on-a-chip setup ensured the probed catalyst particles were exposed to liquid electrolyte after electrochemical operations. Chemically stable but weak Co/Fe surface after OER was discovered and explained via a reversible Co/Fe oxyhydroxide surface reconstruction mechanism occurring on the spinel-like surface. This part of the thesis shows the crucial role that surface-sensitive (S)TEM techniques and lab-on-a-chip setup can help understand the surfaces of catalysts and can provide a new characterization framework aiding development of novel catalysts.

Further, we concentrated on operando studies of Co-based oxide OER catalysts using electrochemical liquid-phase (S)TEM to probe the solid-liquid interfacial interactions. Prior to operando experiments, I fabricated and optimized ultra-thin Pt working electrodes on MEMS chips that were implemented in the electrochemical liquid-phase (S)TEM in order to improve TEM imaging quality and enhance the signal-to-noise ratio for the electron energy-loss (EEL) spectra. Moreover, zero-loss energy filtered TEM was applied to enhance the contrast of operando TEM images. The results revealed potential-dependent contrast variation surrounding the Co-based oxide catalyst particles in the operando TEM image sequences. This unique contrast variation was attributed to liquid movement under potential cycling. The liquid movement was analyzed and further related to wetting dynamics at the solid-liquid interface. It was proposed that prior to OER the wetting behaviors were governed by electrowetting and surface transformation during cycling. The electrowetting induced an overall thinning of the liquid around the oxide particles due to interfacial charges, and the surface transformation of oxyhydroxide phase with hydrophilic character altered the electrowetting behavior. In the OER regime, molecular oxygen evolution was detected in real-time using electron energy-loss spectroscopy (EELS). The detection of O₂ evolution was fulfilled by probing the peak feature at O K edge. The evolution of O₂ correlated to further thinning of liquid surrounding the oxide particles. In a nutshell, we were able to introduce a characterization framework that opens a novel pathway towards the visualization and understanding of the solid-liquid interfacial interactions using electrochemical liquid-phase (S)TEM. It provides insights into physical wetting dynamics that could be related to chemical OER activity on oxide surface by analyzing the liquid movement and detecting the reaction products around single particle catalysts.

Finally, we explored a quantitative EELS characterization framework for probing molecular oxygen. As the O₂ evolution was qualitatively detected in EELS under OER conditions, it is crucial to quantify the amount of evolved O₂ to deepen the understanding of OER activity of single particle catalysts. An approach to quantitatively study molecular oxygen in electrochemical liquid-phase (S)TEM was demonstrated, following the multiple least linear square (MLLS) fitting methodology using standard reference EEL spectra. Using IrO₂ under OER conditions in a liquid-cell enclosure, the MLLS fitting revealed that molecular oxygen features of different components in O K edge can be decoupled, generating qualitative O₂ and electrolyte maps. The fitting coefficient can further link to areal density so the molecular

oxygen can be quantified. However, discrepancies occur while the quantification workflow was tested by applying to cell-enclosure with known composition. Further improvement and optimization are required to have reliable and robust quantitative characterization framework of probing molecular oxygen.

Using the developed characterization methodology, future advancements in order to understand the interfacial phenomena at solid-liquid interface using electrochemical liquid-phase (S)TEM is envisioned. Interfacial phenomena such as accumulation of interfacial charge and charge transfer processes are key to heterogeneous electrocatalysis but direct probing of the phenomena remains challenging. Recently, it was shown that the accumulated charge at the solid-liquid interface is related to OER rate [186]. Further understanding of the interfacial charge can thus aid the understanding of the OER mechanism. Although electrochemical liquid-phase (S)TEM cannot directly image the interfacial charge, recent advancements in 4D-STEM techniques opens possibilities to probe local charge at the interface. Other than interfacial charge, probing the reaction intermediates such as adsorbates at the solid-liquid interface during OER can also be beneficial for understanding the mechanism. Recently, OER mechanism on oxide surface was proposed to follow nonconcerted proton-electron transfer at the interface, which is based on measuring the pH-dependency of the OER activity [187]. Probing the reaction intermediates as well as interfacial charge can further deepen the understanding of how proton and electron transfer occurs during OER. Operando EELS can potentially provide insights into reaction intermediates if the spectrum quality is sufficient to resolve fine structures, and the electron-beam induced effects are mitigated to avoid the damage of the reaction intermediates and the alteration of the electrolyte while probing.

In addition to interfacial phenomena during OER, establishment of a robust and reliable EELS characterization framework for probing molecular oxygen could be particular important for understanding OER activity of the catalysts in electrochemical liquid-phase (S)TEM. The activity comparison of single-particle catalysts can thus be realized when the amount of the evolved oxygen can be reliably compared. Moreover, this could potentially help identify the active sites on the catalytic surfaces at single-particle level. This site-specific and quantitative electron probing framework can provide information of whether the defects or facets on single particle catalysts are more active for OER, aiding the catalyst design protocols. Further,

quantification of reaction products can be generalized to quantify both reactants (OH^-) in liquid and products (O_2) in real-time. The conversion rate of the O_2 production during catalytic reactions can be acquired, providing further understanding of OER kinetics. This quantitative EELS characterization framework requires increasing the quality of EEL spectra with lower noise and higher energy resolution and, thus, further developments of liquid-cell enclosures and advancements of instruments are requested.

Interestingly, using electron microscopy techniques for OER catalysts can be further extended and applied to other more complicated electrocatalytic reactions such as CO_2 reduction or N_2 reduction reactions that involve various product formation. Selectivity of the catalytic products can be understood in a site-specific way when the different products can be probed in real-time.

Appendix A

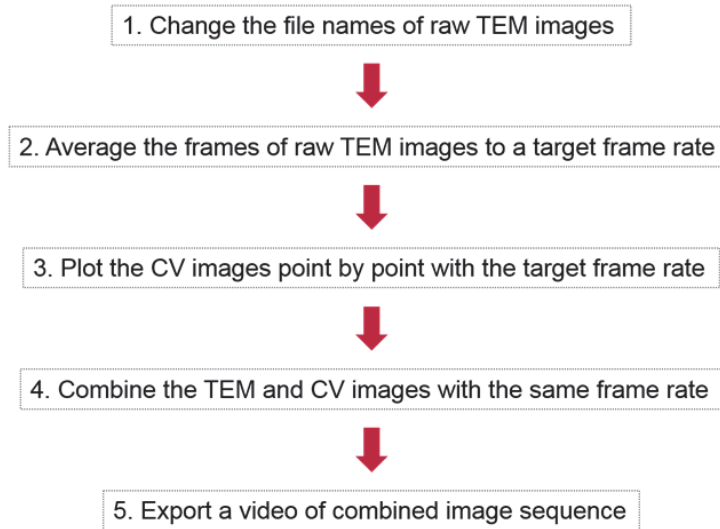
Runcard of the fabrication of the electrochemical chips

Step N°	Description	Equipment	Program / Parameters	Remarks
0	WAFER			
0.1	Siltronix 200 um Si wafer			1 wafer
1	SIN DEPOSITION			
1.1	RCA without SRD	Z3/WB		
1.2	Low stress SIN desposition	Z3/EP1.1 2 LPCVD Nitride	Isnt 50 nm	50 nm
2	PHOTOLITHOGRAPHY - Alignment mark and backside holes			
2.1	PR frontside	Z1/ACS200	ECI 3007 1.2um HMDS	
2.2	PR backside	Z1/ACS200	ECI 3007 1.2um HMDS no BSR	
2.3	PR expose Alignment mark	Z16/MLA150	Dose 150 Defocus -1	
2.4	PR develop	Z1/ACS200	CMdev 4in ECI 3007 1um2	
2.5	PR expose backside holes	Z16/MLA150	Dose 150 Defocus -1	
2.6	PR develop	Z1/ACS200	CMdev 4in ECI 3007 1um2	
3	SIN dry etch - Alignment mark and backside holes			
3.1	Frontside alignment mark etch	Z2/SP7S	SiO2 PR 3.1 Soft 18sec	
3.2	Backside hole etch	Z2/SP7S	SiO2 PR 3.1 Soft 10sec	Oversch
4	PR strip			
3.1	O2 plasma	Z2/Tepla GiGabatch	PR Strip High Power 2min	
3.2	Remove 1165	Z2/UFT Resist	Remove then DI rinse	
3.3	O2 plasma	Z2/Tepla GiGabatch	PR Strip High Power 5min	
5	KOH etching - Membranes			
5.1	KOH etching	Z14/Base wet bench	20% KOH 85°C 2hrs30mins	rel uniform some windows are big. Need to tune etching time
5.2	HCl neutralization	Z14/Acid wet bench	37% HCl 5 hrs	
5.3	DI water rinse	Z2/UFT Resist		
6	PHOTOLITHOGRAPHY - Pt layer			
6.1	Stick dummy wafer	Z6/RC8	Protect membranes	
6.2	PR-LOR coating	Z6/EG150	Dehydration, AZ1512(1.1 um) on LOR (0.4um)	
6.2	PR expose Pt layer	Z16/MLA150	Dose 65 Defocus -2	
6.3	PR develop	Z1/ACS200	AZ1512on LOR 0um48	
7	TI-Pt EVAPORATION			
7.1	Pt Deposition	Z4/ LAB600H	5 nm	
7.2	Pt Deposition	Z4/ LAB600H	50 nm	
8	LIFT-OFF			
8.1	Remove 1165	Z1/ Plade Solvent	overnight	Better to use clean remover1165. Ouz the lift-off dust may get into cavity
8.2	IPA then DI rinse	Z1/ Plade Solvent		
8.3	Remove dummy wafer	Z6/RC8		
8.4	PR residues remove	Z2/UFT Resist	half cycle	
9	PHOTOLITHOGRAPHY - Au layer			
9.1	Stick dummy wafer	Z6/RC8	Protect membranes while coating	
9.2	PR-LOR coating	Z6/EG150	Dehydration, AZ1512(1.1 um) on LOR (0.4um)	Remember to coat dummy first
9.3	PR expose Pt layer	Z16/MLA150	Dose 65 Defocus -2	
9.4	PR develop	Z1/ACS200	AZ1512on LOR 0um48	
10	TI-Au EVAPORATION			
10.1	TI Deposition	Z4/ LAB600H	5 nm	
10.2	Au Deposition	Z4/ LAB600H	100 nm	
11	LIFT-OFF			
11.1	Remove 1165	Z1/ Plade Solvent	overweekend	
11.2	IPA then DI rinse	Z1/ Plade Solvent		
11.3	Remove dummy wafer	Z6/RC8		
11.4	PR residues remove	Z2/UFT Resist	half cycle	
12	SiO2 passivation layer			
12.1	SiO2 sputtering	Z4/Solider	SiO2 1.0um30s	Too thick, SiO2 will create stress on SIN membranes. Thinner next time
12.2	PR coating	Z1/ACS200	ECI 3007 1.2um HMDS	
12.3	PR expose passivation	Z16/MLA150	Dose 175 Defocus -1	
12.4	PR develop	Z1/ACS200	CMdev 4in ECI 3007 1um5 PEB	PEB seems to make PR to be removed
12.5	BHF SiO2 etch	Z2/Plade oxide	1 mm 30s	Check with reflectometer to confirm it is fully etched
12.6	PR remove	Z2/ UFT Resist	full cycle	Some PR cannot be removed even immerse into remover1165 overnight. Maybe PEB makes PR stronger
13	Dicing PR protection			
13.1	Stick dummy wafer	Z6/RC8	Protect membranes while coating	
13.1	PR coating	Z6/EG150	AZ8260 10 um dehydrate	
14	Dicing			
15	PR protection remove			
15.1	PR remove	Z2/UFT Resist	full cycle cycle	

Appendix B

Synchronization of TEM image sequence and CV curves

The process flow of analyzing the operando data is shown below. Each step is explained with the attached Mathematica codes.



1. Change the file name of the raw TEM images

The StreamPix exported the image sequence with names such as "xxx-001", "xxx-002", "xxx-003", etc. It thus causes a problem of specifying the images while they are imported to Mathematica. Therefore, I wrote a function to change the file to "xxx_1", "xxx_2", "xxx_3". The final numbers can be treated as integers instead of strings.

```
Rename[renameraw1_String] := Module[{initialfilename, afterfilename},  
  nbd = NotebookDirectory []; rawfolder = nbd <> "../TEMraw";  
  SetDirectory [rawfolder];  
  initialfilename = FileNames[{"*.tif", "*.jpg"}];  
  afterfilename =  
    Table[ToString[renameraw1] <> ToString[i] <> ".jpg", {i, 1,  
      Length[initialfilename]}];  
  MapThread[RenameFile, {initialfilename, afterfilename}];  
]
```

2. Average the frames of raw TEM images

After rename the raw TEM images, the raw TEM images can be specified correctly. The raw TEM images with high frame rate normally are relatively noisy. Averaging the frames is needed to improve the image quality. A function "AVGframe" is written. First, it creates a TEM folder for the averaged TEM images. Then, it imports the raw TEM images, does the averaging, and exports the averaged TEM images to the TEM folder according to the target frame rates. The build-in function ImageData is used to take the pixel value of the images. ImageAdjust function is used to auto tune the contrast and brightness.

```
AVGframe[renameraw2_String, originfps_, targetfps_, imagesize_,
  AVGname_String] :=
Block[{file, divide, partfile, imageimport, imagearray, dividefactor,
  AVG, AVGimages, partAVG},
  nbd = NotebookDirectory [];
  CreateDirectory[nbd <> "../TEM"];
  TEMfolder = nbd <> "../TEM";
  rawfolder = nbd <> "../TEMraw";
  file = FileNames[ToString[rawfolder] <> "/" <> "*.jpg"];
  dividefactor = IntegerPart[originfps/targetfps];
  partAVG[n_] := Block[{}],
  imageimport =
  Table[ Import [
    ToString[rawfolder] <> "/" <> ToString[renameraw2] <>
    ToString[i] <> ".jpg", ImageSize -> imagesize], {i,
    1 + (n - 1)*dividefactor, n*dividefactor}];
  imagearray[i_] := ImageData[imageimport[[i]]];
  AVG = Sum[imagearray[i], {i, 1, dividefactor}]/dividefactor;
  AVGimages = ImageAdjust[Image[AVG], {0, 1}];
  Export[ToString[TEMfolder] <> "/" <> ToString[AVGname] <>
    ToString[n] <> ".jpg", AVGimages];
];
Parallelize[
  Map[partAVG[#] &, Range[1, IntegerPart[Length[file]/dividefactor]]]]
]
```

3. Plot the CV images

The CV measurements from a potentiostat generate a .dat file, that is, a (x,y) file with x is potential and y is current. A "CVplot" function is written to generate images of (potential, current density) plot of CV data with the same frame rate of the averaged TEM images and export to the folder CV. As the step size (V) and scan rate (V/s) are given, the original CV dataset can be binned to the same frame rate of averaged TEM images. For example, the potential step size is 1 mV and the scan rate is 20 mV/s, therefore, the data point rate is 20 data point per second. If the frame rate of the averaged TEM images is 2 fps, one can average every 10 data point to generate 2 data point per second. In this way, the CV data point rate and image frame rate are synchronized. The function later on exports the plot of CV point by point. The function also calibrates the potential to a certain specific value as well as divides the current by area to have current density.

```
CVplot[filename_String, RHEvalue_, area_, potentialstep_, scanrate_,
targetfps_, imagesize_, outputname_String] :=
Block[{file, files, data, dataRHE, binfactor, dividefactor,
dataDivide, dataMean, plotrangeboundary, g1},
nbd = NotebookDirectory [];
SetDirectory [nbd <> ".."];
data = Delete[Import[filename], 1];
dataRHE = data /. {E_, I_} :> {E + RHEvalue, I/area};
binfactor = IntegerPart[1/targetfps/(potentialstep/scanrate)];
dividefactor =
Partition[Table[i, {i, 1, Length[dataRHE]}], binfactor];
dataDivide =
dataRHE[[#]] & /@ dividefactor[[Range[1, Length[dividefactor]]]];
dataMean =
Table[{dataDivide[[i]][[All, 1]] // Mean,
dataDivide[[i]][[All, 2]] // Mean}, {i, 1,
Length[dividefactor]}];
plotrangeboundary = {{Min[dataMean[[All, 1]]],
Max[dataMean[[All, 1]]]}, {Min[dataMean[[All, 2]]],
Max[dataMean[[All, 2]]]}};
g1[i_Integer] :=
ListLinePlot[dataMean[[1 ;; i]], PlotRange -> plotrangeboundary,
```

```

PlotStyle -> {Thickness[0.003], Blue}, Frame -> True,
FrameLabel -> {Style["E (V vs. RHE)", 32],
  Style["I (mA^1/2(*SuperscriptBox[(cm^-2)]))", 32]},
FrameStyle ->
  Directive[Thick, Black, 26, FontFamily -> "Helvetica"],
AspectRatio -> 1, ImageSize -> {imagesize, imagesize},
Epilog -> {AbsolutePointSize [20], RGBColor [1, 0, 0],
  Point [Last [dataMean[[1 ;; i]]]}];
CreateDirectory[nbd <> "../CV"];
CVfolder = nbd <> "../CV";
Parallelize[
  Map[Export[
    ToString[CVfolder] <> "/" <> ToString[outputname] <>
    ToString[#] <> ".jpg", gl[#] &,
    Range[1, Length[dividefactor]]]]
]

```

4. Combine averaged TEM images and CV images

The two datasets: averaged TEM images and CV data point images are generated with the same frame rate. A function "Imagecombine" is written to combine two datasets at the same timing. For example, TEM image label 1 is combined with CV image label 1 to have synchronization.

```

Imagecombine[filenameTEM_String, filenameCV_String, imagesize_] :=
Block[{partcombine, imageadd, fileTEM, fileCV, filenum},
  nbd = NotebookDirectory [];
  CVfolder = nbd <> "../CV";
  TEMfolder = nbd <> "../TEM";
  fileTEM = FileNames[ToString[TEMfolder] <> "/" <> "*.jpg"];
  fileCV = FileNames[ToString[CVfolder] <> "/" <> "*.jpg"];
  filenum = Min[Length[fileTEM], Length[fileCV]];
  CreateDirectory[nbd <> "../Combine"];
  combinefolder = nbd <> "../Combine";

```



```
partcombine[x_] := Block[{TEMImage, CVImage},
  TEMImage =
  Import [ToString[TEMfolder] <> "/" <> ToString[filenameTEM] <>
    ToString [x] <> ".jpg", ImageSize -> imagesize];
  CVImage =
  Import [ToString[CVfolder] <> "/" <> ToString[filenameCV] <>
    ToString [x] <> ".jpg", ImageSize -> imagesize];
  imageadd = ImageAssemble[{TEMImage, CVImage}];
  Export[
    ToString[combinefolder] <> "/" <> ToString[filenameTEM] <>
      "combine_" <> ToString[x] <> ".jpg", imageadd
  ];
  Parallelize[Map[partcombine[#] &, Range[1, filenum]]]
]
```

5. Export a video of the combined image sequence

A function "ExportVideo" is written to export a video of the combined image sequence. The exported video can be speed up to certain times according to the input variable.

```
ExportVideo[filenameTEM_String, imageframerate_, faster_] :=
Block[{imagecombine, file},
  nbd = NotebookDirectory [];
  combinefolder = nbd <> "../Combine";
  file = FileNames[ToString[combinefolder] <> "/" <> "*.jpg"];
  imagecombine =
  ParallelTable[
    Import[ToString[combinefolder] <> "/" <> ToString[filenameTEM] <>
      "combine_" <> ToString [i] <> ".jpg"], {i, 1, Length[file]}];
  Export[ToString[nbd] <> "/" <> ToString[filenameTEM] <>
    ToString[faster] <> ".X" <> ".mov", imagecombine,
  FrameRate -> imageframerate*faster, VideoEncoding -> "MPEG1VIDEO"]
]
```

6. Applying the functions for data processing

A cell with all the input variables is written in order to initiate the processing functions automatically. Once the input variables are set, the processing can run automatically including generating the folders and exporting images.

```
(*Raw TEM images file name*)renameraw = "BSCFonGC_20fps_";
(*exported average TEM image file name*)AVGTEMname = "BSCF_GC_2fps_";
(*the file name of raw CV.dat file*)CVrawfilename = "BSCFonGC_CV.dat";
(*CV image file name*)CVimagefilename = "BSCFonGC_CV_2fps_";
```

```
(*original fps during acquiring*)originfps = 20;
(*exported fps*)targetfps = 2;
(*video faster*)faster = 4;
```

```
(*exported average TEM image size*)TEMimagesize = 1024;
(*Image size of CV images*)CVimagesize = 1024;
(*combine image size...should same for both*)combineimagesize = 1024;
```

```
(*Convert to RHE*)RHEvalue = 0.967;
(*surface area(cm^2)*)area = 0.1;
(*data point in CV*)potentialstep = 0.001;
(*Scan rate in CV*)scanrate = 0.02;
```

```
Rename[renameraw]
AVGframe[renameraw, originfps, targetfps, TEMimagesize, AVGTEMname]
CVplot[CVrawfilename, RHEvalue, area, potentialstep, scanrate, \
targetfps, CVimagesize, CVimagefilename]
Imagecombine[AVGTEMname, CVimagefilename, combineimagesize]
ExportVideo[AVGTEMname, targetfps, faster]
```


Appendix C

Supporting Information of Chapter 4

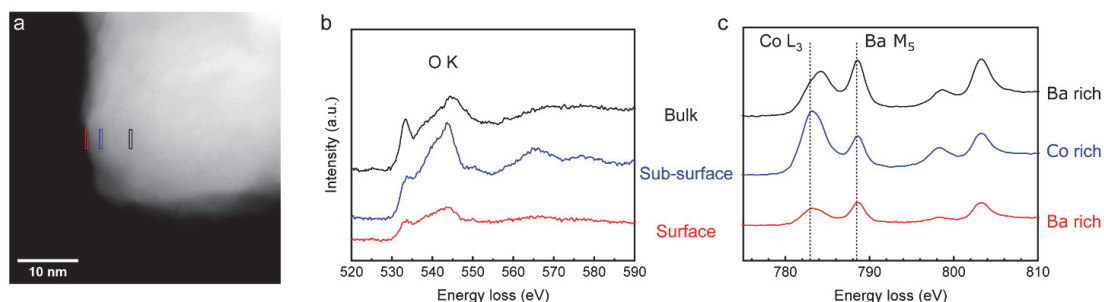


Figure C1. STEM-EELS analysis of a dry pristine BSCF particle. (a) HAADF-STEM image of the BSCF particle. (b) EEL spectra of O K edge of regions indicated in (a). (c) EEL spectra of Co L_{3,2} and Ba M_{5,4}. The surface of the BSCF particle shows a reduced oxidation state of Co (red and blue) and a Ba-rich composition at the most outer surface of the particle (red) prior to dispersing in isopropanol.

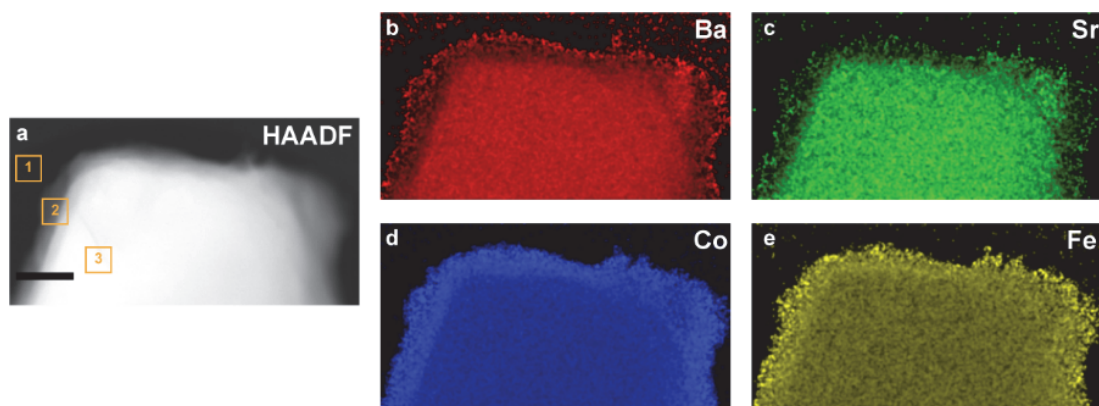


Figure C2. STEM-EDS analysis of a pristine BSCF particle dispersed in 0.1 M KOH. (a) HAADF-STEM image of the BSCF particle. The scale bar is 50 nm. 1-3 areas indicate the regions outside the particle, surface, and bulk, respectively. The corresponding quantification results are shown in Table S1. (b-e) EDS elemental maps of Ba, Sr, Co, and Fe showing a B site surface layer.

Table C1. Quantification results of the three regions indicated in yellow in Figure C2. A-site deficiency on the surface is highlighted in red.

Element	Atomic fraction (%)		
	Region 1 (outside)	Region 2 (surface)	Region 3 (bulk)
C	96.23	14.73	3.06
O	2.60	63.34	60.73
K	0.22	1.41	0.06
Fe	0.32	3.36	3.72
Co	0.32	12.92	14.02
Sr	0.00	2.41	10.41
Ba	0.31	1.84	8.00

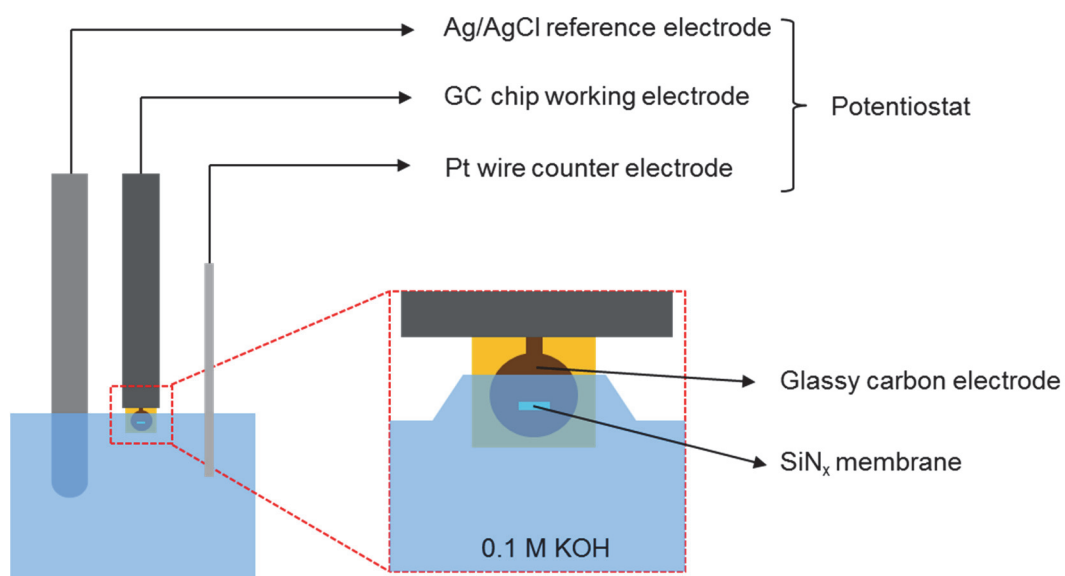


Figure C3. Schematic illustration of the immersion setup used for the electrochemical measurements. The membrane part on the glassy carbon chip is immersed in the KOH solution.

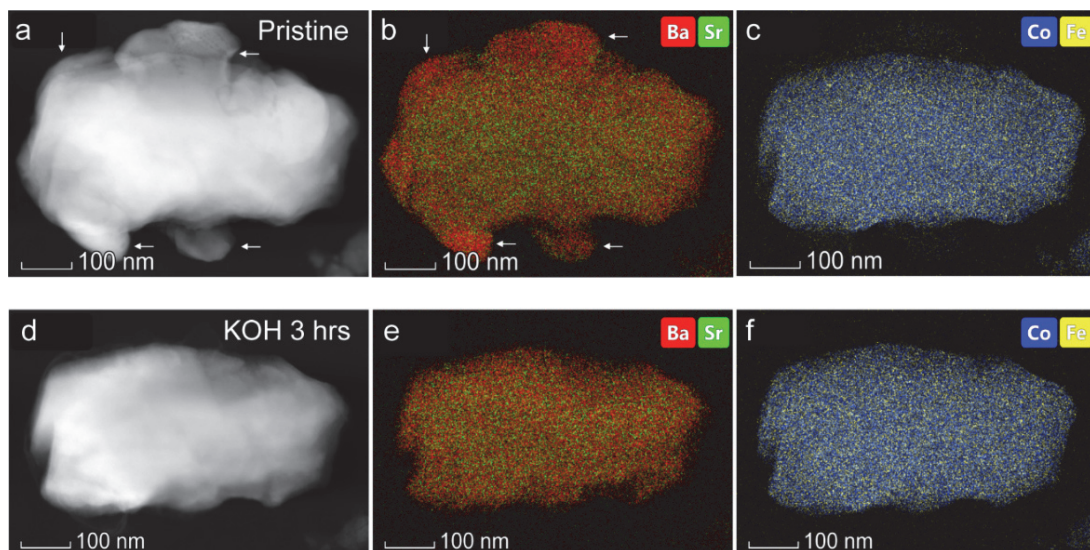


Figure C4. Dissolution of Ba/Sr-rich phases at BSCF surface after immersion in 0.1 M KOH for 3 h. (a) HAADF-STEM image of a pristine BSCF particle. (b) EDS elemental maps of Ba and Sr. White arrows indicate some of the large Ba/Sr rich secondary particles. (c) EDS elemental maps of Co and Fe. (d) HAADF-STEM image of the identical BSCF particle after immersion in KOH. (e, f) EDS elemental maps of Ba, Sr, Co, and Fe of the immersed in KOH BSCF particle.

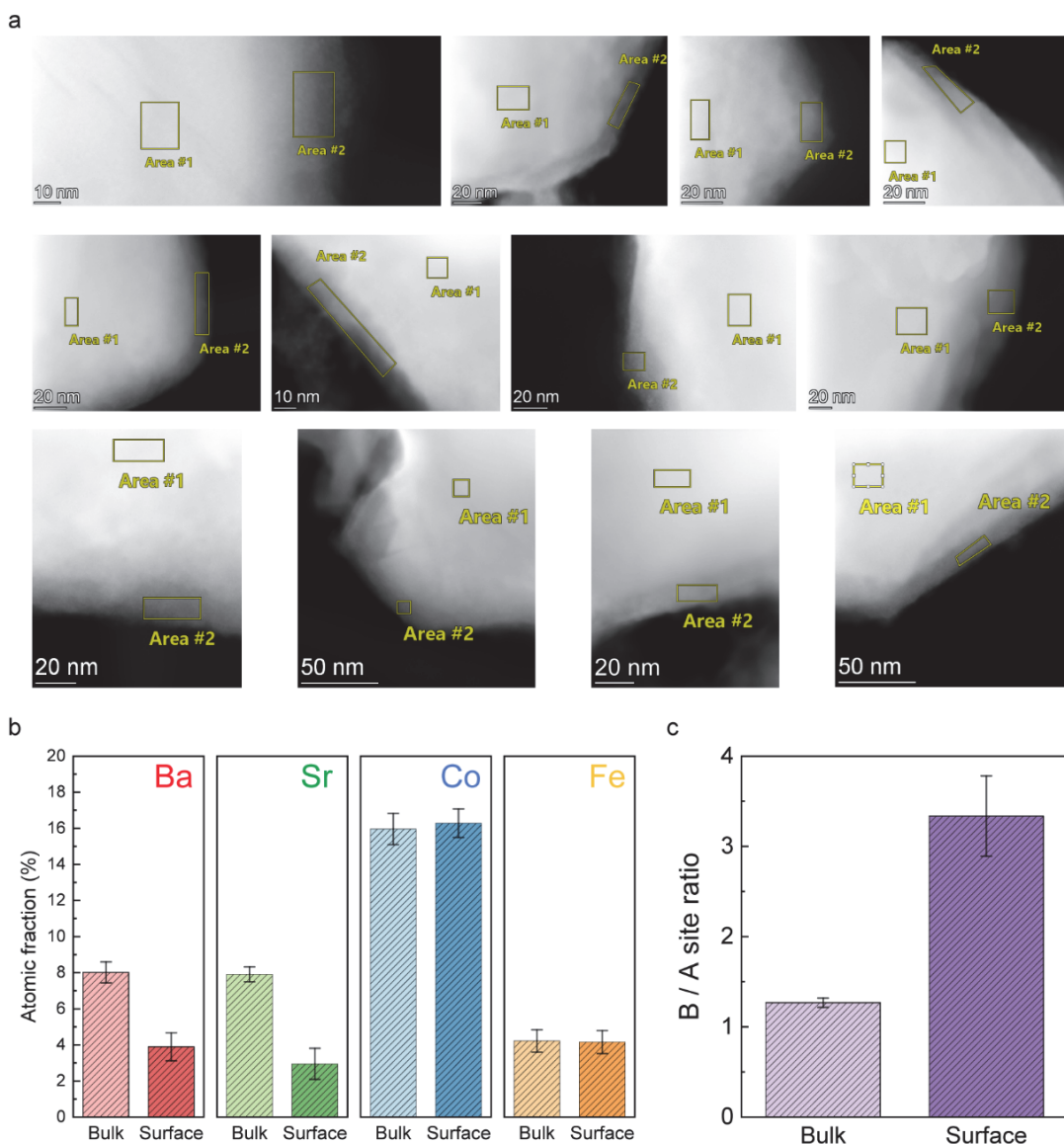


Figure C5. Statistical analysis of the composition of the surfaces and bulk in BSCF after immersion in 0.1 M KOH solution. (a) HAADF-STEM images of 12 BSCF particles showing areas near the surface. The annotated areas 1 and 2 are the regions of bulk and surface, respectively, that were used to acquire STEM-EDS spectra for quantification. (b) Bar chart showing the atomic fraction of Ba, Sr, Co, and Fe of the bulk and surface calculated from the 12 STEM-EDS quantification results. (c) Plot of the B/A site ratio of bulk and surface BSCF averaged across the measurements. Error bars represent the standard deviation.

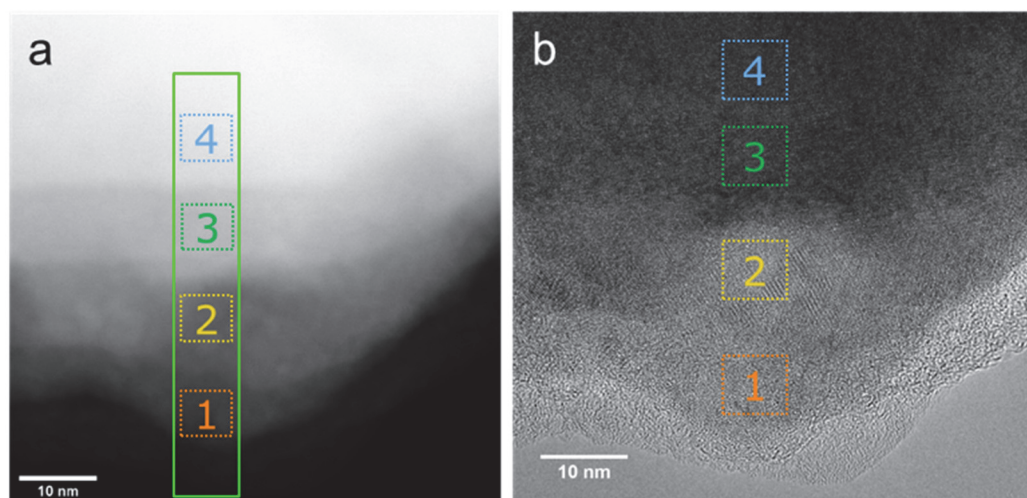


Figure C6. (a) HAADF-STEM image of BSCF near the surface. The green rectangle depicts the acquisition region for STEM-EELS data sets in Figure 4.2. (b) TEM image of the same BSCF surface as in (a). 1-4 indicate the regions that the selected area FFTs in Figure 4.2 were calculated.

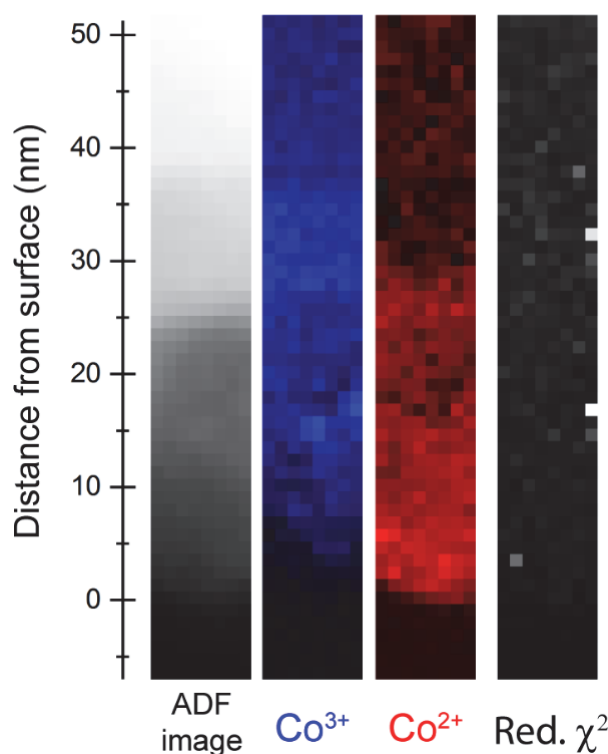
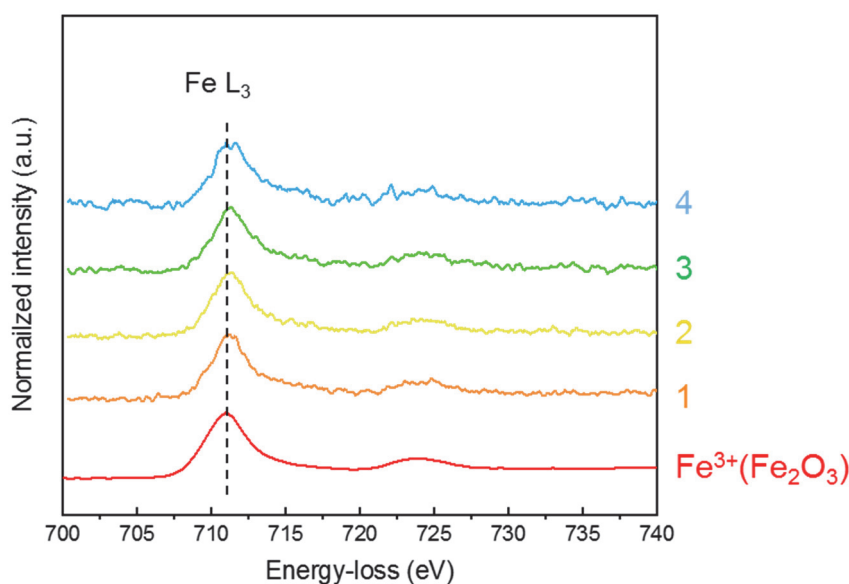
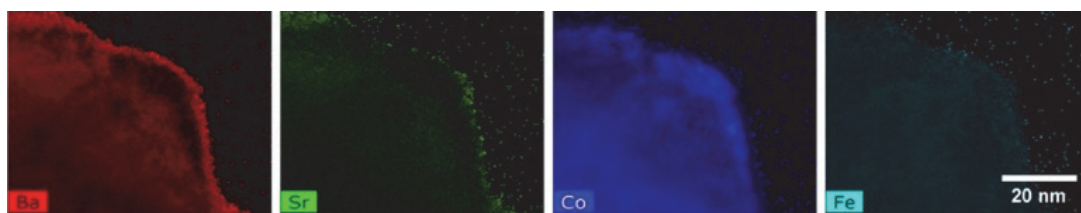


Figure C7. MLLS fitting of Co valence in EEL spectrum image. The MLLS fitting includes the Co L_3 peak (775-785 eV). The fitting was done in the Gatan Microscopy Suite (GMS) software and the fit-weights were set equal to 1. The reduced χ^2 reflects the average square deviation of each fitted point from the corresponding measured value. The randomized values of the χ^2 map confirm the unbiased fitting process.

Table C2. d-spacings of reflections for perovskite and spinel structure.

Perovskite $\text{Ba}_{0.5}\text{Sr}_{0.5}\text{Co}_{0.8}\text{Fe}_{0.2}\text{O}_{3-\delta}$ Cubic ($Pm\bar{3}m, a_0 = 3.99 \text{ \AA}$)	Spinel $(\text{Co, Fe})_3\text{O}_4$ Cubic ($Fd\bar{3}m, a_0 = 8.35 \text{ \AA}$)
3.99 \AA (1 0 0)	4.82 \AA (1 1 1)
2.82 \AA (1 0 1)	2.95 \AA (2 2 0)
2.30 \AA (1 1 1)	2.51 \AA (3 1 1)
1.96 \AA (2 0 0)	2.41 \AA (2 2 2)
1.78 \AA (2 0 1)	2.09 \AA (4 0 0)
1.63 \AA (2 1 1)	1.48 \AA (4 4 0)

**Figure C8.** EEL spectra showing the Fe $L_{3,2}$ edge of BSCF near the surface along with the Fe^{3+} reference. The 1-4 EEL spectra are extracted from Figure 2b. The Fe^{3+} (Fe_2O_3) reference spectrum is extracted from the EELS Atlas database implemented in the GMS software.**Figure C9.** STEM-EDS elemental maps of Ba, Sr, Co, and Fe. Spinel structure corresponds to Co-rich region in the map.

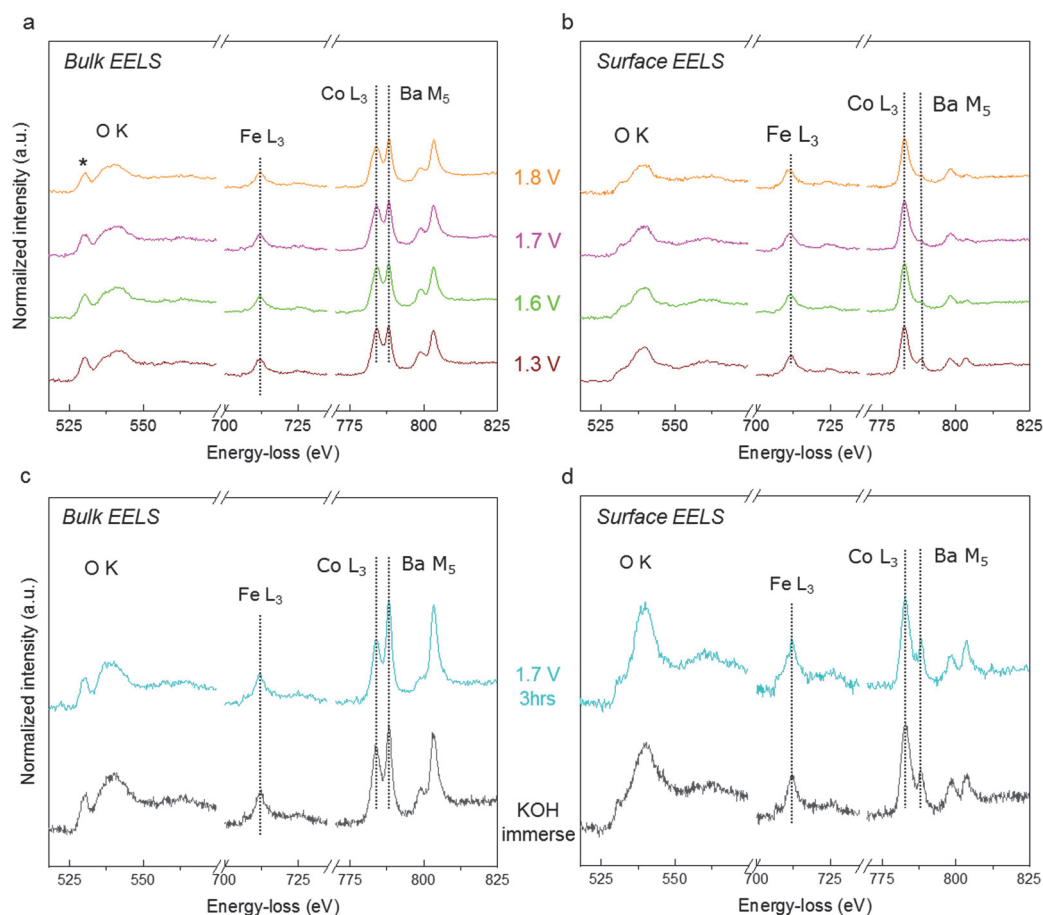


Figure C10. (a) Bulk and (b) surface EEL spectra showing the O K, Fe L_{3,2}, Co L_{3,2}, and Ba M_{5,4} edges of BSCF after chronoamperometric measurements (CA) at 1.3, 1.6, 1.7, and 1.8 V vs RHE for 1 min. (c) Bulk and (d) surface EEL spectra showing O K, Fe L_{3,2}, Co L_{3,2}, and Ba M_{5,4} edges after KOH immersion for 3 h (black lines) and after CA measurements at 1.7 V vs RHE for 3 h (cyan lines).

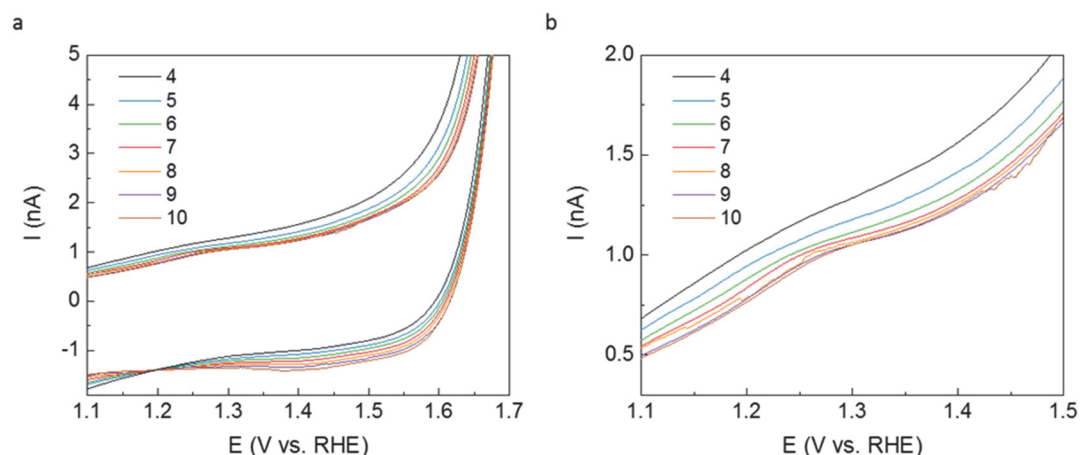


Figure C11. *In situ* CV measurements of BSCF in a liquid-cell TEM holder. (a) Plot depicting the measurements of 4th cycle to 10th cycle. (b) Close-up of voltage range between 1.1-1.5 V vs RHE depicting the pre-peak region during the anodic scan. The first three cycles are not shown because the underlying signal of the Pt current collector hinders the pre-peak detection. The Pt background signal decreases with increasing cycle number and, consequently, the pre-peak becomes more pronounced and is detectable starting from the 4th cycle.

Table C3. Prepeak positions* of *in situ* CV measurements of BSCF.

<i>Cycle number</i>	<i>Pre-peak position (V vs RHE)</i>
1	undetectable
2	undetectable
3	undetectable
4	1.306
5	1.301
6	1.304
7	1.307
8	1.304
9	1.313
10	1.320

*Note that the prepeak positions were determined using the minimum value from calculating the first derivative of smoothed CV curves (change of slope).

Appendix D

Supporting Information of Chapter 5

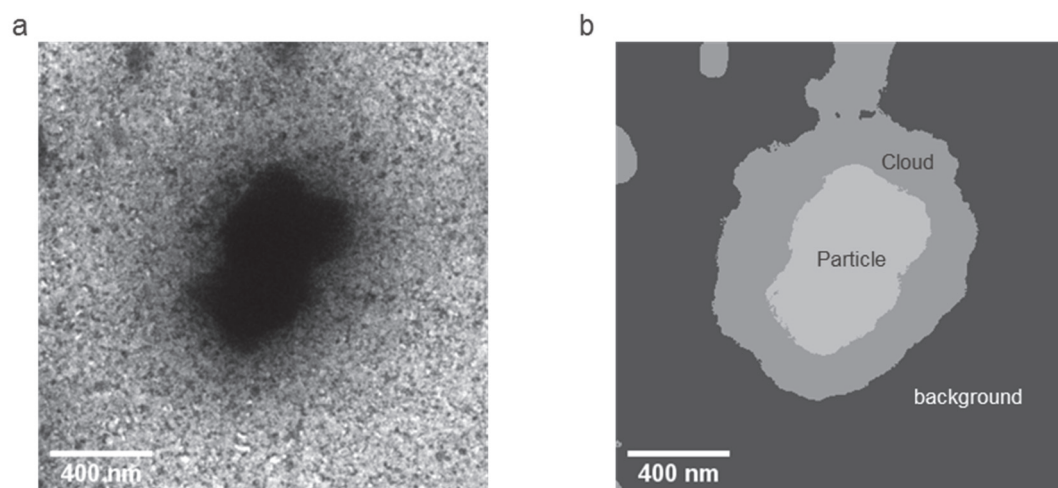


Figure D1. Segmented BF-TEM image of a BSCF particle surrounded by 0.1 M KOH solution. **a**, first frame of BF-TEM image. **b**, segmented image of particle, cloud, and background.

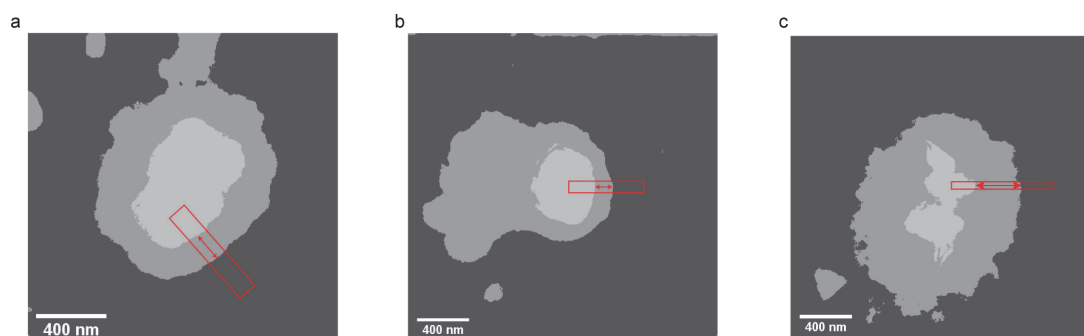


Figure D2. Segmentation of TEM images of three Co-based oxides. **a**, BSCF. **b**, Co_3O_4 . **c**, CoO . The TEM image sequences are segmented into three categories: Background (dark grey), Cloud (medium grey), and Particle (light grey). The red rectangles are used for the determination of the parameter cloud length (indicating with red arrows). The areas of cloud and particle within the rectangles were calculated and then the areas were divided by the width of the rectangles. The cloud lengths can be determined.

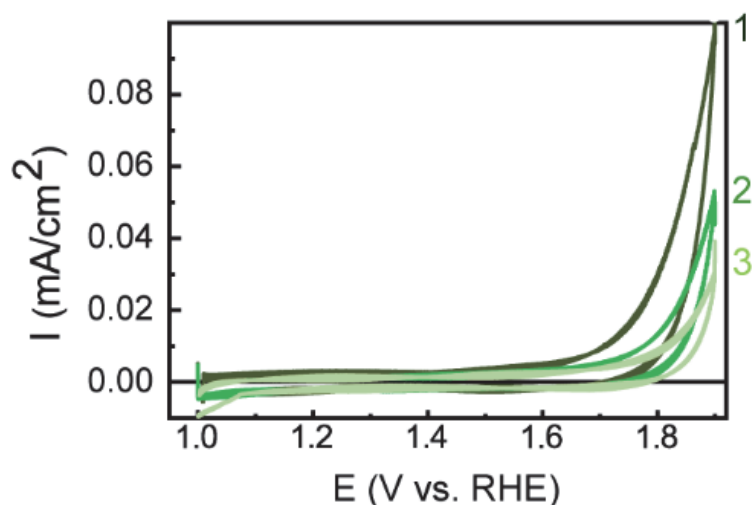


Figure D3. Polarization curves of the three CV cycles of BSCF during the operando EELS experiments. The scan rate is 20 mV/s. The reduction of the current density from the first to third cycles is due to the drift of quasi-reference Pt electrode.

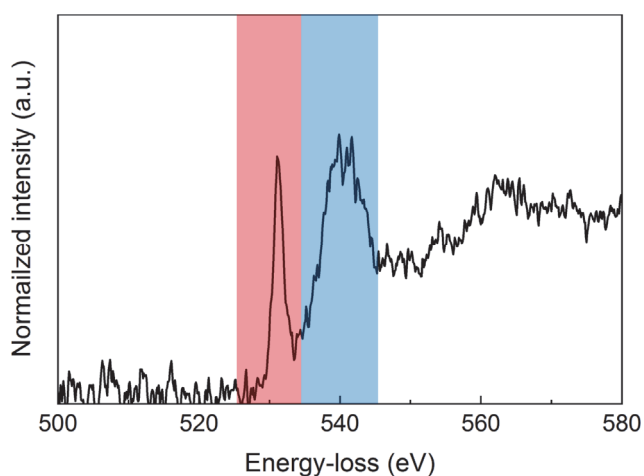


Figure D4. Core-loss O K EELS. The O₂ peak intensity ratio is defined as the molecular peak intensity in the range 529-534 eV (red shaded region) divided by the background intensity ranging from 535 to 545 eV (blue shaded region).

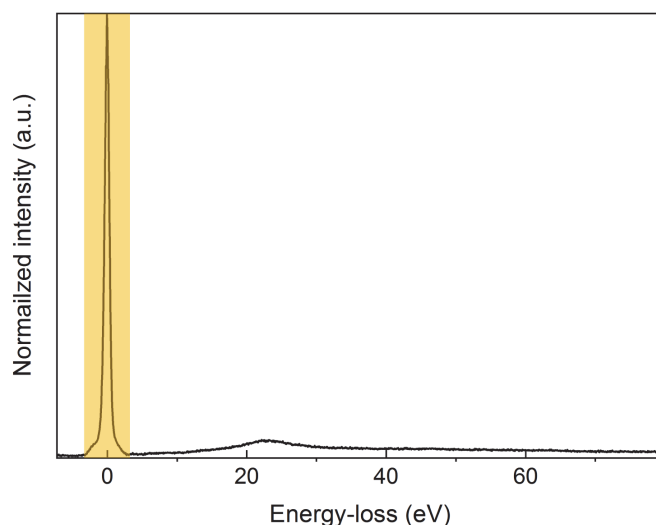


Figure D5. Low-loss EELS. The relative thickness (t/λ) is defined as $-\ln\left(\frac{\text{intensity of the area of the zero-loss peak (yellow shaded region)}}{\text{entire EEL spectrum intensity}}\right)$. This measurement gives an indication of the total thickness of the liquid cell.

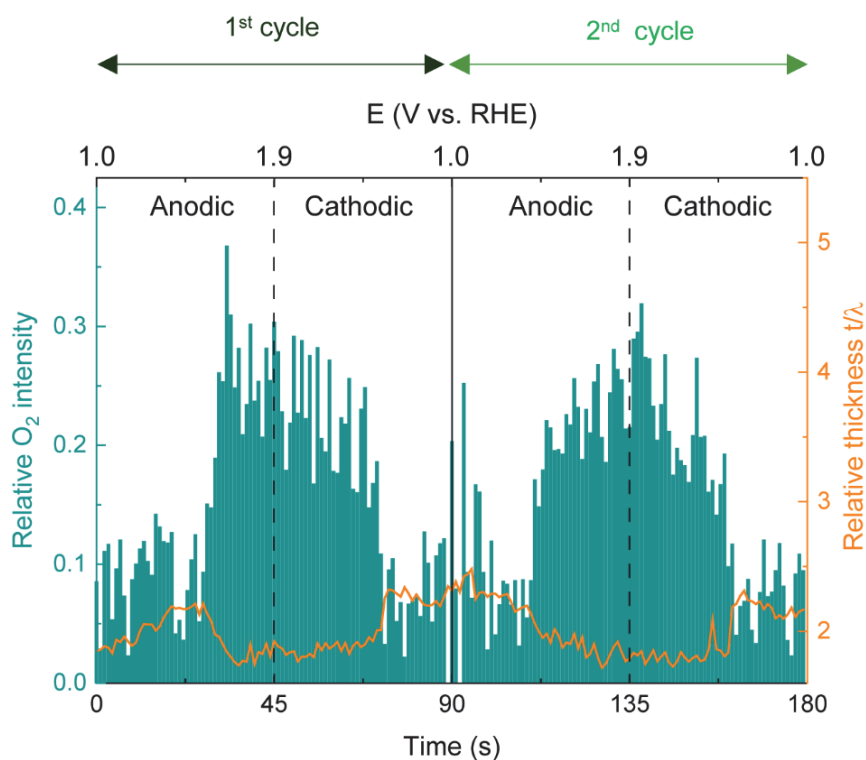


Figure D6. Operando EELS analysis of Co_3O_4 under potential cycling. Plot of relative O_2 intensity (green) and thickness (orange curve) as a function of elapsed time (bottom) and applied potential (top) corresponding to two CV cycles.

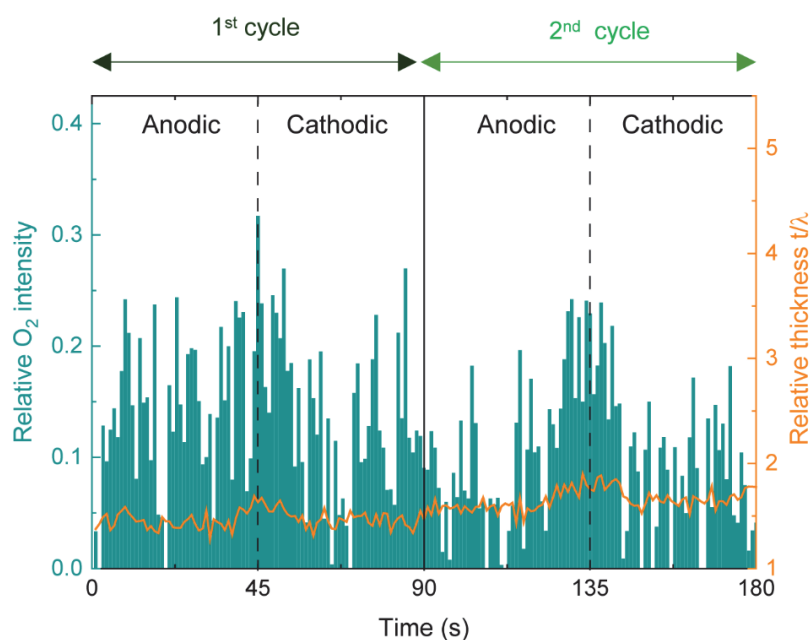


Figure D7. Operando EELS analysis of the Pt electrode under potential cycling. Plot of O₂ peak intensity (green) and relative thickness (orange curve) as a function of elapsed time (bottom) and applied potential (top) corresponding to two CV cycles.

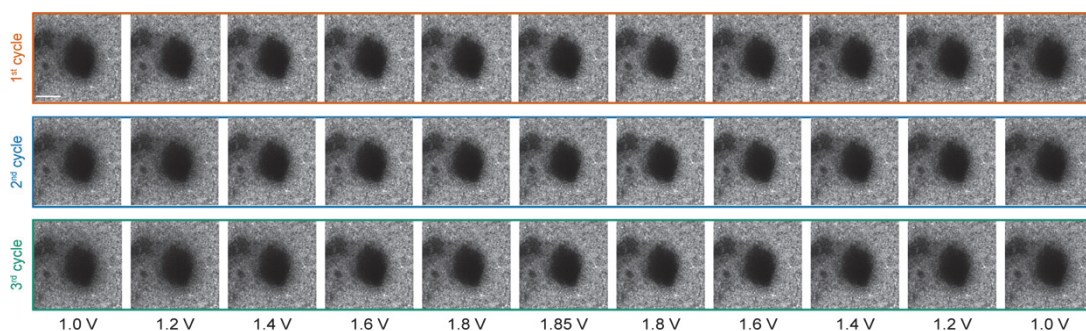


Figure D8. BF-TEM images of Co₃O₄ at different potential stages for the first, second and third cycles. Scale bar, 400 nm.

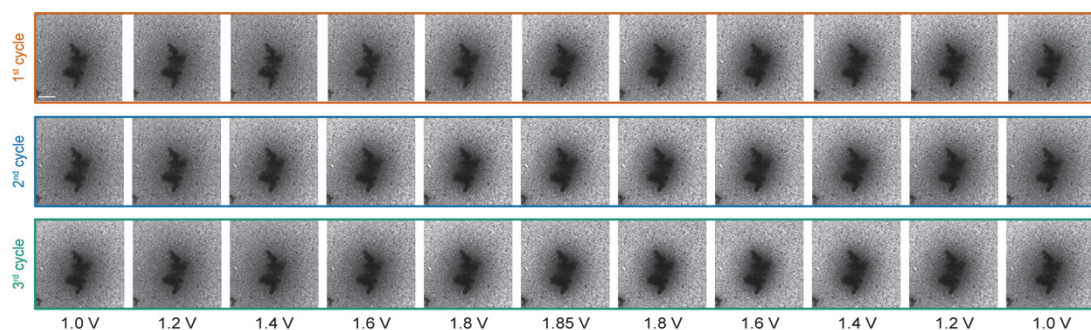


Figure D9. BF-TEM images of CoO at different potential stages for the first, second and third cycles. Scale bar, 400 nm.

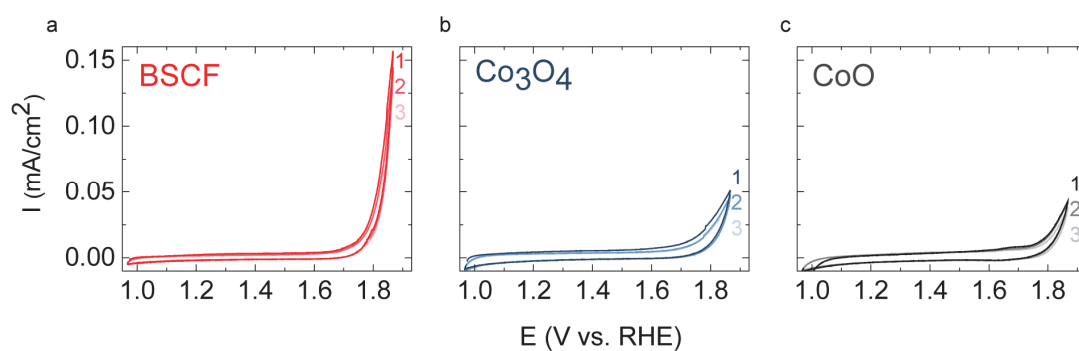


Figure D10. The polarization curves of CV of BSCF (red), Co_3O_4 (blue), and CoO (black) in liquid-cell enclosure. The scan rate is 20 mV/s.

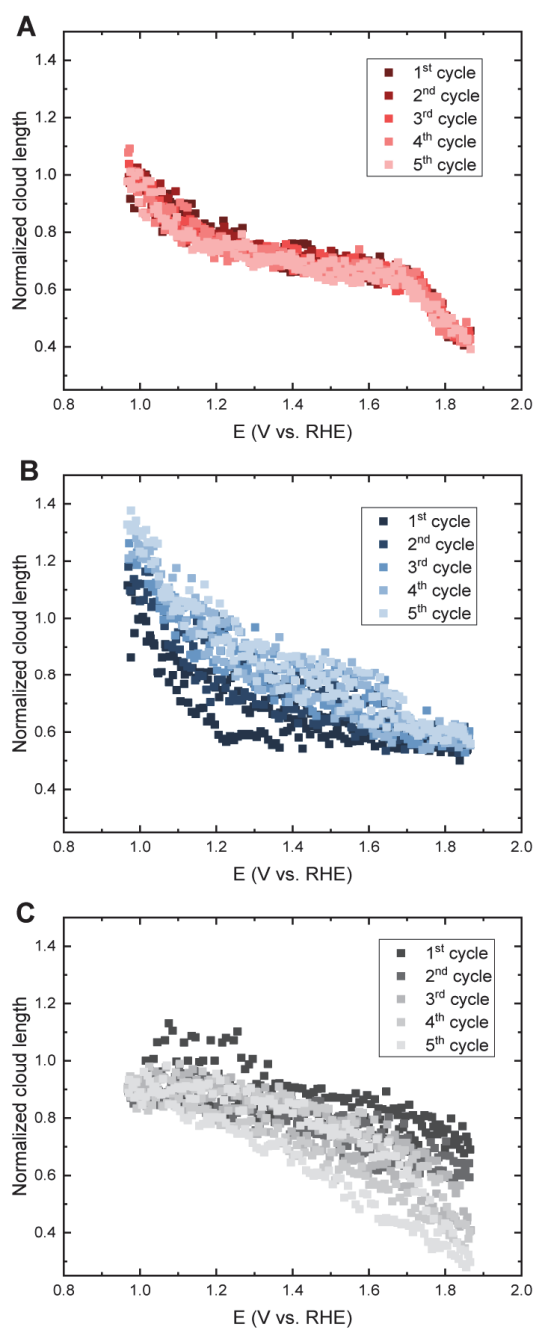


Figure D11. Plot of normalized cloud length as a function of applied potential for the complete 5 cycles. a, BSCF. b, Co₃O₄. c, CoO.

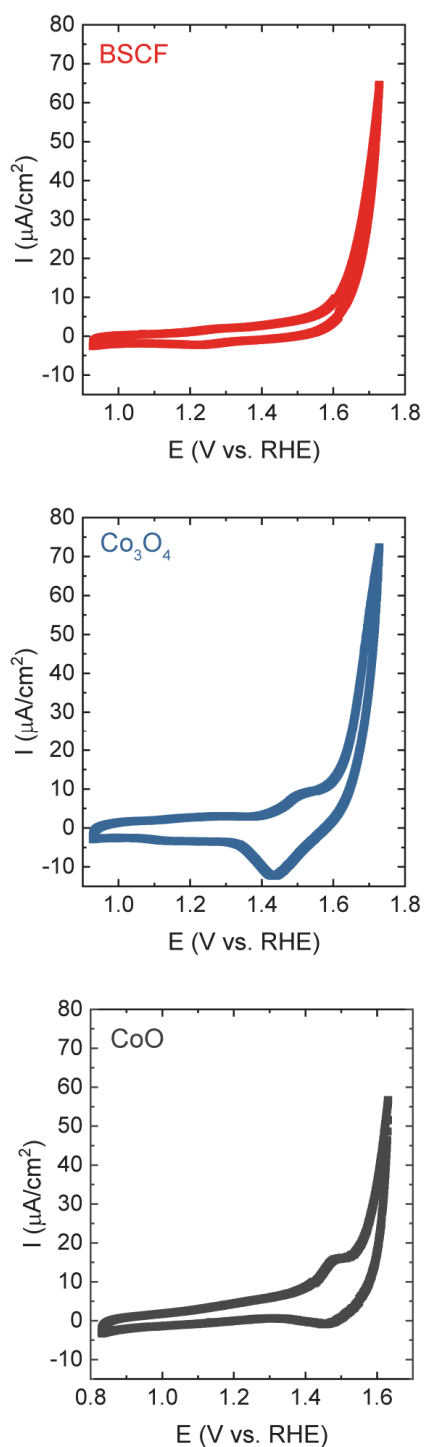


Figure D12. The full range of polarization curves in Figure 5.3b-d. BSCF (red), Co_3O_4 (blue), and CoO (black) in liquid-cell enclosure. The scan rate is 10 mV/s. It is noted that the OER currents of different oxides in the CVs acquired in the liquid cell TEM measurements are not comparable due to variations with the particle loading on the Pt electrode and the volume of the liquid solution.

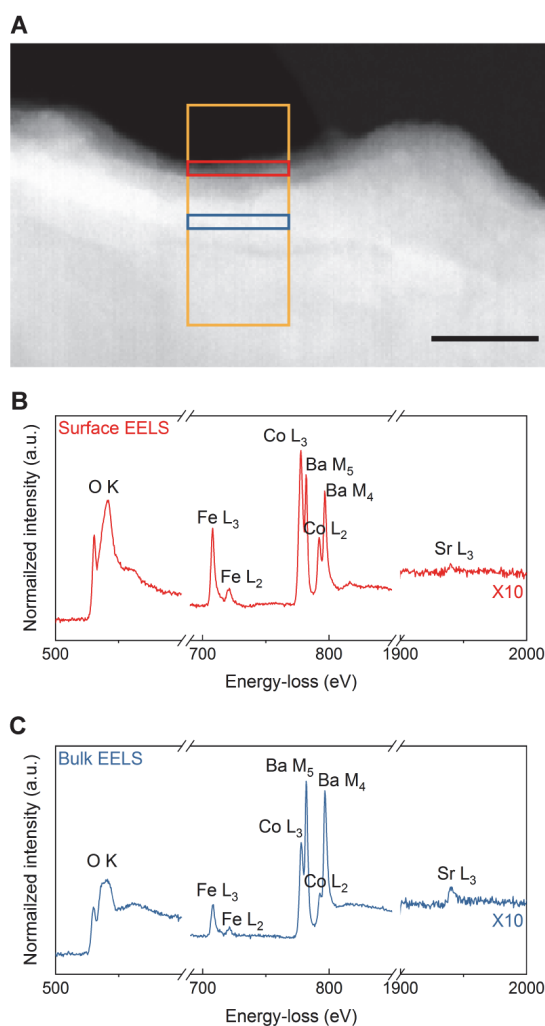


Figure D13. Full energy-loss range EELS spectra involving Ba, Sr, Co, Fe, and O for EELS elemental quantification. (a) HAADF-STEM image of BSCF surface. The orange rectangle indicates the region in which the 2D array spectrum image was acquired. The scale bar is 100 nm. (b) EELS from the surface of BSCF (red rectangular region in a). (c) EELS from the bulk of BSCF (blue rectangle in c). Background is removed and plural scattering is deconvolved in both EEL spectra. The normalized intensity in spectrum region range from 1900-2000 eV was increased by an order of magnitude.

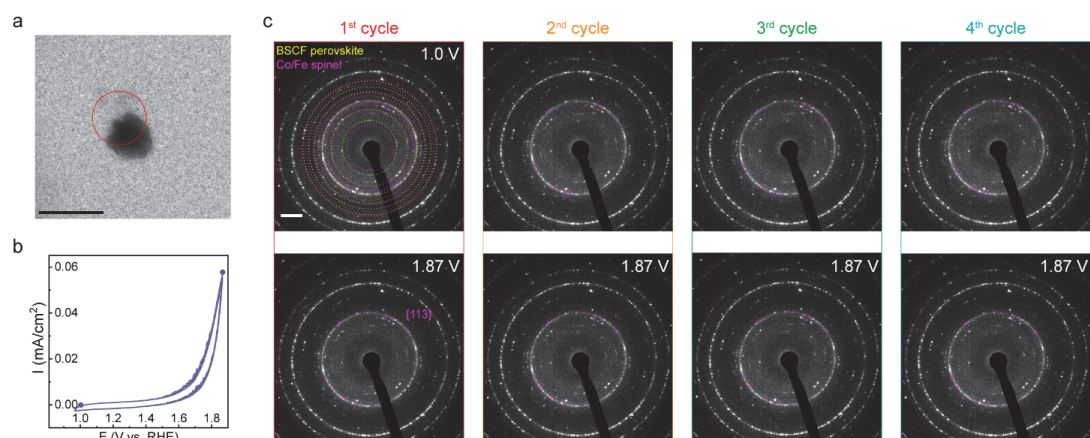


Figure D14. Operando selected area diffraction analysis of BSCF under potential cycling. (a) BF-TEM image of BSCF particle on Pt electrode. The red ring indicates the position and size of the selected area aperture. The scale bar is 1 μm . (b) Polarization curves of the 4 cycles of the experiment. The two purple points indicate the potentials at which SAED patterns in c are extracted for (c). The scan rate is 20 mV/s. (c) Frames of SAED patterns at specific potentials. Yellow and magenta rings indicate BSCF perovskite and Co/Fe spinel reflections, respectively. The magenta arrows indicate the $\{113\}$ spinel reflections. The bright rings, which do not belong to perovskite or spinel, are associated with the underlying Pt polycrystalline thin film electrode. The scale bar is 2 nm^{-1} .

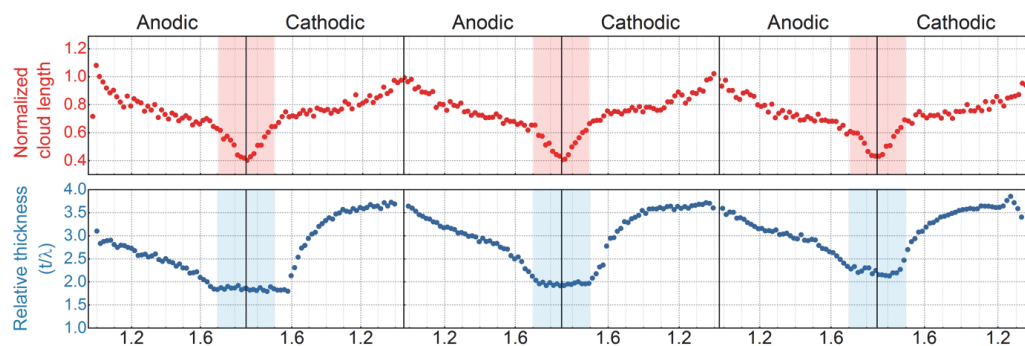


Figure D15. Comparison of normalized cloud length and relative thickness under potential cycling. The shaded regions indicate oxygen evolving conditions.

Bibliography

- (1) Sapountzi, F. M.; Gracia, J. M.; Weststrate, C. J. (Kees J.; Fredriksson, H. O. A.; Niemantsverdriet, J. W. (Hans). Electrocatalysts for the Generation of Hydrogen, Oxygen and Synthesis Gas. *Progress in Energy and Combustion Science* **2017**, 58, 1–35. <https://doi.org/10.1016/j.pecs.2016.09.001>.
- (2) Zeng, K.; Zhang, D. Recent Progress in Alkaline Water Electrolysis for Hydrogen Production and Applications. *Progress in Energy and Combustion Science* **2010**, 36 (3), 307–326. <https://doi.org/10.1016/J.PECS.2009.11.002>.
- (3) Carmo, M.; Fritz, D. L.; Mergel, J.; Stolten, D. A Comprehensive Review on PEM Water Electrolysis. *International Journal of Hydrogen Energy* **2013**, 38 (12), 4901–4934. <https://doi.org/10.1016/J.IJHYDENE.2013.01.151>.
- (4) Suen, N.-T.; Hung, S.-F.; Quan, Q.; Zhang, N.; Xu, Y.-J.; Chen, H. M. Electrocatalysis for the Oxygen Evolution Reaction: Recent Development and Future Perspectives. *Chem. Soc. Rev.* **2017**, 46 (2), 337–365. <https://doi.org/10.1039/C6CS00328A>.
- (5) McCrory, C. C. L.; Jung, S.; Peters, J. C.; Jaramillo, T. F. Benchmarking Heterogeneous Electrocatalysts for the Oxygen Evolution Reaction. *Journal of the American Chemical Society* **2013**, 135 (45), 16977–16987. <https://doi.org/10.1021/ja407115p>.
- (6) Park, S.; Shao, Y.; Liu, J.; Wang, Y. Oxygen Electrocatalysts for Water Electrolyzers and Reversible Fuel Cells: Status and Perspective. *Energy & Environmental Science* **2012**, 5 (11), 9331. <https://doi.org/10.1039/c2ee22554a>.
- (7) Rossmeisl, J.; Qu, Z. W.; Zhu, H.; Kroes, G. J.; Nørskov, J. K. Electrolysis of Water on Oxide Surfaces. *Journal of Electroanalytical Chemistry* **2007**, 607 (1–2), 83–89. <https://doi.org/10.1016/J.JELECHEM.2006.11.008>.
- (8) Lee, Y.; Suntivich, J.; May, K. J.; Perry, E. E.; Shao-Horn, Y. Synthesis and Activities of Rutile IrO₂ and RuO₂ Nanoparticles for Oxygen Evolution in Acid and Alkaline Solutions. *Journal of Physical Chemistry Letters* **2012**, 3 (3), 399–404. <https://doi.org/10.1021/JZ2016507>.
- (9) Song, F.; Bai, L.; Moysiadou, A.; Lee, S.; Hu, C.; Liardet, L.; Hu, X. Transition Metal Oxides as Electrocatalysts for the Oxygen Evolution Reaction in Alkaline Solutions: An Application-Inspired Renaissance. *Journal of the American Chemical Society* **2018**, 140, 7748–7759. <https://doi.org/10.1021/jacs.8b04546>.

-
- (10) Tahir, M.; Pan, L.; Idrees, F.; Zhang, X.; Wang, L.; Zou, J. J.; Wang, Z. L. Electrocatalytic Oxygen Evolution Reaction for Energy Conversion and Storage: A Comprehensive Review. *Nano Energy* **2017**, *37* (May), 136–157. <https://doi.org/10.1016/j.nanoen.2017.05.022>.
- (11) Hong, W. T.; Risch, M.; Stoerzinger, K. A.; Grimaud, A.; Suntivich, J.; Shao-Horn, Y. Toward the Rational Design of Non-Precious Transition Metal Oxides for Oxygen Electrocatalysis. *Energy Environ. Sci.* **2015**, *8* (5), 1404–1427. <https://doi.org/10.1039/C4EE03869J>.
- (12) Suntivich, J.; May, K. J.; Gasteiger, H. a; Goodenough, J. B.; Shao-horn, Y. A Perovskite Oxide Optimized for Molecular Orbital Principles. *Science* **2011**, *334* (6061), 1383–1385. <https://doi.org/10.1126/science.1212858>.
- (13) Song, J.; Wei, C.; Huang, Z.-F.; Liu, C.; Zeng, L.; Wang, X.; Xu, Z. J. A Review on Fundamentals for Designing Oxygen Evolution Electrocatalysts. *Chemical Society Reviews* **2020**, *49* (7), 2196–2214. <https://doi.org/10.1039/C9CS00607A>.
- (14) Man, I. C.; Su, H. Y.; Calle-Vallejo, F.; Hansen, H. A.; Martínez, J. I.; Inoglu, N. G.; Kitchin, J.; Jaramillo, T. F.; Nørskov, J. K.; Rossmeisl, J. Universality in Oxygen Evolution Electrocatalysis on Oxide Surfaces. *ChemCatChem* **2011**, *3* (7), 1159–1165. <https://doi.org/10.1002/cctc.201000397>.
- (15) Grimaud, A.; Diaz-Morales, O.; Han, B.; Hong, W. T.; Lee, Y. L.; Giordano, L.; Stoerzinger, K. A.; Koper, M. T. M.; Shao-Horn, Y. Activating Lattice Oxygen Redox Reactions in Metal Oxides to Catalyse Oxygen Evolution. *Nature Chemistry* **2017**, *9* (5), 457–465. <https://doi.org/10.1038/nchem.2695>.
- (16) Vojvodic, A.; Nørskov, J. K. Optimizing Perovskites for the Water-Splitting Reaction. *Science* **2011**, *334* (6061), 1355–1356. <https://doi.org/10.1126/SCIENCE.1215081>.
- (17) Wei, C.; Feng, Z.; Scherer, G. G.; Barber, J.; Shao-Horn, Y.; Xu, Z. J. Cations in Octahedral Sites: A Descriptor for Oxygen Electrocatalysis on Transition-Metal Spinels. *Advanced Materials* **2017**, *29* (23), 1606800. <https://doi.org/10.1002/ADMA.201606800>.
- (18) Li, H.; Sun, S.; Xi, S.; Chen, Y.; Wang, T.; Du, Y.; Sherburne, M.; Ager, J. W.; Fisher, A. C.; Xu, Z. J. Metal–Oxygen Hybridization Determined Activity in Spinel-Based Oxygen Evolution Catalysts: A Case Study of $\text{ZnFe}_{2-x}\text{Cr}_x\text{O}_4$. *Chemistry of Materials* **2018**, *30* (19), 6839–6848. <https://doi.org/10.1021/acs.chemmater.8b02871>.

- (19) Grimaud, A.; May, K. J.; Carlton, C. E.; Lee, Y.-L.; Risch, M.; Hong, W. T.; Zhou, J.; Shao-Horn, Y. Double Perovskites as a Family of Highly Active Catalysts for Oxygen Evolution in Alkaline Solution. *Nature Communications* **2013**, *4*, 2439. <https://doi.org/10.1038/ncomms3439>.
- (20) Jacobs, R.; Hwang, J.; Shao-Horn, Y.; Morgan, D. Assessing Correlations of Perovskite Catalytic Performance with Electronic Structure Descriptors. *Chemistry of Materials* **2019**, *31* (3), 785–797. <https://doi.org/10.1021/acs.chemmater.8b03840>.
- (21) Hong, W.; Stoerzinger, K. A.; Lee, Y.-L.; Giordano, L.; Grimaud, A. J. L.; Johnson, A. M.; Hwang, J.; Crumlin, E.; Yang, W.; Shao-Horn, Y. Charge-Transfer-Energy-Dependent Oxygen Evolution Reaction Mechanisms for Perovskite Oxides. *Energy Environ. Sci.* **2017**, 2190–2200. <https://doi.org/10.1039/C7EE02052J>.
- (22) Grimaud, A.; Hong, W. T.; Shao-Horn, Y.; Tarascon, J.-M. Anionic Redox Processes for Electrochemical Devices. *Nature Materials* **2016**, *15* (2), 121–126. <https://doi.org/10.1038/nmat4551>.
- (23) Hwang, J.; Rao, R. R.; Giordano, L.; Katayama, Y.; Yu, Y.; Shao-Horn, Y. Perovskites in Catalysis and Electrocatalysis. *Science (New York, N.Y.)* **2017**, *358* (6364), 751–756. <https://doi.org/10.1126/science.aam7092>.
- (24) Cohen, R. E. Origin of Ferroelectricity in Perovskite Oxides. *Nature* **1992**, *358* (6382), 136–138. <https://doi.org/10.1038/358136a0>.
- (25) Acosta, M.; Novak, N.; Rojas, V.; Patel, S.; Vaish, R.; Koruza, J.; Rossetti Jr., G. A.; Rödel, J. BaTiO₃-Based Piezoelectrics: Fundamentals, Current Status, and Perspectives. *Applied Physics Reviews* **2017**, *4* (4), 041305. <https://doi.org/10.1063/1.4990046>.
- (26) Mefford, J. T.; Hardin, W. G.; Dai, S.; Johnston, K. P.; Stevenson, K. J. Anion Charge Storage through Oxygen Intercalation in LaMnO₃ Perovskite Pseudocapacitor Electrodes. *Nature Materials* **2014**, *13*:7 **2014**, *13* (7), 726–732. <https://doi.org/10.1038/nmat4000>.
- (27) Bockris, J. O.; Otagawa, T. The Electrocatalysis of Oxygen Evolution on Perovskites. *Journal of The Electrochemical Society* **1984**, *131* (2), 290–302. <https://doi.org/10.1149/1.2115565>.

- (28) Bockris, J. O.; Otagawa, T. Mechanism of Oxygen Evolution on Perovskites. *The Journal of Physical Chemistry* **2002**, *87* (15), 2960–2971. <https://doi.org/10.1021/J100238A048>.
- (29) Bockris, J. O. M.; Otagawa, T.; Young, V. Solid State Surface Studies of the Electrocatalysis of Oxygen Evolution on Perovskites. *Journal of Electroanalytical Chemistry and Interfacial Electrochemistry* **1983**, *150* (1–2), 633–643. [https://doi.org/10.1016/S0022-0728\(83\)80243-5](https://doi.org/10.1016/S0022-0728(83)80243-5).
- (30) Niedrig, C. *Electrochemical Performance and Stability of Ba_{0.5} Sr_{0.5} Co_{0.8} Fe_{0.2} O_{3-δ} for Oxygen Transport Membranes*; 2015.
- (31) Shao, Z. Investigation of the Permeation Behavior and Stability of a Ba_{0.5}Sr_{0.5}Co_{0.8}Fe_{0.2}O_{3-δ} Oxygen Membrane. *Journal of Membrane Science* **2000**, *172* (1–2), 177–188. [https://doi.org/10.1016/S0376-7388\(00\)00337-9](https://doi.org/10.1016/S0376-7388(00)00337-9).
- (32) Shai, Z.; Hale, S. M. A High-Performance Cathode for the next Generation of Solid-Oxide Fuel Cells. *Nature* **2004**, *431* (1978), 170–174.
- (33) Magnone, E. A Systematic Literature Review on BSCF-Based Cathodes for Solid Oxide Fuel Cell Applications. *Journal of Fuel Cell Science and Technology* **2010**, *7* (6), 064001. <https://doi.org/10.1115/1.4001323>.
- (34) Hong, W. T.; Risch, M.; Stoerzinger, K. A.; Grimaud, A.; Suntivich, J.; Shao-Horn, Y. Toward the Rational Design of Non-Precious Transition Metal Oxides for Oxygen Electrocatalysis. *Energy Environ. Sci.* **2015**, *8* (5), 1404–1427. <https://doi.org/10.1039/C4EE03869J>.
- (35) Fabbri, E.; Nachtegaal, M.; Binninger, T.; Cheng, X.; Kim, B. J.; Durst, J.; Bozza, F.; Graule, T.; Schäublin, R.; Wiles, L.; Pertoso, M.; Danilovic, N.; Ayers, K. E.; Schmidt, T. J. Dynamic Surface Self-Reconstruction Is the Key of Highly Active Perovskite Nano-Electrocatalysts for Water Splitting. *Nature Materials* **2017**, *16* (9), 925–931. <https://doi.org/10.1038/nmat4938>.
- (36) Chen, G.; Zhou, W.; Guan, D.; Sunarso, J.; Zhu, Y.; Hu, X.; Zhang, W.; Shao, Z. Two Orders of Magnitude Enhancement in Oxygen Evolution Reactivity on Amorphous Ba_{0.5} Sr_{0.5} Co_{0.8} Fe_{0.2} O_{3-δ} Nanofilms with Tunable Oxidation State. *Science Advances* **2017**, *3* (6), e1603206. <https://doi.org/10.1126/sciadv.1603206>.
- (37) Risch, M.; Grimaud, A.; May, K. J.; Stoerzinger, K. A.; Chen, T. J.; Mansour, A. N.; Shao-Horn, Y. Structural Changes of Cobalt-Based Perovskites upon Water Oxidation

- Investigated by EXAFS. *Journal of Physical Chemistry C* **2013**, *117* (17), 8628–8635. <https://doi.org/10.1021/jp3126768>.
- (38) May, K. J.; Carlton, C. E.; Stoerzinger, K. A.; Risch, M.; Suntivich, J.; Lee, Y. L.; Grimaud, A.; Shao-Horn, Y. Influence of Oxygen Evolution during Water Oxidation on the Surface of Perovskite Oxide Catalysts. *Journal of Physical Chemistry Letters* **2012**, *3* (22), 3264–3270. <https://doi.org/10.1021/jz301414z>.
- (39) Shen, T.-H.; Spillane, L.; Vavra, J.; Pham, T. H. M.; Peng, J.; Shao-Horn, Y.; Tileli, V. Oxygen Evolution Reaction in $\text{Ba}_{0.5}\text{Sr}_{0.5}\text{Co}_{0.8}\text{Fe}_{0.2}\text{O}_{3-\delta}$ Aided by Intrinsic Co/Fe Spinel-Like Surface. *Journal of the American Chemical Society* **2020**, *142* (37), 15876–15883. <https://doi.org/10.1021/jacs.0c06268>.
- (40) Tong, Y.; Guo, Y.; Chen, P.; Liu, H.; Zhang, M.; Zhang, L.; Yan, W.; Chu, W.; Wu, C.; Xie, Y. Spin-State Regulation of Perovskite Cobaltite to Realize Enhanced Oxygen Evolution Activity. *Chem* **2017**, *3* (5), 812–821. <https://doi.org/10.1016/J.CHEMPR.2017.09.003>.
- (41) Huang, J.; Chen, J.; Yao, T.; He, J.; Jiang, S.; Sun, Z.; Liu, Q.; Cheng, W.; Hu, F.; Jiang, Y.; Pan, Z.; Wei, S. CoOOH Nanosheets with High Mass Activity for Water Oxidation. *Angewandte Chemie International Edition* **2015**, *54* (30), 8722–8727. <https://doi.org/10.1002/ANIE.201502836>.
- (42) Guo, Y.; Tong, Y.; Chen, P.; Xu, K.; Zhao, J.; Lin, Y.; Chu, W.; Peng, Z.; Wu, C.; Xie, Y. Engineering the Electronic State of a Perovskite Electrocatalyst for Synergistically Enhanced Oxygen Evolution Reaction. *Advanced Materials* **2015**, *27* (39), 5989–5994. <https://doi.org/10.1002/ADMA.201502024>.
- (43) Suntivich, J.; Hong, W. T.; Lee, Y. L.; Rondinelli, J. M.; Yang, W.; Goodenough, J. B.; Dabrowski, B.; Freeland, J. W.; Shao-Horn, Y. Estimating Hybridization of Transition Metal and Oxygen States in Perovskites from o k -Edge X-Ray Absorption Spectroscopy. *Journal of Physical Chemistry C* **2014**, *118* (4), 1856–1863. <https://doi.org/10.1021/jp410644j>.
- (44) Lee, Y.-L. L.; Kleis, J.; Rossmeisl, J.; Yang, S. H.; Morgan, D.; Environ, E.; Lee, Y.-L. L.; Kleis, J.; Rossmeisl, J.; Shao-Horn, Y.; Morgan, D. Prediction of Solid Oxide Fuel Cell Cathode Activity with First-Principles Descriptors. *Energy and Environmental Science* **2011**, *4* (10), 3966–3970. <https://doi.org/10.1039/c1ee02032c>.

- (45) Han, B.; Stoerzinger, K. A.; Tileli, V.; Gamalski, A. D.; Stach, E. A.; Shao-Horn, Y. Nanoscale Structural Oscillations in Perovskite Oxides Induced by Oxygen Evolution. *Nature Materials* **2017**, *16* (1), 121–126. <https://doi.org/10.1038/nmat4764>.
- (46) McIntosh, S.; Vente, J. F.; Haije, W. G.; Blank, D. H. A.; Bouwmeester, H. J. M. Oxygen Stoichiometry and Chemical Expansion of Ba_{0.5}Sr_{0.5}Co_{0.8}Fe_{0.2}O_{3-δ} Measured by in Situ Neutron Diffraction. *Chemistry of Materials* **2006**, *18* (8), 2187–2193. <https://doi.org/10.1021/cm052763x>.
- (47) Binniger, T.; Mohamed, R.; Waltar, K.; Fabbri, E.; Levecque, P.; Kötz, R.; Schmidt, T. J. Thermodynamic Explanation of the Universal Correlation between Oxygen Evolution Activity and Corrosion of Oxide Catalysts. *Scientific Reports* **2015**, *5* (1), 12167. <https://doi.org/10.1038/srep12167>.
- (48) Wang, M.; Feng, Z. Interfacial Processes in Electrochemical Energy Systems. *Chemical Communications* **2021**, *57* (81), 10453–10468. <https://doi.org/10.1039/D1CC01703A>.
- (49) Rao, R. R.; Kolb, M. J.; Halck, N. B.; Pedersen, A. F.; Mehta, A.; You, H.; Stoerzinger, K. A.; Feng, Z.; Hansen, H. A.; Zhou, H.; Giordano, L.; Rossmeisl, J.; Vegge, T.; Chorkendorff, I.; Stephens, I. E. L.; Shao-Horn, Y. Towards Identifying the Active Sites on RuO₂ (110) in Catalyzing Oxygen Evolution. *Energy & Environmental Science* **2017**, *10* (12), 2626–2637. <https://doi.org/10.1039/C7EE02307C>.
- (50) Bergmann, A.; Martinez-Moreno, E.; Teschner, D.; Chernev, P.; Gliech, M.; de Araújo, J. F.; Reier, T.; Dau, H.; Strasser, P. Reversible Amorphization and the Catalytically Active State of Crystalline Co₃O₄ during Oxygen Evolution. *Nature Communications* **2015**, *6* (1), 8625. <https://doi.org/10.1038/ncomms9625>.
- (51) Wang, H. Y.; Hung, S. F.; Chen, H. Y.; Chan, T. S.; Chen, H. M.; Liu, B. In Operando Identification of Geometrical-Site-Dependent Water Oxidation Activity of Spinel Co₃O₄. *Journal of the American Chemical Society* **2016**, *138* (1), 36–39. <https://doi.org/10.1021/jacs.5b10525>.
- (52) Louie, M. W.; Bell, A. T. An Investigation of Thin-Film Ni-Fe Oxide Catalysts for the Electrochemical Evolution of Oxygen. *Journal of the American Chemical Society* **2013**, *135* (33), 12329–12337. <https://doi.org/10.1021/ja405351s>.
- (53) Bonn, D.; Eggers, J.; Indekeu, J.; Meunier, J. Wetting and Spreading. *Reviews of Modern Physics* **2009**, *81* (2), 739–805. <https://doi.org/10.1103/RevModPhys.81.739>.

- (54) Xin, B.; Hao, J. Reversibly Switchable Wettability. *Chemical Society Reviews* **2010**, 39 (2), 769–782. <https://doi.org/10.1039/b913622c>.
- (55) Wakerley, D.; Lamaison, S.; Ozanam, F.; Menguy, N.; Mercier, D.; Marcus, P.; Fontecave, M.; Mougél, V. Bio-Inspired Hydrophobicity Promotes CO₂ Reduction on a Cu Surface. *Nature Materials* **2019**, 18 (11), 1222–1227. <https://doi.org/10.1038/s41563-019-0445-x>.
- (56) Rong, W.; Kazuhito, H.; Akira, F.; Makoto, C.; Eiichi, K.; Astushi, K.; Mitsuhide, S.; Toshiya, W. Light-Induced Amphiphilic Surfaces. *Nature* **1997**, 338, 431–432.
- (57) Zhang, L.; Dillert, R.; Bahnemann, D.; Vormoor, M. Photo-Induced Hydrophilicity and Self-Cleaning: Models and Reality. *Energy and Environmental Science* **2012**, 5 (6), 7491–7507. <https://doi.org/10.1039/c2ee03390a>.
- (58) Lahann, J.; Mitragotri, S.; Tran, T. N.; Kaido, H.; Sundaram, J.; Choi, I. S.; Hoffer, S.; Somorjai, G. A.; Langer, R. A Reversibly Switching Surface. *Science* **2003**, 299 (5605), 371–374. <https://doi.org/10.1126/science.1078933>.
- (59) Sun, T.; Wang, G.; Feng, L.; Liu, B.; Ma, Y.; Jiang, L.; Zhu, D. Reversible Switching between Superhydrophilicity and Superhydrophobicity. *Angewandte Chemie International Edition* **2004**, 43 (3), 357–360. <https://doi.org/10.1002/ANIE.200352565>.
- (60) Moon, H.; Cho, S. K.; Garrell, R. L.; Kim, C. J. Low Voltage Electrowetting-on-Dielectric. *Journal of Applied Physics* **2002**, 92 (7), 4080–4087. <https://doi.org/10.1063/1.1504171>.
- (61) Chen, L.; Bonaccorso, E. Electrowetting - From Statics to Dynamics. *Advances in Colloid and Interface Science* **2014**, 210, 2–12. <https://doi.org/10.1016/j.cis.2013.09.007>.
- (62) Lomax, D. J.; Kant, P.; Williams, A. T.; Patten, H. v.; Zou, Y.; Juel, A.; Dryfe, R. A. W. Ultra-Low Voltage Electrowetting Using Graphite Surfaces. *Soft Matter* **2016**, 12 (42), 8798–8804. <https://doi.org/10.1039/c6sm01565d>.
- (63) Zhang, G.; Walker, M.; Unwin, P. R. Low-Voltage Voltammetric Electrowetting of Graphite Surfaces by Ion Intercalation/Deintercalation. *Langmuir* **2016**, 32 (30), 7476–7484. <https://doi.org/10.1021/acs.langmuir.6b01506>.

- (64) Ounnunkad, K.; Patten, H. v.; Velický, M.; Farquhar, A. K.; Brooksby, P. A.; Downard, A. J.; Dryfe, R. A. W. Electrowetting on Conductors: Anatomy of the Phenomenon. *Faraday Discussions* **2017**, *199*, 49–61. <https://doi.org/10.1039/c6fd00252h>.
- (65) Tang, B.; Shao, W.; Groenewold, J.; Li, H.; Feng, Y.; Xu, X.; Shui, L.; Barman, J.; Zhou, G. Transition of Interfacial Capacitors in Electrowetting on a Graphite Surface by Ion Intercalation. *Physical Chemistry Chemical Physics* **2019**, *21* (48), 26284–26291. <https://doi.org/10.1039/c9cp04436a>.
- (66) Zahiri, B.; Sow, P. K.; Kung, C. H.; Mérida, W. Active Control over the Wettability from Superhydrophobic to Superhydrophilic by Electrochemically Altering the Oxidation State in a Low Voltage Range. *Advanced Materials Interfaces* **2017**, *4* (12), 1–12. <https://doi.org/10.1002/admi.201700121>.
- (67) Khan, M. R.; Eaker, C. B.; Bowden, E. F.; Dickey, M. D. Giant and Switchable Surface Activity of Liquid Metal via Surface Oxidation. *Proceedings of the National Academy of Sciences of the United States of America* **2014**, *111* (39), 14047–14051. <https://doi.org/10.1073/pnas.1412227111>.
- (68) Li, T.; Wang, J.; Wang, F.; Zhang, L.; Jiang, Y.; Arandiyan, H.; Li, H. The Effect of Surface Wettability and Coalescence Dynamics in Catalytic Performance and Catalyst Preparation: A Review. *ChemCatChem* **2019**, *11* (6), 1576–1586. <https://doi.org/10.1002/cctc.201801925>.
- (69) Wang, L.; Xiao, F. S. The Importance of Catalyst Wettability. *ChemCatChem* **2014**, *6* (11), 3048–3052. <https://doi.org/10.1002/cctc.201402437>.
- (70) Li, Y.; Zhao, C. Enhancing Water Oxidation Catalysis on a Synergistic Phosphorylated NiFe Hydroxide by Adjusting Catalyst Wettability. *ACS Catalysis* **2017**, *7* (4), 2535–2541. <https://doi.org/10.1021/acscatal.6b03497>.
- (71) Zhang, Q.; Li, T.; Liang, J.; Wang, N.; Kong, X.; Wang, J.; Qian, H.; Zhou, Y.; Liu, F.; Wei, C.; Zhao, Y.; Zhang, X. Highly Wettable and Metallic NiFe-Phosphate/Phosphide Catalyst Synthesized by Plasma for Highly Efficient Oxygen Evolution Reaction. *Journal of Materials Chemistry A* **2018**, *6* (17), 7509–7516. <https://doi.org/10.1039/c8ta01334a>.
- (72) Yoo, J. M.; Shin, H.; Park, S.; Sung, Y.-E. Recent Progress in in Situ/Operando Analysis Tools for Oxygen Electrocatalysis. *Journal of Physics D: Applied Physics* **2021**, *54* (17), 173001. <https://doi.org/10.1088/1361-6463/abd9a4>.

- (73) Yang, Y.; Xiong, Y.; Zeng, R.; Lu, X.; Krumov, M.; Huang, X.; Xu, W.; Wang, H.; DiSalvo, F. J.; Brock, Joel. D.; Muller, D. A.; Abruña, H. D. Operando Methods in Electrocatalysis. *ACS Catalysis* **2021**, *11* (3), 1136–1178. <https://doi.org/10.1021/acscatal.0c04789>.
- (74) Trotochaud, L.; Head, A. R.; Karshoğlu, O.; Kyhl, L.; Bluhm, H. Ambient Pressure Photoelectron Spectroscopy: Practical Considerations and Experimental Frontiers. *Journal of Physics: Condensed Matter* **2017**, *29* (5), 053002. <https://doi.org/10.1088/1361-648X/29/5/053002>.
- (75) Favaro, M.; Yang, J.; Nappini, S.; Magnano, E.; Toma, F. M.; Crumlin, E. J.; Yano, J.; Sharp, I. D. Understanding the Oxygen Evolution Reaction Mechanism on CoO_x Using Operando Ambient-Pressure X-Ray Photoelectron Spectroscopy. *Journal of the American Chemical Society* **2017**, *139* (26), 8960–8970. <https://doi.org/10.1021/jacs.7b03211>.
- (76) Glatzel, P.; Bergmann, U. High Resolution 1s Core Hole X-Ray Spectroscopy in 3d Transition Metal Complexes—Electronic and Structural Information. *Coordination Chemistry Reviews* **2005**, *249* (1–2), 65–95. <https://doi.org/10.1016/J.CCR.2004.04.011>.
- (77) Fabbri, E.; Abbott, D. F.; Nachtegaal, M.; Schmidt, T. J. Operando X-Ray Absorption Spectroscopy: A Powerful Tool toward Water Splitting Catalyst Development. *Current Opinion in Electrochemistry* **2017**, *5* (1), 20–26. <https://doi.org/10.1016/J.COEELEC.2017.08.009>.
- (78) Gao, J.; Xu, C.-Q.; Hung, S.-F.; Liu, W.; Cai, W.; Zeng, Z.; Jia, C.; Chen, H. M.; Xiao, H.; Li, J.; Huang, Y.; Liu, B. Breaking Long-Range Order in Iridium Oxide by Alkali Ion for Efficient Water Oxidation. *Journal of the American Chemical Society* **2019**, *141* (7), 3014–3023. <https://doi.org/10.1021/jacs.8b11456>.
- (79) Minguzzi, A.; Lugaresi, O.; Achilli, E.; Locatelli, C.; Vertova, A.; Ghigna, P.; Rondinini, S. Observing the Oxidation State Turnover in Heterogeneous Iridium-Based Water Oxidation Catalysts. *Chemical Science* **2014**, *5* (9), 3591. <https://doi.org/10.1039/C4SC00975D>.
- (80) Görlin, M.; Chernev, P.; de Araújo, J. F.; Reier, T.; Dresp, S.; Paul, B.; Krähnert, R.; Dau, H.; Strasser, P. Oxygen Evolution Reaction Dynamics, Faradaic Charge Efficiency, and the Active Metal Redox States of Ni-Fe Oxide Water Splitting

- Electrocatalysts. *Journal of the American Chemical Society* **2016**, *138* (17), 5603–5614. <https://doi.org/10.1021/jacs.6b00332>.
- (81) Friebe, D.; Louie, M. W.; Bajdich, M.; Sanwald, K. E.; Cai, Y.; Wise, A. M.; Cheng, M. J.; Sokaras, D.; Weng, T. C.; Alonso-Mori, R.; Davis, R. C.; Bargar, J. R.; Nørskov, J. K.; Nilsson, A.; Bell, A. T. Identification of Highly Active Fe Sites in (Ni,Fe)OOH for Electrocatalytic Water Splitting. *Journal of the American Chemical Society* **2015**, *137* (3), 1305–1313. <https://doi.org/10.1021/ja511559d>.
- (82) Risch, M.; Ringleb, F.; Kohlhoff, M.; Bogdanoff, P.; Chernev, P.; Zaharieva, I.; Dau, H. Water Oxidation by Amorphous Cobalt-Based Oxides: In Situ Tracking of Redox Transitions and Mode of Catalysis. *Energy & Environmental Science* **2015**, *8* (2), 661–674. <https://doi.org/10.1039/C4EE03004D>.
- (83) Daniel Friebe; Michal Bajdich; Siang Yeo, B.; W. Louie, M.; J. Miller, D.; Casalongue, H. S.; Felix Mbuga; Tsu-Chien Weng; Dennis Nordlund; Dimosthenis Sokaras; Roberto Alonso-Mori; T. Bell, A.; Anders Nilsson. On the Chemical State of Co Oxide Electrocatalysts during Alkaline Water Splitting. *Physical Chemistry Chemical Physics* **2013**, *15* (40), 17460–17467. <https://doi.org/10.1039/C3CP52981A>.
- (84) Xiao, Z.; Huang, Y. C.; Dong, C. L.; Xie, C.; Liu, Z.; Du, S.; Chen, W.; Yan, D.; Tao, L.; Shu, Z.; Zhang, G.; Duan, H.; Wang, Y.; Zou, Y.; Chen, R.; Wang, S. Operando Identification of the Dynamic Behavior of Oxygen Vacancy-Rich Co₃O₄ for Oxygen Evolution Reaction. *Journal of the American Chemical Society* **2020**, *142* (28), 12087–12095. <https://doi.org/10.1021/jacs.0c00257>.
- (85) Mefford, J. T.; Akbashev, A. R.; Kang, M.; Bentley, C. L.; Gent, W. E.; Deng, H. D.; Alsem, D. H.; Yu, Y. S.; Salmon, N. J.; Shapiro, D. A.; Unwin, P. R.; Chueh, W. C. Correlative Operando Microscopy of Oxygen Evolution Electrocatalysts. *Nature* **2021**, *593* (7857), 67–73. <https://doi.org/10.1038/s41586-021-03454-x>.
- (86) Bommarito, G. M.; Acevedo, D.; Abruña, H. D. In Situ Monitoring of Electrochemically Induced Roughening with the Crystal Truncation Rod Technique. *Journal of Physical Chemistry* **2002**, *96* (8), 3416–3419. <https://doi.org/10.1021/J100187A044>.
- (87) Huang, X.; Plaza, M.; Ko, J. Y. P.; Abruña, H. D.; Brock, J. D. Relaxation of Asymmetric Crystallographic Tilt: In Situ x-Ray Diffraction Studies of Epitaxial

- Electrodeposition of Bismuth on GaAs (110). *Journal of Applied Physics* **2018**, *124* (3), 035301. <https://doi.org/10.1063/1.5026630>.
- (88) Gründer, Y.; Lucas, C. A. Surface X-Ray Diffraction Studies of Single Crystal Electrocatalysts. *Nano Energy* **2016**, *29*, 378–393. <https://doi.org/10.1016/J.NANOEN.2016.05.043>.
- (89) Reikowski, F.; Maroun, F.; Pacheco, I.; Wiegmann, T.; Allongue, P.; Stettner, J.; Magnussen, O. M. Operando Surface X-Ray Diffraction Studies of Structurally Defined Co₃O₄ and CoOOH Thin Films during Oxygen Evolution. *ACS Catalysis* **2019**, *9* (5), 3811–3821. <https://doi.org/10.1021/acscatal.8b04823>.
- (90) Ortiz Peña, N.; Ihiawakrim, D.; Han, M.; Lassalle-Kaiser, B.; Carencio, S.; Sanchez, C.; Laberty-Robert, C.; Portehault, D.; Ersen, O. Morphological and Structural Evolution of Co₃O₄ Nanoparticles Revealed by *in Situ* Electrochemical Transmission Electron Microscopy during Electrocatalytic Water Oxidation. *ACS Nano* **2019**, *13* (10), 11372–11381. <https://doi.org/10.1021/acsnano.9b04745>.
- (91) Williams, D. B.; Carter, C. B. *Transmission Electron Microscopy*; Springer US: Boston, MA, 2009. <https://doi.org/10.1007/978-0-387-76501-3>.
- (92) Egerton, R. F. *Electron Energy-Loss Spectroscopy in the Electron Microscope*; Springer US: Boston, MA, 2011. <https://doi.org/10.1007/978-1-4419-9583-4>.
- (93) Erni, R. *Aberration-Corrected Imaging in Transmission Electron Microscopy*; IMPERIAL COLLEGE PRESS, 2015. <https://doi.org/10.1142/p960>.
- (94) Wang, Z. W.; Li, Z. Y.; Park, S. J.; Abdela, A.; Tang, D.; Palmer, R. E. Quantitative Z-Contrast Imaging in the Scanning Transmission Electron Microscope with Size-Selected Clusters. *Physical Review B* **2011**, *84* (7), 073408. <https://doi.org/10.1103/PhysRevB.84.073408>.
- (95) Hartel, P.; Rose, H.; Dinges, C. Conditions and Reasons for Incoherent Imaging in STEM. *Ultramicroscopy* **1996**, *63* (2), 93–114. [https://doi.org/10.1016/0304-3991\(96\)00020-4](https://doi.org/10.1016/0304-3991(96)00020-4).
- (96) Pearson, D. H.; Ahn, C. C.; Fultz, B. White Lines and *d*-Electron Occupancies for the 3 *d* and 4 *d* Transition Metals. *Physical Review B* **1993**, *47* (14), 8471–8478. <https://doi.org/10.1103/PhysRevB.47.8471>.

- (97) Tan, H.; Verbeeck, J.; Abakumov, A.; van Tendeloo, G. Oxidation State and Chemical Shift Investigation in Transition Metal Oxides by EELS. *Ultramicroscopy* **2012**, *116*, 24–33. <https://doi.org/10.1016/j.ultramic.2012.03.002>.
- (98) Hodnik, N.; Dehm, G.; Mayrhofer, K. J. J. Importance and Challenges of Electrochemical in Situ Liquid Cell Electron Microscopy for Energy Conversion Research. *Accounts of Chemical Research* **2016**, *49* (9), 2015–2022. <https://doi.org/10.1021/acs.accounts.6b00330>.
- (99) Ross, F. M. Opportunities and Challenges in Liquid Cell Electron Microscopy. *Science* **2015**, *350* (6267). <https://doi.org/10.1126/science.aaa9886>.
- (100) Ross, F. M. *Liquid Cell Electron Microscopy*; Advances in Microscopy and Microanalysis; Cambridge University Press, 2016. <https://doi.org/10.1017/9781316337455>.
- (101) de Jonge, N.; Ross, F. M. Electron Microscopy of Specimens in Liquid. *Nature Nanotechnology* **2011**, *6* (11), 695–704. <https://doi.org/10.1038/nnano.2011.161>.
- (102) Williamson, M. J.; Tromp, R. M.; Vereecken, P. M.; Hull, R.; Ross, F. M. Dynamic Microscopy of Nanoscale Cluster Growth at the Solid–Liquid Interface. *Nature Materials* **2003**, *2* (8), 532–536. <https://doi.org/10.1038/nmat944>.
- (103) Radisic, A.; Vereecken, P. M.; Searson, P. C.; Ross, F. M. The Morphology and Nucleation Kinetics of Copper Islands during Electrodeposition. *Surface Science* **2006**, *600* (9), 1817–1826. <https://doi.org/10.1016/J.SUSC.2006.02.025>.
- (104) Radisic, A.; Vereecken, P. M.; Hannon, J. B.; Searson, P. C.; Ross, F. M. Quantifying Electrochemical Nucleation and Growth of Nanoscale Clusters Using Real-Time Kinetic Data. *Nano Letters* **2006**, *6* (2), 238–242. https://doi.org/10.1021/NL052175I/SUPPL_FILE/NL052175SI20051103_054834.QT.
- (105) Schneider, N. M.; Park, J. H.; Grogan, J. M.; Steingart, D. A.; Bau, H. H.; Ross, F. M. Nanoscale Evolution of Interface Morphology during Electrodeposition. *Nature Communications* **2017**, *8*:1 **2017**, *8* (1), 1–10. <https://doi.org/10.1038/s41467-017-02364-9>.
- (106) Tan, S. F.; Reidy, K.; Klein, J.; Pinkowitz, A.; Wang, B.; Ross, F. M. Real-Time Imaging of Nanoscale Electrochemical Ni Etching under Thermal Conditions. *Chemical Science* **2021**, *12* (14), 5259–5268. <https://doi.org/10.1039/d0sc06057g>.

- (107) Impagnatiello, A.; Cerqueira, C. F.; Coulon, P. E.; Morin, A.; Escribano, S.; Guetaz, L.; Clochard, M. C.; Rizza, G. Degradation Mechanisms of Supported Pt Nanocatalysts in Proton Exchange Membrane Fuel Cells: An Operando Study through Liquid Cell Transmission Electron Microscopy. *ACS Applied Energy Materials* **2020**, *3* (3), 2360–2371. https://doi.org/10.1021/ACSAEM.9B02000/SUPPL_FILE/AE9B02000_SI_001.PDF.
- (108) Beermann, V.; Holtz, M. E.; Padgett, E.; de Araujo, J. F.; Muller, D. A.; Strasser, P. Real-Time Imaging of Activation and Degradation of Carbon Supported Octahedral Pt-Ni Alloy Fuel Cell Catalysts at the Nanoscale Using: In Situ Electrochemical Liquid Cell STEM. *Energy and Environmental Science* **2019**, *12* (8), 2476–2485. <https://doi.org/10.1039/c9ee01185d>.
- (109) Vavra, J.; Shen, T.-H.; Stoian, D.; Tileli, V.; Buonsanti, R. Real-time Monitoring Reveals Dissolution/Redeposition Mechanism in Copper Nanocatalysts during the Initial Stages of the CO₂ Reduction Reaction. *Angewandte Chemie* **2021**, *133* (3), 1367–1374. <https://doi.org/10.1002/ange.202011137>.
- (110) Nagashima, S.; Ikai, T.; Sasaki, Y.; Kawasaki, T.; Hatanaka, T.; Kato, H.; Kishita, K. Atomic-Level Observation of Electrochemical Platinum Dissolution and Redeposition. *Nano Letters* **2019**, *19* (10), 7000–7005. <https://doi.org/10.1021/acs.nanolett.9b02382>.
- (111) Soleymani, A. P.; Parent, L. R.; Jankovic, J. Challenges and Opportunities in Understanding Proton Exchange Membrane Fuel Cell Materials Degradation Using In-Situ Electrochemical Liquid Cell Transmission Electron Microscopy. *Advanced Functional Materials* **2021**, 2105188. <https://doi.org/10.1002/adfm.202105188>.
- (112) Zhu, G. Z.; Prabhudev, S.; Yang, J.; Gabardo, C. M.; Botton, G. A.; Soleymani, L. In Situ Liquid Cell TEM Study of Morphological Evolution and Degradation of Pt-Fe Nanocatalysts during Potential Cycling. *Journal of Physical Chemistry C* **2014**, *118* (38), 22111–22119. <https://doi.org/10.1021/jp506857b>.
- (113) Holtz, M. E.; Yu, Y.; Gunceler, D.; Gao, J.; Sundararaman, R.; Schwarz, K. A.; Arias, T. A.; Abruña, H. D.; Muller, D. A. Nanoscale Imaging of Lithium Ion Distribution during in Situ Operation of Battery Electrode and Electrolyte. *Nano Letters* **2014**, *14* (3), 1453–1459. <https://doi.org/10.1021/nl404577c>.

-
- (114) Wu, F.; Yao, N. Advances in Sealed Liquid Cells for In-Situ TEM Electrochemical Investigation of Lithium-Ion Battery. *Nano Energy*. 2015, pp 196–210. <https://doi.org/10.1016/j.nanoen.2014.11.004>.
- (115) Zeng, Z.; Liang, W. I.; Liao, H. G.; Xin, H. L.; Chu, Y. H.; Zheng, H. Visualization of Electrode-Electrolyte Interfaces in LiPF₆/EC/DEC Electrolyte for Lithium Ion Batteries via in Situ TEM. *Nano Letters* **2014**, *14* (4), 1745–1750. https://doi.org/10.1021/NL403922U/SUPPL_FILE/NL403922U_SI_003.AVI.
- (116) de Jonge, N.; Houben, L.; Dunin-Borkowski, R. E.; Ross, F. M. Resolution and Aberration Correction in Liquid Cell Transmission Electron Microscopy. *Nature Reviews Materials* **2019**, *4* (1), 61–78. <https://doi.org/10.1038/s41578-018-0071-2>.
- (117) de Jonge, N. Theory of the Spatial Resolution of (Scanning) Transmission Electron Microscopy in Liquid Water or Ice Layers. *Ultramicroscopy* **2018**, *187*, 113–125. <https://doi.org/10.1016/j.ultramic.2018.01.007>.
- (118) de Jonge, N.; Verch, A.; Demers, H. The Influence of Beam Broadening on the Spatial Resolution of Annular Dark Field Scanning Transmission Electron Microscopy. *Microscopy and Microanalysis* **2018**, *24* (1), 8–16. <https://doi.org/10.1017/S1431927618000077>.
- (119) de Jonge, N.; Poirier-Demers, N.; Demers, H.; Peckys, D. B.; Drouin, D. Nanometer-Resolution Electron Microscopy through Micrometers-Thick Water Layers. *Ultramicroscopy* **2010**, *110* (9), 1114–1119. <https://doi.org/10.1016/J.ULTRAMIC.2010.04.001>.
- (120) Vlassak, J. J.; Nix, W. D. A New Bulge Test Technique for the Determination of Young's Modulus and Poisson's Ratio of Thin Films. *Journal of Materials Research* **1992**, *7* (12), 3242–3249. <https://doi.org/10.1557/JMR.1992.3242>.
- (121) Peckys, D. B.; Veith, G. M.; Joy, D. C.; de Jonge, N. Nanoscale Imaging of Whole Cells Using a Liquid Enclosure and a Scanning Transmission Electron Microscope. *PLoS ONE* **2009**, *4* (12), 8214. <https://doi.org/10.1371/journal.pone.0008214>.
- (122) Zhu, G.; Jiang, Y.; Huang, W.; Zhang, H.; Zhang, H.; Jin, C. Atomic Resolution Liquid-Cell Transmission Electron Microscopy Investigations of the Dynamics of Nanoparticles in Ultrathin Liquids. *Chemical Communications* **2013**, *49* (93), 10944–10946. <https://doi.org/10.1039/C3CC46667A>.

- (123) Serra-Maia, R.; Kumar, P.; Meng, A. C.; Foucher, A. C.; Kang, Y.; Karki, K.; Jariwala, D.; Stach, E. A. Nanoscale Chemical and Structural Analysis during In Situ Scanning/Transmission Electron Microscopy in Liquids. *ACS Nano* **2021**, *15* (6), 10228–10240. <https://doi.org/10.1021/acsnano.1c02340>.
- (124) Yuk, J. M.; Park, J.; Ercius, P.; Kim, K.; Hellebusch, D. J.; Crommie, M. F.; Lee, J. Y.; Zettl, A.; Alivisatos, A. P. High-Resolution EM of Colloidal Nanocrystal Growth Using Graphene Liquid Cells. *Science* **2012**, *335* (6077), 61–64. https://doi.org/10.1126/SCIENCE.1217654/SUPPL_FILE/1217654S2.MOV.
- (125) Kelly, D. J.; Clark, N.; Zhou, M.; Gebauer, D.; Gorbachev, R. v.; Haigh, S. J. In Situ TEM Imaging of Solution-Phase Chemical Reactions Using 2D-Heterostructure Mixing Cells. *Advanced Materials* **2021**, *33* (29), 2100668. <https://doi.org/10.1002/adma.202100668>.
- (126) Williams, D. B.; Carter, C. B. Electron Energy-Loss Spectrometers and Filters. In *Transmission Electron Microscopy*; Springer US: Boston, MA, 2009; pp 679–698. https://doi.org/10.1007/978-0-387-76501-3_37.
- (127) Woehl, T. J.; Moser, T.; Evans, J. E.; Ross, F. M. Electron-Beam-Driven Chemical Processes during Liquid Phase Transmission Electron Microscopy. *MRS Bulletin* **2020**, *45* (9), 746–753. <https://doi.org/10.1557/mrs.2020.227>.
- (128) Schneider, N. M.; Norton, M. M.; Mendel, B. J.; Grogan, J. M.; Ross, F. M.; Bau, H. H. Electron-Water Interactions and Implications for Liquid Cell Electron Microscopy. *Journal of Physical Chemistry C* **2014**, *118* (38), 22373–22382. <https://doi.org/10.1021/jp507400n>.
- (129) Sutter, E.; Jungjohann, K.; Bliznakov, S.; Courty, A.; Maisonhaute, E.; Tenney, S.; Sutter, P. In Situ Liquid-Cell Electron Microscopy of Silver–Palladium Galvanic Replacement Reactions on Silver Nanoparticles. *Nature Communications* **2014**, *5* (1), 4946. <https://doi.org/10.1038/ncomms5946>.
- (130) Birss, V. I.; Damjanovic, A. Oxygen Evolution at Platinum Electrodes in Alkaline Solutions: I. Dependence on Solution PH and Oxide Film Thickness. *Journal of The Electrochemical Society* **1987**, *134* (1), 113–117. <https://doi.org/10.1149/1.2100385>.
- (131) Damjanovic, A. Electron Transfer through Thin Anodic Films in Oxygen Evolution at Pt Electrodes in Alkaline Solutions. *Electrochimica Acta* **1992**, *37* (13), 2533–2539. [https://doi.org/10.1016/0013-4686\(92\)87095-H](https://doi.org/10.1016/0013-4686(92)87095-H).

- (132) Reier, T.; Oezaslan, M.; Strasser, P. Electrocatalytic Oxygen Evolution Reaction (OER) on Ru, Ir, and Pt Catalysts: A Comparative Study of Nanoparticles and Bulk Materials. *ACS Catalysis* **2012**, 2 (8), 1765–1772. <https://doi.org/10.1021/cs3003098>.
- (133) Bergmann, A.; Jones, T. E.; Martinez Moreno, E.; Teschner, D.; Chernev, P.; Gliech, M.; Reier, T.; Dau, H.; Strasser, P. Unified Structural Motifs of the Catalytically Active State of Co(Oxyhydr)Oxides during the Electrochemical Oxygen Evolution Reaction. *Nature Catalysis* **2018**, 1 (9), 711–719. <https://doi.org/10.1038/s41929-018-0141-2>.
- (134) O'Reilly, J. E. Oxidation-Reduction Potential of the Ferro-Ferricyanide System in Buffer Solutions. *Biochimica et Biophysica Acta (BBA) - Bioenergetics* **1973**, 292 (3), 509–515. [https://doi.org/10.1016/0005-2728\(73\)90001-7](https://doi.org/10.1016/0005-2728(73)90001-7).
- (135) Binggeli, M.; Shen, T.-H.; Tileli, V. Simulating Current Distribution of Oxygen Evolution Reaction in Microcells Using Finite Element Method. *Journal of The Electrochemical Society* **2021**, 168 (10), 106508. <https://doi.org/10.1149/1945-7111/ac2ebf>.
- (136) Alnoush, W.; Black, R.; Higgins, D. Judicious Selection, Validation, and Use of Reference Electrodes for in Situ and Operando Electrocatalysis Studies. *Chem Catalysis* **2021**. <https://doi.org/10.1016/j.checat.2021.07.001>.
- (137) Fabbri, E.; Schmidt, T. J. Oxygen Evolution Reaction—The Enigma in Water Electrolysis. *ACS Catalysis* **2018**, 8 (10), 9765–9774. <https://doi.org/10.1021/acscatal.8b02712>.
- (138) Song, F.; Bai, L.; Moysiadou, A.; Lee, S.; Hu, C.; Liardet, L.; Hu, X. Transition Metal Oxides as Electrocatalysts for the Oxygen Evolution Reaction in Alkaline Solutions: An Application-Inspired Renaissance. *Journal of the American Chemical Society* **2018**, 140, 7748–7759. <https://doi.org/10.1021/jacs.8b04546>.
- (139) Suen, N. T.; Hung, S. F.; Quan, Q.; Zhang, N.; Xu, Y. J.; Chen, H. M. Electrocatalysis for the Oxygen Evolution Reaction: Recent Development and Future Perspectives. *Chemical Society Reviews* **2017**, 46 (2), 337–365. <https://doi.org/10.1039/c6cs00328a>.
- (140) Mefford, J. T.; Rong, X.; Abakumov, A. M.; Hardin, W. G.; Dai, S.; Kolpak, A. M.; Johnston, K. P.; Stevenson, K. J. Water Electrolysis on La_{1-x}Sr_xCoO_{3-δ} Perovskite Electrocatalysts. *Nature Communications* **2016**, 7, 11053. <https://doi.org/10.1038/ncomms11053>.

- (141) Li, M.; Xiong, Y.; Liu, X.; Bo, X.; Zhang, Y.; Han, C.; Guo, L. Facile Synthesis of Electrospun MFe_2O_4 ($\text{M} = \text{Co}, \text{Ni}, \text{Cu}, \text{Mn}$) Spinel Nanofibers with Excellent Electrocatalytic Properties for Oxygen Evolution and Hydrogen Peroxide Reduction. *Nanoscale* **2015**, 7 (19), 8920–8930. <https://doi.org/10.1039/c4nr07243j>.
- (142) Chakrapani, K.; Bendt, G.; Hajiyani, H.; Schwarzrock, I.; Lunkenbein, T.; Salamon, S.; Landers, J.; Wende, H.; Schlögl, R.; Pentcheva, R.; Behrens, M.; Schulz, S. Role of Composition and Size of Cobalt Ferrite Nanocrystals in the Oxygen Evolution Reaction. *ChemCatChem* **2017**, 9 (15), 2988–2995. <https://doi.org/10.1002/cctc.201700376>.
- (143) Fabbri, E.; Nachtegaal, M.; Cheng, X.; Schmidt, T. J. Superior Bifunctional Electrocatalytic Activity of $\text{Ba}_{0.5}\text{Sr}_{0.5}\text{Co}_{0.8}\text{Fe}_{0.2}\text{O}_{3-\delta}$ /Carbon Composite Electrodes: Insight into the Local Electronic Structure. *Advanced Energy Materials* **2015**, 5 (17), 1402033. <https://doi.org/10.1002/aenm.201402033>.
- (144) Hsu, C. S.; Suen, N. T.; Hsu, Y. Y.; Lin, H. Y.; Tung, C. W.; Liao, Y. F.; Chan, T. S.; Sheu, H. S.; Chen, S. Y.; Chen, H. M. Valence- and Element-Dependent Water Oxidation Behaviors: In Situ X-Ray Diffraction, Absorption and Electrochemical Impedance Spectroscopies. *Physical Chemistry Chemical Physics* **2017**, 19 (13), 8681–8693. <https://doi.org/10.1039/c6cp07630k>.
- (145) Burke, M. S.; Kast, M. G.; Trotochaud, L.; Smith, A. M.; Boettcher, S. W. Cobalt-Iron (Oxy)Hydroxide Oxygen Evolution Electrocatalysts: The Role of Structure and Composition on Activity, Stability, and Mechanism. *Journal of the American Chemical Society* **2015**, 137 (10), 3638–3648. <https://doi.org/10.1021/jacs.5b00281>.
- (146) Tung, C. W.; Hsu, Y. Y.; Shen, Y. P.; Zheng, Y.; Chan, T. S.; Sheu, H. S.; Cheng, Y. C.; Chen, H. M. Reversible Adapting Layer Produces Robust Single-Crystal Electrocatalyst for Oxygen Evolution. *Nature Communications* **2015**, 6, 1–9. <https://doi.org/10.1038/ncomms9106>.
- (147) Hung, S.-F.; Hsu, Y.-Y.; Chang, C.-J.; Hsu, C.-S.; Suen, N.-T.; Chan, T.-S.; Chen, H. M. Unraveling Geometrical Site Confinement in Highly Efficient Iron-Doped Electrocatalysts toward Oxygen Evolution Reaction. *Advanced Energy Materials* **2018**, 8 (7), 1701686. <https://doi.org/10.1002/aenm.201701686>.
- (148) Calvillo, L.; Carraro, F.; Vozniuk, O.; Celorrio, V.; Nodari, L.; Russell, A. E.; Debellis, D.; Fermin, D.; Cavani, F.; Agnoli, S.; Granozzi, G. Insights into the Durability of Co-

- Fe Spinel Oxygen Evolution Electrocatalysts: Via Operando Studies of the Catalyst Structure. *Journal of Materials Chemistry A* **2018**, *6* (16), 7034–7041. <https://doi.org/10.1039/c7ta10892c>.
- (149) Tan, H.; Verbeeck, J.; Abakumov, A.; Van Tendeloo, G. Oxidation State and Chemical Shift Investigation in Transition Metal Oxides by EELS. *Ultramicroscopy* **2012**, *116* (2012), 24–33. <https://doi.org/10.1016/j.ultramic.2012.03.002>.
- (150) Müller, P.; Meffert, M.; Störmer, H.; Gerthsen, D. Fast Mapping of the Cobalt-Valence State Energy Loss Spectroscopy. *Microscopy and Microanalysis* **2013**, *19*, 1595–1605.
- (151) de Groot, F. M. F.; Grioni, M.; Fuggle, J. C.; Ghijsen, J.; Sawatzky, G. A.; Petersen, H. Oxygen 1s X-Ray-Absorption Edges of Transition-Metal Oxides. *Physical Review B* **1989**, *40* (8), 5715–5723. <https://doi.org/10.1103/PhysRevB.40.5715>.
- (152) Ignatans, R.; Mallia, G.; Ahmad, E. A.; Spillane, L.; Stoerzinger, K. A.; Shao-Horn, Y.; Harrison, N. M.; Tileli, V. The Effect of Surface Reconstruction on the Oxygen Reduction Reaction Properties of LaMnO₃. *Journal of Physical Chemistry C* **2019**, *123* (18), 11621–11627. <https://doi.org/10.1021/acs.jpcc.9b00458>.
- (153) Sun, S.; Cheng, Z. Effects of H₂O and CO₂ on Electrochemical Behaviors of BSCF Cathode for Proton Conducting IT-SOFC. *Journal of The Electrochemical Society* **2017**, *164* (2), F81–F88. <https://doi.org/10.1149/2.0611702jes>.
- (154) Tileli, V.; Duchamp, M.; Axelsson, A.-K.; Valant, M.; Dunin-Borkowski, R. E.; Alford, N. M. On Stoichiometry and Intermixing at the Spinel/Perovskite Interface in CoFe₂O₄/BaTiO₃ Thin Films. *Nanoscale* **2014**, *7* (1), 218–224. <https://doi.org/10.1039/C4NR04339A>.
- (155) Qian, D.; Xu, B.; Chi, M.; Meng, Y. S. Uncovering the Roles of Oxygen Vacancies in Cation Migration in Lithium Excess Layered Oxides. *Physical Chemistry Chemical Physics* **2014**, *16* (28), 14665–14668. <https://doi.org/10.1039/c4cp01799d>.
- (156) Wang, C.; Baer, D. R.; Amonette, J. E.; Engelhard, M. H.; Antony, J.; Qiang, Y. Morphology and Electronic Structure of the Oxide Shell on the Surface of Iron Nanoparticles. *Journal of the American Chemical Society* **2009**, *131* (25), 8824–8832. <https://doi.org/10.1021/ja900353f>.
- (157) Gao, X.; Liu, J.; Sun, Y.; Wang, X.; Geng, Z.; Shi, F.; Wang, X.; Zhang, W.; Feng, S.; Wang, Y.; Huang, K. Optimized Co²⁺(Td)-O-Fe³⁺(Oh) Electronic State in a Spinel

- Electrocatalyst for Highly Efficient Oxygen Evolution Reaction. *Inorganic Chemistry Frontiers* **2019**, *1*, 3295–3301. <https://doi.org/10.1039/c9qi00852g>.
- (158) Arnold, M.; Gesing, T. M.; Martynczuk, J.; Feldhoff, A. Correlation of the Formation and the Decomposition Process of the BSCF Perovskite at Intermediate Temperatures. *Chemistry of Materials* **2008**, *20* (18), 5851–5858. <https://doi.org/10.1021/cm801463h>.
- (159) Zeljkovi, S.; Miyawaki, J.; Vrankovi, D.; Tervoort, E.; Hauert, R.; Kotegawa, T.; Ivas, T. Solvent-Deficient Synthesis of Nanocrystalline $\text{Ba}_{0.5}\text{Sr}_{0.5}\text{Co}_{0.8}\text{Fe}_{0.2}\text{O}_{3-\delta}$ Powder. *Processing and Application of Ceramics* **2018**, *12* (4), 342–349.
- (160) Behl, W. K.; Toni, J. E. Anodic Oxidation of Cobalt in Potassium Hydroxide Electrolytes. *Journal of Electroanalytical Chemistry* **1971**, *31* (1), 63–75. [https://doi.org/10.1016/S0022-0728\(71\)80043-8](https://doi.org/10.1016/S0022-0728(71)80043-8).
- (161) Kuznetsov, D. A.; Han, B.; Yu, Y.; Rao, R. R.; Hwang, J.; Román-Leshkov, Y.; Shao-Horn, Y. Tuning Redox Transitions via Inductive Effect in Metal Oxides and Complexes, and Implications in Oxygen Electrocatalysis. *Joule* **2018**, *2* (2), 225–244. <https://doi.org/10.1016/j.joule.2017.11.014>.
- (162) Kuznetsov, D. A.; Peng, J.; Giordano, L.; Román-Leshkov, Y.; Shao-Horn, Y. Bismuth Substituted Strontium Cobalt Perovskites for Catalyzing Oxygen Evolution. *Journal of Physical Chemistry C* **2020**, *124* (12), 6562–6570. <https://doi.org/10.1021/acs.jpcc.0c01401>.
- (163) Merkle, R.; Mastrikov, Y. A.; Kotomin, E. A.; Kuklja, M. M.; Maier, J. First Principles Calculations of Oxygen Vacancy Formation and Migration in $\text{Ba}_{1-x}\text{Sr}_x\text{Co}_{1-y}\text{Fe}_y\text{O}_{3-\delta}$ Perovskites. *Journal of The Electrochemical Society* **2011**, *159* (2), B219–B226. <https://doi.org/10.1149/2.077202jes>.
- (164) Shen, T.-H.; Spillane, L.; Peng, J.; Shao-Horn, Y.; Tileli, V. Switchable Wetting of Oxygen-Evolving Oxide Catalysts. *Nature Catalysis* **2022**, *5* (1), 30–36. <https://doi.org/10.1038/s41929-021-00723-w>.
- (165) Volp, G.; Grassian, V. H. Role(s) of Adsorbed Water in the Surface Chemistry of Environmental Interfaces. *Chemical Communications* **2013**, *49* (30), 3071–3094. <https://doi.org/10.1039/c3cc38872g>.
- (166) Song, X.; Zhang, H.; Li, D.; Jia, D.; Liu, T. Electrowetting Lens with Large Aperture and Focal Length Tunability. *Scientific Reports* **2020**, *10* (1), 1–12. <https://doi.org/10.1038/s41598-020-73260-4>.

- (167) Tadanaga, K.; Katata, N.; Minami, T. Super-Water-Repellent Al₂O₃ Coating Films with High Transparency. *Journal of the American Ceramic Society* **1997**, *80* (4), 1040–1042. <https://doi.org/10.1111/j.1151-2916.1997.tb02943.x>.
- (168) Nakajima, A.; Koizumi, S. I.; Watanabe, T.; Hashimoto, K. Effect of Repeated Photo-Illumination on the Wettability Conversion of Titanium Dioxide. *Journal of Photochemistry and Photobiology A: Chemistry* **2001**, *146* (1–2), 129–132. [https://doi.org/10.1016/S1010-6030\(01\)00544-5](https://doi.org/10.1016/S1010-6030(01)00544-5).
- (169) Kornyshev, A. A.; Kucernak, A. R.; Marinescu, M.; Monroe, C. W.; Sleightholme, A. E. S.; Urbakh, M. Ultra-Low-Voltage Electrowetting. *The Journal of Physical Chemistry C* **2010**, *114* (35), 14885–14890. <https://doi.org/10.1021/jp101051e>.
- (170) Chang, F. M.; Cheng, S. L.; Hong, S. J.; Sheng, Y. J.; Tsao, H. K. Superhydrophilicity to Superhydrophobicity Transition of CuO Nanowire Films. *Applied Physics Letters* **2010**, *96* (11). <https://doi.org/10.1063/1.3360847>.
- (171) Chang, J. H.; Choi, D. Y.; Han, S.; Pak, J. J. Driving Characteristics of the Electrowetting-on-Dielectric Device Using Atomic-Layer-Deposited Aluminum Oxide as the Dielectric. *Microfluidics and Nanofluidics* **2010**, *8* (2), 269–273. <https://doi.org/10.1007/s10404-009-0511-9>.
- (172) Mibus, M.; Zangari, G. Performance and Reliability of Electrowetting-on-Dielectric (EWOD) Systems Based on Tantalum Oxide. *ACS Applied Materials and Interfaces* **2017**, *9* (48), 42278–42286. <https://doi.org/10.1021/acsami.7b07366>.
- (173) Stoerzinger, K. A.; Hong, W. T.; Azimi, G.; Giordano, L.; Lee, Y. L.; Crumlin, E. J.; Biegalski, M. D.; Bluhm, H.; Varanasi, K. K.; Shao-Horn, Y. Reactivity of Perovskites with Water: Role of Hydroxylation in Wetting and Implications for Oxygen Electrocatalysis. *Journal of Physical Chemistry C* **2015**, *119* (32), 18504–18512. <https://doi.org/10.1021/acs.jpcc.5b06621>.
- (174) Drelich, J.; Miller, J. D.; Hupka, J. The Effect of Drop Size on Contact Angle over a Wide Range of Drop Volumes. *Journal of Colloid And Interface Science*. 1993, pp 379–385. <https://doi.org/10.1006/jcis.1993.1050>.
- (175) Koopal, L. K. Wetting of Solid Surfaces: Fundamentals and Charge Effects. *Advances in Colloid and Interface Science* **2012**, *179–182*, 29–42. <https://doi.org/10.1016/j.cis.2012.06.009>.

- (176) Bohinc, K.; Kralj-Iglič, V.; Iglič, A. Thickness of Electrical Double Layer. Effect of Ion Size. *Electrochimica Acta* **2001**, *46* (19), 3033–3040. [https://doi.org/10.1016/S0013-4686\(01\)00525-4](https://doi.org/10.1016/S0013-4686(01)00525-4).
- (177) Frati, F.; Hunault, M. O. J. Y.; de Groot, F. M. F. Oxygen K-Edge X-Ray Absorption Spectra. *Chemical Reviews* **2020**, *120* (9), 4056–4110. <https://doi.org/10.1021/acs.chemrev.9b00439>.
- (178) Dukovic, J.; Tobias, C. W. The Influence of Attached Bubbles on Potential Drop and Current Distribution at Gas-Evolving Electrodes. *Journal of The Electrochemical Society* **1987**, *134* (2), 331–343. <https://doi.org/10.1149/1.2100456>.
- (179) Chang, Y. H.; Hau, N. Y.; Liu, C.; Huang, Y. T.; Li, C. C.; Shih, K.; Feng, S. P. A Short-Range Ordered-Disordered Transition of a NiOOH/Ni(OH)₂ Pair Induces Switchable Wettability. *Nanoscale* **2014**, *6* (24), 15309–15315. <https://doi.org/10.1039/c4nr05261g>.
- (180) Verbeeck, J.; van Aert, S. Model Based Quantification of EELS Spectra. *Ultramicroscopy* **2004**, *101* (2–4), 207–224. <https://doi.org/10.1016/J.ULTRAMIC.2004.06.004>.
- (181) Thomas, P. J.; Midgley, P. A. An Introduction to Energy-Filtered Transmission Electron Microscopy. *Topics in Catalysis* **2002**, *21*:4 (4), 109–138. <https://doi.org/10.1023/A:1021377125838>.
- (182) Mildner, S.; Beleggia, M.; Mierwaldt, D.; Hansen, T. W.; Wagner, J. B.; Yazdi, S.; Kasama, T.; Ciston, J.; Zhu, Y.; Jooss, C. Environmental TEM Study of Electron Beam Induced Electrochemistry of Pr_{0.64}Ca_{0.36}MnO₃ Catalysts for Oxygen Evolution. *The Journal of Physical Chemistry C* **2015**, *119* (10), 5301–5310. <https://doi.org/10.1021/jp511628c>.
- (183) Chenna, S.; Crozier, P. A. Operando Transmission Electron Microscopy: A Technique for Detection of Catalysis Using Electron Energy-Loss Spectroscopy in the Transmission Electron Microscope. *ACS Catalysis* **2012**, *2* (11), 2395–2402. <https://doi.org/10.1021/cs3004853>.
- (184) Crozier, P. A.; Chenna, S. In Situ Analysis of Gas Composition by Electron Energy-Loss Spectroscopy for Environmental Transmission Electron Microscopy. *Ultramicroscopy* **2011**, *111* (3), 177–185. <https://doi.org/10.1016/j.ultramic.2010.11.005>.

-
- (185) Makino, T. Composition and Structure Control by Source Gas Ratio in LPCVD SiN_x. *Journal of The Electrochemical Society* **1983**, *130* (2), 450–455. <https://doi.org/10.1149/1.2119729>.
- (186) Nong, H. N.; Falling, L. J.; Bergmann, A.; Klingenhof, M.; Tran, H. P.; Spöri, C.; Mom, R.; Timoshenko, J.; Zichittella, G.; Knop-Gericke, A.; Piccinin, S.; Pérez-Ramírez, J.; Cuenya, B. R.; Schlögl, R.; Strasser, P.; Teschner, D.; Jones, T. E. Key Role of Chemistry versus Bias in Electrocatalytic Oxygen Evolution. *Nature* **2020**, *587* (7834), 408–413. <https://doi.org/10.1038/s41586-020-2908-2>.
- (187) Giordano, L.; Han, B.; Risch, M.; Hong, W. T.; Rao, R. R.; Stoerzinger, K. A.; Shao-Horn, Y. PH Dependence of OER Activity of Oxides: Current and Future Perspectives. *Catalysis Today* **2016**, *262*, 2–10. <https://doi.org/10.1016/j.cattod.2015.10.006>.

CURRICULUM VITAE

TZU-HSIEN SHEN

Email: tzu-hsien.shen@epfl.ch **Tel:** +41-787332058

Address: Chemin des Triauldes 4 B562, Ecublens VD 1024, Switzerland

EDUCATION

- Ph.D. Materials Science and Engineering** **2017 – 2022**
École Polytechnique Fédérale de Lausanne (EPFL) Lausanne, Switzerland
Thesis title: Electron probing of oxygen-evolving oxide catalysts
Advisor: Prof. Vasiliki Tileli
- M.S. Materials Science and Engineering** **2016**
National Taiwan University Taipei, Taiwan
Thesis title: Growth and analysis of semiconductor heterojunction nanowires
Advisor: Prof. Cheng-Yen Wen
- B.S. Materials Science and Engineering** **2014**
National Taiwan University Taipei, Taiwan
GPA: **4.18 / 4.3** (overall), **4.23 / 4.3** (major); ranked **3rd / 53**

RESEARCH EXPERIENCE

- Doctoral assistant** **2017 - Current**
Institute of Materials, EPFL Lausanne, Switzerland
Understand the correlation between surface and electrocatalytic properties of OERⁱ catalysts:
- Unveil and quantify the intrinsic Co/Fe spinel surface on perovskite BSCFⁱⁱⁱ oxides using STEM-EELSⁱⁱⁱ
 - Optimize and fabricate MEMS^{iv} chips for electrochemical LP-(S)TEM^v applications
 - Perform operando electrochemical LP-TEM imaging to study switchable wettability of Co-based oxide OER catalysts under potential cycling
 - Probe the catalytic O₂ of oxygen evolving oxide catalysts in real-time using O K EEL spectra
- Research student in Nano-material Growth Laboratory** **2014 - 2016**
Dept. Materials Science and Engineering, National Taiwan University Taipei, Taiwan
Growth and analysis of Si/Ge axial heterojunction nanowires:
- Grew Si/Ge heterojunction nanowires with abrupt interface using UHVCVD^{vi}
 - Analyzed strain and sharpness at the Si/Ge interface using (S)TEM

WORK EXPERIENCE

Research assistant in Advanced Materials Laboratory

2016 - 2017

Institute of Atomic and Molecular Sciences, Academia Sinica

Taipei, Taiwan

- Provided (S)TEM characterizations from specimen preparation to operation of energy materials including thermoelectric, batteries, and catalyst applications

Assistant operator of (S)TEM

2015 - 2016

Dept. Materials Science and Engineering, National Taiwan University

Taipei, Taiwan

- Provided technical service and maintained JEOL 2010F (S)TEM

RESEARCH SKILLS

- (S)TEM-based characterization techniques: imaging, diffraction, Ω -filter EFTEM^{vii}, EELS, and EDS^{viii}, and electrochemical LP-(S)TEM
- Electrochemical measurements (potentiostat) for operando (S)TEM: cyclic voltammetry and chronoamperometry
- MEMS chip fabrication in clean-room: photolithography, etching, and e-beam deposition
- Operando (S)TEM and EELS data processing: DigitalMicrograph[®] and *Mathematica*

TEACHING EXPERIENCE

Supervising master student projects

2018 – 2020

Institute of Materials, EPFL

Lausanne, Switzerland

Teaching assistant of Thermodynamics for Materials Science Course

2018 - 2020

Institute of Materials, EPFL

Lausanne, Switzerland

Lecturer: Prof. Vasiliki Tileli

Teaching assistant of Theory of Diffraction Course

2014 - 2015

Dept. Materials Science and Engineering, National Taiwan University

Taipei, Taiwan

Lecturer: Prof. Cheng-Yen Wen

AWARDS

Poster Award Winner

2021

T.-H. Shen, L. Spillane, J. Vavra, and V. Tileli. “Electron Probing of the Oxygen Evolving $\text{Ba}_{0.5}\text{Sr}_{0.5}\text{Co}_{0.8}\text{Fe}_{0.2}\text{O}_{3-\delta}$ ”. *Microscopy & Microanalysis 2021*, virtual meeting.

Excellent Poster Award

2016

T.-H. Shen, C.-H. Yu, and C.-Y. Wen, “Growth and Strain Analysis of Si/Ge Axial Heterojunction Nanowires”. *Symposium on Nano Device Technology, Hsinchu, Taiwan*.

Academic Presidential Award (Top 5% in class), two times

2012 & 2013

Department of Materials Science and Engineering, National Taiwan University, Taipei, Taiwan

PUBLICATIONS

1. T.-H. Shen, L. Spillane, J. Peng, Y. Shao-Horn, and V. Tileli. Switchable Wetting of Oxygen Evolving Catalysts. *Nature Catalysis* **2022**, 5 (1), 30-36.
2. M. Binggeli, T.-H. Shen, and V. Tileli. Simulating Current Distribution of Oxygen Evolution Reaction in Microcells Using Finite Element Method. *Journal of The Electrochemical Society* **2021**, 168, 106508.
3. T.-H. Shen, L. Spillane, J. Vavra, and V. Tileli. Electron Probing of the Oxygen Evolving $\text{Ba}_{0.5}\text{Sr}_{0.5}\text{Co}_{0.8}\text{Fe}_{0.2}\text{O}_{3-\delta}$. *Microscopy and Microanalysis* **2021**, 27 (S1), 2438-2439.
4. L. Nela, J. Ma, C. Erine, P. Xiang, T.-H. Shen, V. Tileli, T. Wang, K. Cheng, and E. Matioli. Multi-channel Nanowire Devices for Efficient Power Conversion. *Nature Electronics* **2021**, 4 (4), 284-290.
5. M. Lihter, M. Graf, D. Iveković, M. Zhang, T.-H. Shen, Y. Zhao, M. Macha, V. Tileli, and A. Radenovic. Electrochemical Functionalization of Selectively Addressed MoS_2 Nanoribbons for Sensor Device Fabrication. *ACS Applied Nano Materials* **2021**, 4 (2), 1076-1084.
6. J. Vavra, T.-H. Shen, D. Stoian, V. Tileli, and R. Buonsanti. Real-time Monitoring Reveals Dissolution/Redeposition Mechanism in Copper Nanocatalysts during the Initial Stages of the CO_2 Reduction Reaction. *Angewandte Chemie* **2021**, 60 (3), 1347-1354.
7. T.-H. Shen, L. Spillane, J. Vavra, T. H. M. Pham, J. Peng, Y. Shao-Horn, and V. Tileli. Oxygen Evolution Reaction in $\text{Ba}_{0.5}\text{Sr}_{0.5}\text{Co}_{0.8}\text{Fe}_{0.2}\text{O}_{3-\delta}$ Aided by Intrinsic Co/Fe Spinel-Like Surface. *Journal of the American Chemical Society* **2020**, 142, 15876–15883.
8. J. Hou, R. Girod, N. Nianias, T.-H. Shen, J. Fan, and V. Tileli. Lithium-Gold Reference Electrode for Potential Stability During In Situ Electron Microscopy Studies of Lithium-Ion Batteries. *Journal of The Electrochemical Society* **2020**, 167, 110515.
9. J. Hou, A. Freiberg, T.-H. Shen, R. Girod, J. Gonthier, S.-J. Kim, F. Maglia, H. A. Gasteiger, and V. Tileli. Charge/discharge Cycling of $\text{Li}_{1+x}(\text{Ni}_{0.6}\text{Co}_{0.2}\text{Mn}_{0.2})_{1-x}\text{O}_2$ Primary Particles Performed in a Liquid Microcell for Transmission Electron Microscopy Studies. *Journal of Physics: Energy* **2020**, 2, 34007.
10. DP Wong, M. Aminzare, T.-L. Chou, C.-S. Pang, Y.-R. Liu, T.-H. Shen, B.-K. Chang, H.-T. Lien, S.-T. Chang, C.-H. Chien, Y.-Y. Chen, M.-W. Chu, Y.-W. Yang, W.-P. Hsieh, G. Rogl, P. Rogl, Y. Kakefuda, T. Mori, M.-Y. Chou, L.-C. Chen, K.-H. Chen. Origin of Band

Modulation in GeTe-Rich Ge–Sb–Te Thin Film. *ACS Applied Electronic Materials* **2019**, 1 (12), 2619-2625.

11. A. Weiß, A. Siebel, M. Bernt, **T.-H. Shen**, V. Tileli, and H. A. Gasteiger. Impact of Intermittent Operation on Lifetime and Performance of a PEM Water Electrolyzer. *Journal of The Electrochemical Society* **2019**, 166, F487–F497.
12. T. Billo, F.-Y. Fu, P. Raghunath, I. Shown, W.-F. Chen, H.-T. Lien, **T.-H. Shen**, J.-F. Lee, T.-S. Chan, K.-Y. Huang, C.-I. Wu, MC Lin, J.-S. Hwang, C.-H. Lee, L.-C. Chen, and K.-H. Chen. Ni-Nanocluster Modified Black TiO₂ with Dual Active Sites for Selective Photocatalytic CO₂ Reduction. *Small* **2018**, 14 (2), 1702928.
13. H.-Y. Lee, **T.-H. Shen**, C.-Y. Hu, Y.-Y. Tsai, and C.-Y. Wen. Producing Atomically Abrupt Axial Heterojunctions in Silicon–Germanium Nanowires by Thermal Oxidation. *Nano letters* **2017**, 17 (12), 7494-7499.
14. S. Samireddi, I. Shown, **T.-H. Shen**, H.-C. Huang, K.-T. Wong, L.-C. Chen, and K.-H. Chen. Hybrid bimetallic-N4 electrocatalyst derived from a pyrolyzed ferrocene–Co-corrole complex for oxygen reduction reaction. *Journal of Materials Chemistry A* **2017**, 5 (19), 9279-9286.
15. Y.-J. Huang, **T.-H. Shen**, L.-H. Lee, C.-Y. Wen, S.-C. Lee. Low-power resistive random access memory by confining the formation of conducting filaments. *AIP Advances* **2016**, 6 (6), 065022.

ⁱ Oxygen evolution reaction

ⁱⁱ Ba_{0.5}Sr_{0.5}Co_{0.8}Fe_{0.2}O_{3-δ}

ⁱⁱⁱ Scanning transmission electron microscopy-electron energy-loss spectroscopy

^{iv} Micro-electromechanical systems

^v Liquid-phase TEM

^{vi} Ultra-high vacuum chemical vapor deposition

^{vii} Energy-filtered TEM

^{viii} Energy dispersive spectroscopy